Dynamic fracture of solar grade single crystalline silicon wafers

Meng Wang

N°d'ordre NNT : 2019LYSEI081

THESE de DOCTORAT DE L'UNIVERSITE DE LYON
opérée au sein de
l'Institut National des Sciences Appliquées de Lyon

Ecole Doctorale N° ED162
MECANIQUE, ENERGETIQUE, GENIE CIVIL, ACOUSTIQUE

Spécialité/ discipline de doctorat :
Mécanique – Génie Mécanique – Génie Civil

Soutenue publiquement le 15/11/2019, par :
Meng WANG

Dynamic Fracture of Solar Grade Single Crystalline Silicon Wafers

---

Devant le jury composé de :

Nom, prénom	grade/qualité	établissement/entreprise	
			Président
CHABLI Amal	Directrice de Recherche	CEA-INES	Rapporteur
BONAMY Daniel	Expert Senior, HDR	CEA-Saclay	Rapporteur
JAY Fineberg	Professeur des Universités	HUJI	Examinateur
ADDA-BEDIA Mokhtar	Directeur de Recherche	ENS Lyon	Examinateur
NELIAS Daniel	Professeur des Universités	INSA Lyon	Directeur de thèse
FOURMEAU Marion	Maître de Conférences	INSA Lyon	Co-directrice
ALBARET Tristan	Maître de Conférences	Université Lyon1	Invité
RIVA Roland	Ingénieur-Chercheur	CEA-INES	Invité

Département FEDORA – INSA Lyon - Ecoles Doctorales – Quinquennal 2016-2020

SIGLE	ECOLE DOCTORALE	NOM ET COORDONNEES DU RESPONSABLE
CHIMIE	**CHIMIE DE LYON** **http://www.edchimie-lyon.fr** Sec. : Renée EL MELHEM Bât. Blaise PASCAL, 3e étage **secretariat@edchimie-lyon.fr** INSA : R. GOURDON	M. Stéphane DANIELE Institut de recherches sur la catalyse et l'environnement de Lyon IRCELYON-UMR 5256 Équipe CDFA 2 Avenue Albert EINSTEIN 69 626 Villeurbanne CEDEX **directeur@edchimie-lyon.fr**
E.E.A.	**ÉLECTRONIQUE, ÉLECTROTECHNIQUE, AUTOMATIQUE** **http://edeea.ec-lyon.fr** Sec. : M.C. HAVGOUDOUKIAN **ecole-doctorale.eea@ec-lyon.fr**	M. Gérard SCORLETTI École Centrale de Lyon 36 Avenue Guy DE COLLONGUE 69 134 Écully Tél : 04.72.18.60.97 Fax 04.78.43.37.17 **gerard.scorletti@ec-lyon.fr**
E2M2	**ÉVOLUTION, ÉCOSYSTÈME, MICROBIOLOGIE, MODÉLISATION** **http://e2m2.universite-lyon.fr** Sec. : Sylvie ROBERJOT Bât. Atrium, UCB Lyon 1 Tél : 04.72.44.83.62 INSA : H. CHARLES **secretariat.e2m2@univ-lyon1.fr**	M. Philippe NORMAND UMR 5557 Lab. d'Ecologie Microbienne Université Claude Bernard Lyon 1 Bâtiment Mendel 43, boulevard du 11 Novembre 1918 69 622 Villeurbanne CEDEX **philippe.normand@univ-lyon1.fr**
EDISS	**INTERDISCIPLINAIRE SCIENCES-SANTÉ** **http://www.ediss-lyon.fr** Sec. : Sylvie ROBERJOT Bât. Atrium, UCB Lyon 1 Tél : 04.72.44.83.62 INSA : M. LAGARDE **secretariat.ediss@univ-lyon1.fr**	Mme Emmanuelle CANET-SOULAS INSERM U1060, CarMeN lab, Univ. Lyon 1 Bâtiment IMBL 11 Avenue Jean CAPELLE INSA de Lyon 69 621 Villeurbanne Tél : 04.72.68.49.09 Fax : 04.72.68.49.16 **emmanuelle.canet@univ-lyon1.fr**
INFOMATHS	**INFORMATIQUE ET MATHÉMATIQUES** **http://edinfomaths.universite-lyon.fr** Sec. : Renée EL MELHEM Bât. Blaise PASCAL, 3e étage Tél : 04.72.43.80.46 **infomaths@univ-lyon1.fr**	M. Luca ZAMBONI Bât. Braconnier 43 Boulevard du 11 novembre 1918 69 622 Villeurbanne CEDEX Tél : 04.26.23.45.52 **zamboni@maths.univ-lyon1.fr**
Matériaux	**MATÉRIAUX DE LYON** **http://ed34.universite-lyon.fr** Sec. : Stéphanie CAUVIN Tél : 04.72.43.71.70 Bât. Direction **ed.materiaux@insa-lyon.fr**	M. Jean-Yves BUFFIÈRE INSA de Lyon MATEIS - Bât. Saint-Exupéry 7 Avenue Jean CAPELLE 69 621 Villeurbanne CEDEX Tél : 04.72.43.71.70 Fax : 04.72.43.85.28 **jean-yves.buffiere@insa-lyon.fr**
MEGA	**MÉCANIQUE, ÉNERGÉTIQUE, GÉNIE CIVIL, ACOUSTIQUE** **http://edmega.universite-lyon.fr** Sec. : Stéphanie CAUVIN Tél : 04.72.43.71.70 Bât. Direction **mega@insa-lyon.fr**	M. Jocelyn BONJOUR INSA de Lyon Laboratoire CETHIL Bâtiment Sadi-Carnot 9, rue de la Physique 69 621 Villeurbanne CEDEX **jocelyn.bonjour@insa-lyon.fr**
ScSo	**ScSo*** **http://ed483.univ-lyon2.fr** Sec. : Véronique GUICHARD INSA : J.Y. TOUSSAINT Tél : 04.78.69.72.76 **veronique.cervantes@univ-lyon2.fr**	M. Christian MONTES Université Lyon 2 86 Rue Pasteur 69 365 Lyon CEDEX 07 **christian.montes@univ-lyon2.fr**

*ScSo : Histoire, Géographie, Aménagement, Urbanisme, Archéologie, Science politique, Sociologie, Anthropologie

Fate can start you at the bottom

Dreams can take you to the top

Acknowledges

My heartfelt thanks to my supervisor, professor Daniel Nélias for his continuous support and constant encouragement, both scientific and otherwise that make me successfully complete this thesis. I am grateful for the freedom he provided me in choosing and pursuing research goals. Then, I want to extend my sincere gratitude to my co-supervisor, Dr. Marion Fourmeau. She has walked me through all the stages of the writing of this thesis. Her conscientious academic spirit and modest, open-minded personality inspire me both in academic study and daily life.

My sincere gratitude to Dr. Lv Zhao for his support and advice. Lv was a source of inspiration for me in his way of doing and communicating research, and Lv has fought hard to get our paper published, and I deeply thank him for it. Many thanks for Franck Legrand for his abundant experience that provided great assistance in breaking those unruly silicon wafers.

Also, I would like to express my heartfelt gratitude to all of my committee members : Dr. Amal Chabli, Dr, Daniel Bonamy, Prof. Jay Fineberg, Dr. Mokhtar Adda-Bedia, Dr. Tristan Albert and Dr. Roland Riva for generously offering their time, support, guidance, and goodwill throughout the review of this document. Thanks for letting my defense be an enjoyable moment, and for their brilliant comments and suggestions. Many thanks to Dr. Mokhtar Adda-Bedia for the useful literature and the valuable discussion on the fracture mechanics.

Many thanks to my fantastic labmates : Alexis BONETTO, Bo CHEN, Chao ZHANG, Deqi LIU, Efoe WALLACE, Haoming LUO, Pierre Panico, Quanshangze DU, Jin Huang, Shuai CHEN, Thomas JAILIN, Tristan DJOURACHKOVITCH, Thibaut Hirschler, Wenjun GAO, WenqiZHU, Ye LU, Zikang LOW. They made the lab a friendly place to work in and taught me much about science and life. Special thanks to all the professors of the MIMESIS and MULTIMAP. Each at some point agreed to hear my questions and suggest helpful advice. My thanks go also to all the people of Lamcos who without exception always responded to my questions and requests with a smile.

And, of course, a big thank you to Wanni for her love, her support and her company. This is also an opportunity to thank my parents and my sister who helped me greatly in this period of my life, each in their own way.

Abstract

Crystalline silicon has attracted substantial attention for decades because of its large applications in solar cells and microelectromechanical systems. The high brittleness of silicon raises wide concerns since the failure of this semiconductor material increases the manufacturing cost and decreases the efficiency of the utilization of Si-based devices. Crack propagation of crystalline silicon is the main cause of catastrophic failure of silicon components. It has been intensively studied but is not fully understood yet due to intricate dynamic fracture behavior linked to small-scale phenomena. Therefore, the development of feasible methods to study the dynamic fracture, as well as the deeper understanding of fracture mechanism of crystalline silicon, are of paramount importance to improve the reliability and durability of Si-based systems for both industrial and scientific practitioners.

In this work, dynamic fracture behavior of solar-grade single crystalline silicon wafers under mechanical loads was studied. We carried out fracture experiments on (001) silicon wafers using three-line or four-line bending apparatus under quasi-static loading. The entire fracture process was captured using a high-speed camera and was analyzed by the high-speed imaging technique. We studied the post-mortem fracture surface using a digital microscope, a laser scanning profilometer, as well as an atomic force microscope. The failure source of the silicon wafer was identified using fractographic analysis. Coupling the crack velocity measurement and fractographic analysis, we determined the crack front during dynamic crack propagation, which exhibits a velocity-dependent shape. We revealed the source of (110)-(111) cleavage plane deflection phenomena during high-speeding crack propagation under line-contact effects. Besides, jointly with the finite element simulations, we demonstrated how dynamics of the crack front is governed by the crystallographic direction-dependent dynamic fracture toughness. Finally, in comparison with the Wallner lines on the fracture surface, generated by linear perturbations of elastic waves on the crack front, we highlight the nucleation and strong nonlinear characteristics of out-of-plane corrugation waves, leaving specific markings that alter the surface roughness of asperity-free material.

KEYWORDS : Brittle fracture, Single crystalline silicon, Dynamic crack propagation, Crack deflection, Shear waves, Corrugation waves.

Résumé

La résistance mécanique du silicium cristallin a fait l'objet de plusieurs études notamment à l'état mono-cristallin c'est-à-dire à l'état quasiment pur et pour une microstructure modèle, et aussi pour ses nombreuses applications dans les systèmes photovoltaïques et les semi-conducteurs. Étant donné que la défaillance de ce matériau semi-conducteur augmente le coût de fabrication et diminue l'efficacité et le rendement des dispositifs en silicium, la durabilité de ce matériau est l'un des éléments clé. La propagation de fissures dans le silicium mono-cristallin est l'un des modes de ruine de ces composants. Ce sujet a été étudié durant de nombreuses années, cependant il n'est pas encore complètement compris en raison de la complexité du comportement de la rupture dynamique liée aux phénomènes à petite échelle. Par conséquent, la compréhension des mécanismes de rupture du silicium cristallin comme matériau modèle reste un sujet d'actualité, avec pour objectif in fine d'améliorer la fiabilité et la durabilité des systèmes à base de silicium.

Dans ce travail, le comportement à la rupture dynamique de plaques minces (ndlr wafers) de silicium monocristallin de qualité solaire soumis à des charges mécaniques a été étudié. Nous avons effectué les essais de rupture sur des tranches minces de silicium (001) en utilisant un appareil de flexion quatre lignes sous chargement quasi-statique. Le processus de rupture de wafers de silicium a été capturé à l'aide d'une caméra rapide puis étudié par analyse d'images. Nous avons étudié la surface de rupture post-mortem via un microscope numérique, un profilomètre à balayage laser ainsi qu'un microscope à force atomique. La source de défaillance de la tranche de silicium a été identifiée par analyse fractographique. En couplant la mesure de vitesse de fissure et l'analyse fractographique, nous déterminons le front de fissure pendant la propagation dynamique de la fissure, ce qui donne une forme qui dépend de la vitesse de propagation de la fissure. Nous révélons ainsi la source des phénomènes de déflexion du plan de clivage (110) - (111) lors de la propagation de fissures à grande vitesse sous l'effet d'un changement multiaxial lors du passage sous les rouleaux. En outre, conjointement avec les simulations par éléments finis, nous avons montré comment la dynamique du front de fissure est contrôlée par la ténacité dynamique qui dépend de l'orientation cristallographique. Enfin, par l'observation des lignes de Wallner sur la surface de fracture - marques qui sont générées par des perturbations linéaires des ondes élastiques au niveau du front de fissure, nous mettons en évidence la nucléation et les caractéristiques non linéaires de ces traces appelées 'front waves' visibles sur les faciès de rupture des matériaux mono-cristallins lorsque la vitesse de propagation de la fissure se rapproche de la vitesse de Rayleigh.

KEYWORDS : Rupture fragile, Silicium monocristallin, Propagation dynamique de fissure, Déflexion de fissure, Ondes de cisaillement, Onde nonlinéaire.

Contents

List of Figures

General introduction

Solar power is one of the key to a clean and sustainable energy future. The conversion from solar energy to electric energy falls into two categories : concentrated solar power (CSP) [ZHA 13] and photovoltaics (PV) [WEN 13]. CSP systems concentrate the sunlight to a small beam through mirrors or lenses, then the thermal energy converted from sunlight powers a heat engine to generate electricity. PV systems directly generate electricity from sunlight based on the photovoltaic effect. Nowadays, with the fast development of PV systems, the cost of solar electricity for PV systems drops and worldwide growth of PV installations has averaged 24% per annum between 2010 to 2017 [FRA 19].

A PV system employs PV modules, connected assembly of PV solar cells to create an additive voltage. The solar cells are classified into three generations. Crystalline silicon (c-Si) solar cell is the conventional, first generation solar cell, based on the monocrystalline or multicrystalline silicon wafer. The thin-film solar cell is a second generation solar cell, which is produced by the deposition of a thin PV film on a substrate. This technology can reduce the PV material in a cell and may enable the solar cell to be flexible. The third generation solar cells are described as emerging technologies, such as multi-junction solar cell. These solar cells may be able to pass through the limitation of power efficiency of single-junction solar cell [GRE 04] and are still under development. By far, the c-Si solar cells are always the most prevalent components of PV systems. According to [FRA 19], production of Si-wafer based solar cells accounted for about 95% of the total PV market in 2017. Their performances are received great attention for the development of PV in both industries and laboratories.

The power efficiency of the solar cell is one of the focus that is relevant to the profitability of solar power. As reported in [FRA 19], the record cell efficiency is 26.7% in 2017 for monocrystalline silicon solar cell in laboratory and is 22.3% for multicrystalline silicon solar cell. For the commercial wafer-based silicon modules with mass production, their efficiency is about 15 - 20% and can reach up to 21% for certain types of wafer-based silicon modules. Besides the power efficiency, low-cost manufacturing process of PV systems is another concern. The manufacture of Si wafer counts for about 40% of the cost of solar cells, while more than 40% of the pure silicon is machined into dust during wafer sawing [ITR]. Improving the sawing technique to produce thinner wafers and increasing recycling rates are subjected to scientific concerns. Moreover, the durability and reliability of solar cells are important issues for PV production and utilization, which may affect the profitability of PV systems. During the manufacturing of Si-wafers, losses of material due to the breakage of silicon crystal may be up to 5% - 10% [RUP 09]. [KÖN 17]

reported that the fracture of Si-wafers of the solar cells in a module could remove more than 10% of cells from the electrical circuit. Fig. 1 shows an electroluminescence image of a PV module under four-line bending loading. Black areas correspond to electrically disconnected zone due to the breakage solar cells.

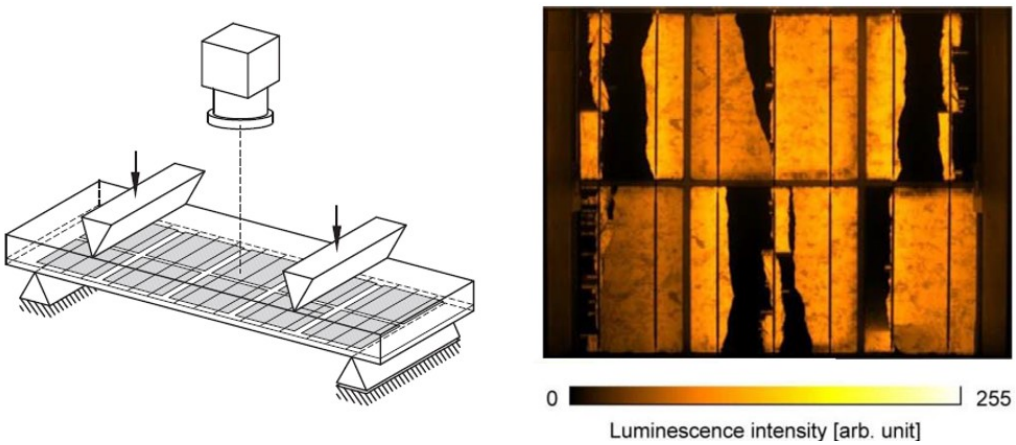

FIGURE 1: Electroluminescence image of a PV module under four-line bending loading adapted from [INF 14].

The Equipex Durasol, supported by the French National Research Agency (ANR), is dedicated to improving the durability of solar materials and systems. This platform gathers indoor and outdoor researches of all scientific fields covering the whole value chain of solar power technology. Among them, the laboratory LaMCoS conducts fundamental studies on the mechanical properties of Si-wafer based PV systems from material level (silicon crystal) to solar cell level. The silicon specimens are provided by our platform partner CEA - INES.

The theoretical stress for breaking the atomic bonds of silicon is in the order of 20,000 MPa, while the practical stress to break a Si solar cell is in the order of 200 MPa. This huge difference commonly occurs in brittle materials, and is due to the presence of the crack. Hence, the study of the formation and subsequent propagation of cracks, which govern the material strength, is necessary for the durability of the solar cell. Once initiating, the crack generally undergoes dynamic process in the silicon wafer, and the dissipation processes occurring near the vicinity of the crack, determine material resistance to dynamic fracture. The crack can propagate at speed close to the wave speed in the crystalline silicon and involves fast dissipation processes. In this thesis, we aim at observing, characterizing the dynamic fracture processes, and deepening the understanding of the high-speed crack propagation in the silicon crystal.

In the first chapter, we present the basic knowledge of the linear elastic fracture mechanics (LEFM), including the equation of motion for a rapidly propagating crack. Then, we briefly review some investigations in the literature of fracture instabilities during the dynamic crack propagation for both isotropic amorphous materials and anisotropic silicon crystal. The discrepancies of the experimental studies and molecular dynamics simula-

tions with theoretical predictions are shown. Some puzzles about the dynamics of cracks in the silicon crystal are put forward.

In the second chapter, the crystalline silicon specimens are presented, including the crystal structure, the cleavage, as well as their fabrications. The fracture experiments using the three-line and four-line bending setup are shown. The crack velocity measurement method based on the high-speed camera is shown, and the feasibility of the high-speed camera in our tests are discussed. The correlation between the fracture stress and the pre-crack length, as well as the crack velocity, are presented. The terminal crack velocity up to about 85% of the sound speed in silicon is obtained.

In the third chapter, we present the fractographic analysis on the fracture surface of silicon specimens. We show the studies on typical fracture surface traces, which allow to determine the crack origin and the crack front shape. Particularly, we highlight how we identify the shear wave perturbations on the crack front. We demonstrate how the shear waves gradually deflect the crack front out of the fracture plane during the dynamic crack propagation, which finally induce the crack path deflection. Besides, we show also the determination of the crack velocity based on the fractography and the crack recovery phenomenon. The outlook in this chapter presents the occurrence of microbranching instabilities that induce special surface markings. This inspires the studies in the next chapter.

In the fourth chapter, based on the finite element simulations and LEFM, the whole crack front dynamics that governed by the ensemble of local energy balances of every point along the front is demonstrated. We show that dynamic fracture toughness of silicon involves a sharp jump depending on the crystallographic direction when the crack velocity increases and induces a local kink of the crack front. At the local crack front kink spot, we identify the emission of out-of-plane corrugation waves localized along the crack front, which can be triggered by the microbranching instabilities as well. We highlight the non-linear attributes of corrugation waves based on the AFM characterizations and compare them with the linear perturbations on the crack front.

Finally, we draw general conclusions and some prospects.

Chapter 1

Introduction to dynamic fracture

The theoretical basis of linear elastic fracture mechanics is presented. State of the art concerning intricate quasi-static and dynamic fracture instabilities in isotropic amorphous materials and silicon single crystal are shown. Some open questions are put forward as well.

1 Fracture mechanics

The history of fracture mechanics begins from the calculation of Inglis [ING 13] in 1913 on the stress concentrations around elliptical holes in a linear elastic material (Fig. 1.1). He found that the stress at the tip of the major axis increase with a factor of $\sqrt{a/\rho}$ where a is the length of the semi-major axis and ρ is the radius of curvature at the tip. The stress amplifies when ρ decreases. For an ideal sharp crack ($\rho \to 0$), the stress becomes singular at the crack tip. However, this is 'unrealistic'.

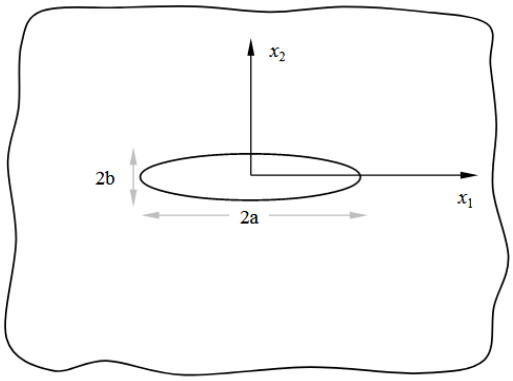

FIGURE 1.1: Two dimensional elliptical notch in an infinite medium

In the 1920s, A. A. Griffith advanced the understanding of the fracture mechanics thanks to the pioneering work on the fracture of glass [GRI 21]. Motivated by the puzzle of why the glass fibers break at strengths that are a few hundred orders of magnitude lower than the theoretical strength of atomic bonds of glass, he found that the fracture strength depends on the size of material flows so Inglis' solution failed to explain this dependence. Griffith realized that the fracture mechanism should be described by an energy-balance approach instead of strength consideration. He suggested that the crack grows when the strain energy released by the growth of crack per unit area G is equal to twice the surface energy 2γ, given by

$$G = 2\gamma \tag{1.1}$$

Griffith assumption applies well to brittle materials for which the energy dissipation solely associates with atomic bond breaking, such as glass. However, it fails to deal with material failures involving nonlinear dissipative processes around the crack tip. For instance, the energy dissipation due to the plastic deformation around the crack tip in steels could be about 1000 times higher than the surface energy [ORO 49].

1.1 Linear elastic fracture mechanics

Until the early 1950s, the theory of fracture mechanics was advanced thanks to the assumption of 'small-scale yielding'. Irwin [IRW 57] first found that if the zone (called process zone) where energy dissipation occurs around the crack is small enough compared

to the crack size, the material outside of the process zone can be assumed to be linear elastic. This assumption circumvents nonlinear processes in the process zone that provides a way to compute the energy available for fracture G using the purely elastic solution. This drives the development of the linear elastic fracture mechanics (LEFM) [LAW 93, FRE 98].

LEFM show that, regardless of the loading and the sample geometry, the asymptotic solution of the stresses in polar coordinates (r, θ) with the origin at the crack tip is :

$$\sigma(r,\theta) \backsimeq \frac{K_\alpha}{\sqrt{2\pi r}} f_\alpha(\theta) \tag{1.2}$$

where $\alpha = I$, II or III. The functions $f_\alpha(\theta)$ are dimensionless quantities of angle. K_α, named the stress intensity factor (SIF), characterize the singular stress field around the crack tip, and they depend on the sample and crack geometry. The α are known as 'cracking modes' to classify the fracture problems according to the loads subjected to the crack. As shown in Fig. 1.2, mode I is an open mode where the crack is subjected to pure tension; mode II is a sliding mode where the crack is subjected to in-plane shear; mode III is a tearing mode where the crack is subjected to out-of-plane shear load. The K_I, K_{II}, K_{III} are the SIF associated with each mode. For instance, for a straight crack of length $2a$ in an infinite plate subjected by a uniform tensile load σ, $K_I = \sigma\sqrt{\pi a}$. In the case of a crack is subjected to complex loads, the stress field can be expressed by the sum of Eq. 1.2 in different modes.

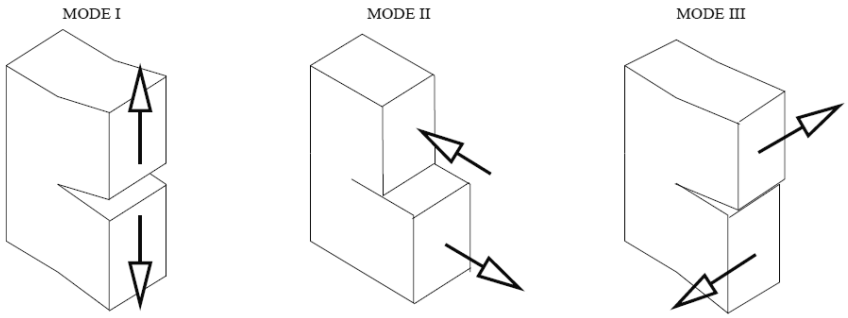

FIGURE 1.2: Three modes of fracture.

To calculate the available energy for fracture, LEFM provide the relationship between the SIF and the potential energy dissipated per unit area of crack growth G as :

$$G \propto K_\alpha^2 \tag{1.3}$$

G is called energy release rate (ERR). For instance, the ERR for mode I crack under plane strain is given by, $G = K_I^2(1-\nu^2)/E$, where ν is the Poisson's ratio and E is the Young's modulus. In the case of multiple modes, G is the sum of ERR of each mode.

Hence, an energy-based fracture criterion can be given by :

$$G \geqslant G_c \tag{1.4}$$

The crack growth is initiated when the ERR reaches a critical value, G_c, called the fracture toughness. The fracture toughness is a material property that reveals the material resistance to failure. G_c can be equal to 2γ for brittle material and becomes larger than 2γ when plastic deformation occurs at the crack tip. Besides, from Eq. 1.3, the critical ERR G_c is related to the critical SIF which can be determined from standard testing methods [BRO 66, ANS 81].

1.2 Crack tip equation of motion

When the crack begins to propagate, LEFM describe that the motion of the crack tip (crack tip speed v) is governed by the dynamic energy balance between the energy flowing into the process zone per unit area of crack growth, $G(v)$, and the fracture energy dissipation rate within the process zone, Γ, given by :

$$G(v) = \Gamma \tag{1.5}$$

$G(v)$ is a load-dependent quantity and Γ is a material-dependent quantity, hence, once $G(v)$ is computed and Γ is calculated or experimentally determined, the crack tip motion can be predicted. In the case that a straight semi-infinite crack propagating at speed v in an unbounded body under given Mode I loading, the dynamic SIF, $K_I(v)$ can be written as :

$$K_I(v) = k(v)K_I(l) \tag{1.6}$$

The dynamic SIF $K_I(v)$ is decomposed by the equilibrium SIF $K_I(l)$ which depends on the applied load and the crack length l, but is independent on the crack tip speed and a universal function of the crack tip speed $k(v)$, given by $(1-v/c_R)/\sqrt{1-v/c_d}$ (c_R and c_d are the Rayleigh wave speed and the dilatation wave speed). This relation can also be applied on other fracture modes with different universal functions [FRE 98].

According to Eq. 1.3, the dynamic ERR $G(v)$ for the crack at speed v, can be written as :

$$G(v) = \frac{1-\nu^2}{E} K_I(l)^2 g(v) = G(l)g(v) \tag{1.7}$$

The equilibrium ERR $G(l)$ presents the strain energy release rate for a crack at rest of length l under a specific loading configuration, and $g(v)$ is a universal function of v that can be approximated by a linear function $g(v) \approx 1 - v/c_R$. Eq. 1.7 is obtained from the analysis of a semi-infinite crack and an unbounded body. Meanwhile, it is valid for the crack propagation in a bounded body before the stress field around the crack tip is affected by the stress waves reflected from the boundaries [FRE 98, BOU 14].

Hence, the energy-balance based equation of motion of the crack tip reads :

$$\Gamma = G(l)(1 - \frac{v}{c_R}) \tag{1.8}$$

where $G(l)$ is the ERR that involves no dynamics but depends on the specific cracked geometry and applied load. As a result, for the quasi-static crack propagation in the brittle material, where $\Gamma = 2\gamma$ and $v \sim 0$, Eq. 1.8 is equivalent to the Griffith criterion (Eq. 1.3). For the high-speed crack propagation, the limit of the crack velocity is bounded by c_R.

1.3 The J-integral

An attractive theoretical concept was developed by J. R. Rice [RIC 68] to calculate the strain energy release rate G, named J-integral. For a linear or nonlinear elastic material subjected to a two-dimensional deformation, Rice showed that a line integral J surrounding a crack tip or a notch, expressed as

$$J = \int_{\Gamma} (W dy - \mathbf{T}\frac{\partial \mathbf{u}}{\partial x} ds) \tag{1.9}$$

is path independent and its value is equal to the ERR G. As shown in Fig 1.3, Γ here is a curve encircling the crack tip. W represents the strain energy density. $\mathbf{T} = [\sigma]n$ is the surface traction vector and $\mathbf{u}$ the displacement vector.

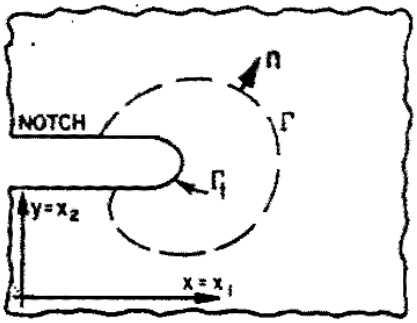

FIGURE 1.3: Two dimensional deformation field with a surfaced notch [RIC 68].

Eq. 1.9 can be directly computed using the finite element method, hence the J-integral provides an appealing way to calculate the equilibrium ERR $G(l)$ in Eq. 1.8 and then study the dynamic fracture behavior.

1.4 Dynamic fracture toughness

LEFM describe the crack tip as the sole energy sink around which all dissipative processes occur during the fracture. Γ includes all the energy dissipation that characterizes the material resistance to crack propagation. In the case of static or quasi-static crack propagation, Γ is equivalent to G_c, while in the case of dynamic crack propagation, Γ can be a rate dependent function $\Gamma(v)$, called dynamic fracture toughness, which varies with the instantaneous crack velocity v. For example, Figs. 1.4 show the dynamic fracture energy, determined with experimental methods, as a function of the crack velocity for four different materials reported in the literature. The $\Gamma(v)$ for soda-lime glass is nearly constant, while an increase of the dynamic fracture toughness occurs for other materials when v increases.

For ductile materials, the increase of $\Gamma(v)$ was found due to the rate-dependent dissipation relative to the plastic deformation within the crack tip plastic zone [FRE 98]. However, for brittle fracture, the source of the sharp increase of $\Gamma(v)$ could not be the

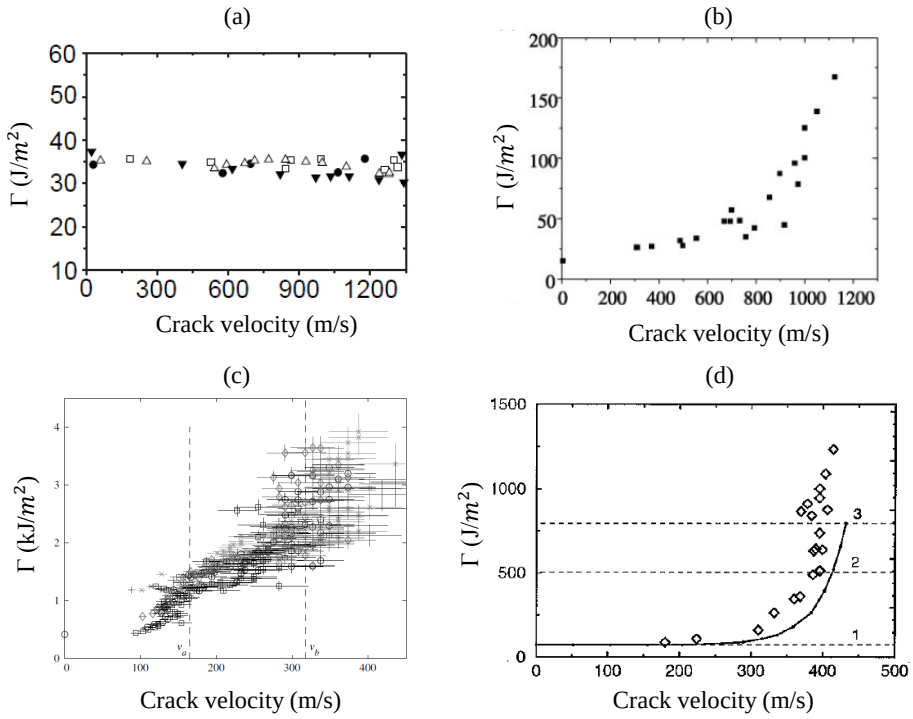

FIGURE 1.4: Dynamic fracture toughness evolution. $\Gamma(v)$ for (a) soda-lime glass from [SHA 99] ($c_R \simeq 3300$ m/s), (b) AISI 4340 steel from [ROS 84] ($c_R \simeq 2950$ m/s), (c) PMMA from [GUE 12] ($c_R \simeq 930$ m/s) and (d) Homalite-100 from [HAU 98] ($c_R \simeq 1010$ m/s).

plastic deformation near the crack tip since dislocations in brittle amorphous material like Homalite are immobile [CHE 17]. Hence, other dissipation mechanisms occurring in a small region around the crack tip should be considered.

2 Intricate fracture surface morphologies

The equation of motion of the crack (Eq. 1.8) predicts that the crack can reach a speed equal to Rayleigh wave speed. However, as shown in Figs. 1.4, the crack speed converges to a lower value than the Rayleigh wave speed when the fracture energy increases. Since the fracture energy is no more used to accelerate the crack, there should exist other phenomena that dissipate the energy during dynamic crack propagation, for example, the increase of fracture surface. These phenomena are expected to alter the crack motion and leave specific morphologies on the fracture surface. Hence, the study of the fracture surface to characterize these specific surface features is a primary step to reveal the dynamic fracture mechanisms. Lets now focus on some typical fracture surface morphologies.

2.1 Mirror, mist and hackle zone

For the fracture of brittle material, the fracture surface usually has three distinct structures, called 'mirror, mist and hackle zones'. These zones have been observed in brittle amorphous materials like glass and PMMA, as well as crystalline materials like silicon. Fig. 1.5 shows the fracture surface of glass rod broken in tension reported in [JOH 66]. Near the fracture origin, the 'mirror' fracture surface is generated by the low-speeding crack propagation under mode I loading. As the crack propagates, the crack surface continues roughening and translates from the mist zone to the hackle zone.

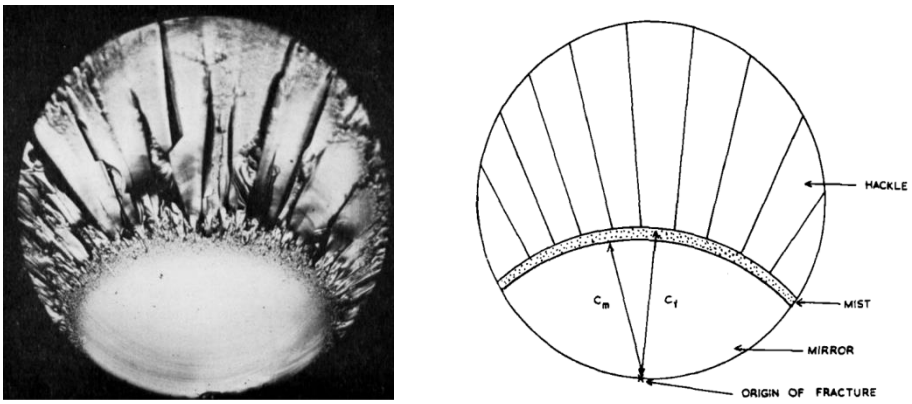

FIGURE 1.5: Fracture surface of glass rod from [JOH 66] presenting mirror, mist and hackle zones.

The transition of the fracture surface from a two-dimensional (2D) mirror surface to a three-dimensional (3D) hackle surface implies that the crack growth cannot be described by a crack-tip propagating in a 2D material but a crack front, i.e. the leading edge of the crack, propagating in a 3D material. The 3D fracture surface morphologies in the mist and hackle zones have been investigated for decades. Several characteristic structures of fracture surface are getting known, such as 'lances' structure, micro-branches, and conic surface markings, etc.

2.2 Helical crack-front instability

Helical crack-front instabilities were first observed on the fracture surface of the glass and referred as 'lance' instabilities because of their specific structures [SOM 69], and then have been observed in the hackle zone in a variety of material, such as plexiglass [CHE 15], hydrogel, [RON 14] and metal [PON 10]. As shown in Fig. 1.6(a) from [RON 14], the 'lance' instabilities are generated at any crack propagation speed when the crack front involves helical deformations (right inset) under the superposition of mode I and mode III loading (left inset). A planar crack front splits into an array of daughter crack fronts forming an angle θ relative to the maximum tensile plane and propagating parallel to each other, which produces stepped fracture surfaces, as presented in Fig. 1.6(b). The angle θ increases when the ratio between the SIF of mode III and SIF of mode I, K_{III}/K_I

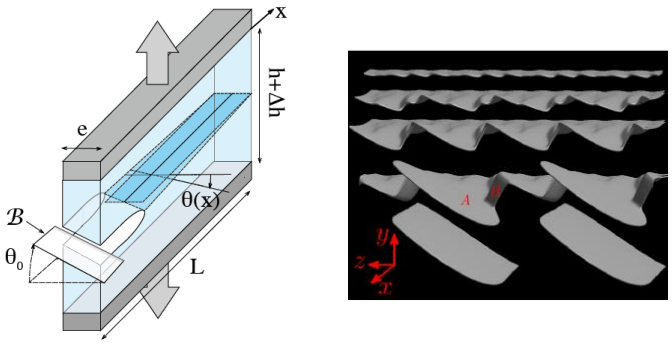

(a)

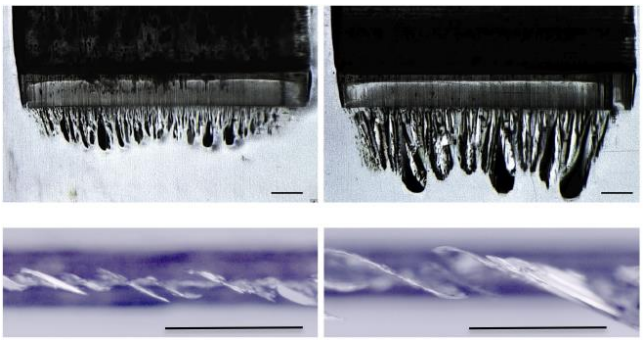

(b)

FIGURE 1.6: Helical crack-front instabilities. (a) Example of loading configuration of lance formation (left inset) from [RON 14] and sequences of helical crack-front during the crack propagation from [CHE 15]. (b) Front view (top insets) and bottom view (bottom inset) of broken sample from [CHE 15].

increases. Besides, the steps are found to be self-similar, where the in-plane array spacing of the steps grows linearly with the crack propagation length and the growth rate increases with K_{III}/K_I [RON 14]. Moreover, in the light of LFEM, the characteristics of the helical crack-front instabilities can be well predicted by phase-filed simulations [CHE 15] or analytic solution [LEB 15, LEB 19].

2.3 Conic surface markings

Conic surface markings are commonly observed on the fracture surface of brittle amorphous materials when the crack velocity reaches a critical value, v_a. The generation of the conic surface markings is due to voids coalescing with the crack front in the presence of material heterogeneities, such as defects or microscopic cavitation. When the crack is driven by a high SIF that propagates at $v > v_a$, the intense stress field ahead of the crack front can cause the nucleation of microcracks from the heterogeneities before the crack front crosses the heterogeneities. Fig. 1.7 presents the fracture surface of PMMA with conic markings from [GUE 12], where $v_a = 0.19c_R$. Bright spots in the microscope

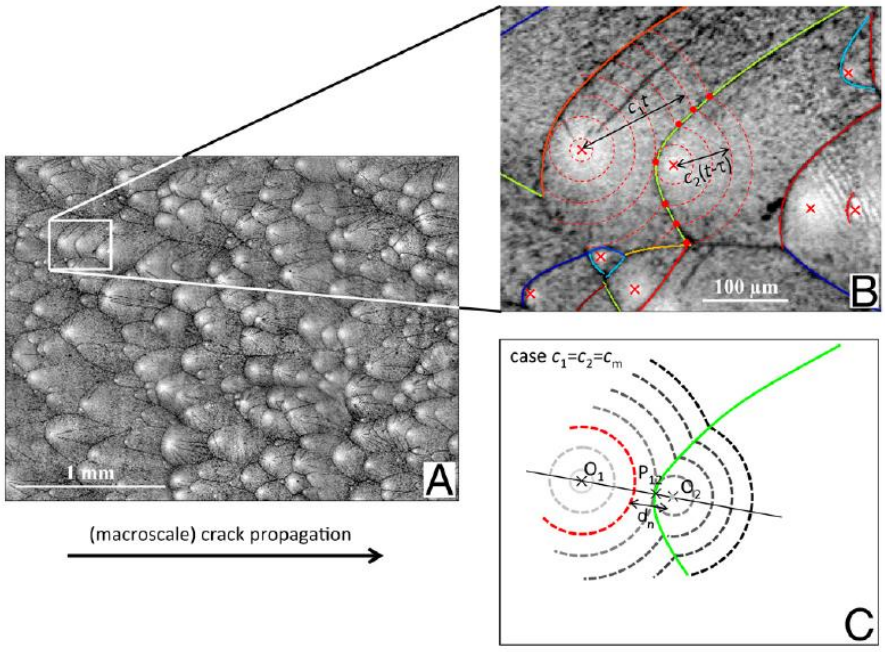

FIGURE 1.7: Fracture surface of PMMA at $v > v_a$ containing conic surface markings from [GUE 12].

image of the fracture surface correspond to the nucleation points of each microcrack. The microcracks expand radially along a slightly different plane with the main fracture surface [SHI 91], and they subsequently coalesce with the crack front propagating from left to right that generate the conic markings. Furthermore, it is found that the density of conic markings increases with the SIF since the size of the process zone increases and triggers the nucleation of more microcracks [RAV 97, SCH 10]. Hence, the microcracks dissipate more energy and contribute to the increase of Γ.

2.4 Micro-branching instability

When the energy flow into the crack is high enough, the crack can bifurcate into several macroscopic cracks. [YOF 51] first suggested a critical crack propagating velocity of $0.6c_s$, where c_s is the transverse wave speed, based on the calculation of velocity-dependent stress field near the head of the propagating crack. It was found that, above this velocity, crack bifurcations occur due to the deviation of the maximum normal stress component ahead of the crack tip. However, experimental observations where the crack bifurcations occur at $0.18c_R$ - $0.35c_R$ in glass [ANT 70] and at $0.34c_R$ - $0.53c_R$ in Homalite [ARA 91] imply that there is no critical crack bifurcation velocity.

Differing from the macroscopic crack bifurcations, the microbranching instabilities have been observed in the mist zone in different brittle materials when the crack propagation velocity v reaches a critical value $v_c \simeq 0.3c_R$ - $0.4c_R$ [SHA 96a, SHA 99, LIV 05].

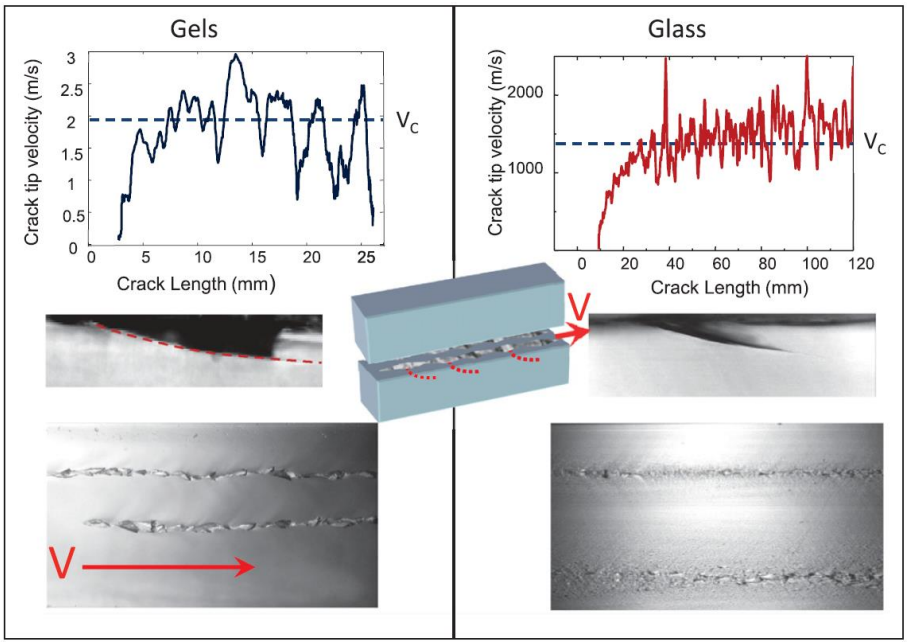

FIGURE 1.8: Microbranching instabilities and crack velocity oscillations in both soft polyacrylamide gels (left) and soda-lime glass (right) reported in [BOU 14].

As shown in Fig. 3.22 They exhibit localized crack branches of micro-scale sizes with a short lifetime, called microbranches, which sprout away from the main crack turning into an unstable state. The microbranches are parallel to the propagation direction of the crack and extend in a direction of a certain angle relative to the fracture surface into the material. Their mean length increase with the crack velocity. Since the microbranches lead to the increases of the fracture surface, Γ increases. [SHA 96b, SHA 96a] found that the total fracture surface varies linearly with the energy release rate G, which reveals that the microbranches do not dissipate extra energy and the increase of Γ is due to the increase of fracture surface when microbranches form. Hence, the oscillations in the crack propagation velocity are due to the birth and death of the microbranches that generate the fluctuations in the energy flowing into the main crack. It is noteworthy that the high peaks of the crack velocity oscillations, where the crack can be considered as a single entity, can be well described by LEFM [SHA 99]. Moreover, it is found that the formation of the microbranches induces a localized curvature variation of the crack front and the latter may, in turn, lead to the microbranch death [KOL 15].

The question of when the microbranches occur remains subtle. [LIV 05] found that the critical crack velocity v_c is not universal even for a given material, while it is a roughly linearly increasing function of the acceleration of the crack velocity. Moreover, [BOU 15] found that the microbranches can be triggered by an activation threshold $|K_{II}(v)|/K_I(v)$ and its value linearly decreases with the crack velocity. As a result, the microbranching instabilities can occur for a large range of crack velocities $v_c \simeq 0.3c_R$ - $0.9c_R$, while they can be suppressed during the crack propagation with a high acceleration rate and the pure

mode I loading.

2.5 Oscillatory instability

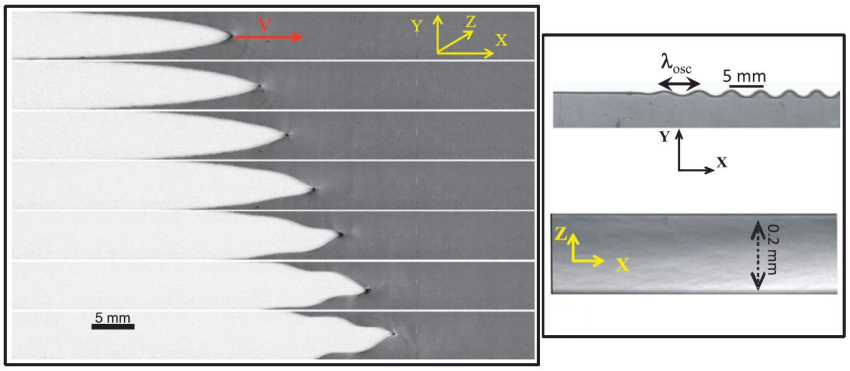

(a)

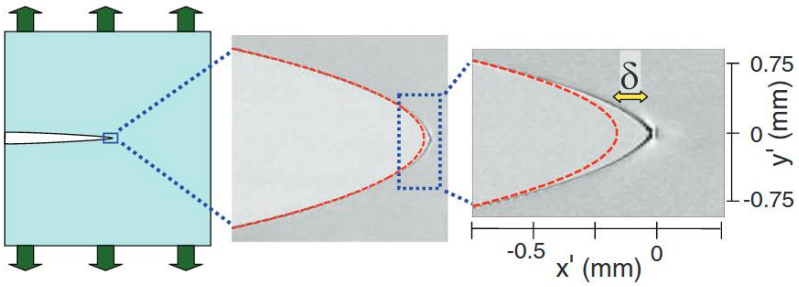

(b)

FIGURE 1.9: (a) Oscillatory instability in the fracture of thin polyacrylamide gels when $v = 0.90c_s$ from [BOU 14]. (b) Profile of the tensile crack tip moving at $v = 0.70c_s$ in polyacrylamide gels from [LIV 10].

When the microbranching instabilities are suppressed, a single crack can propagate at $v \sim c_R$. Meanwhile, another fracture instability, called oscillatory instability, is observed when v reaches about 0.90 c_s [LIV 07, CHE 17], as shown in Fig. 1.9(a). The wavelength of the oscillatory instability λ_{osc} is a linear increase function of the size of dynamic nonlinear zone l_{nl} in the near vicinity of the crack tip, where linear elasticity breaks down [BOU 09a, GOL 12]. Fig. 1.9(b) presents the deviation between the parabolic shape predicted by LEFM and the real crack tip profile δ, incorporating the nonlinear effects in the vicinity of the crack tip at $v = 0.70c_s$, which is proportional to l_{nl}. This instability can not be explained by LEFM and impels the development of new theory to describe the dynamic crack propagation controlled by near-tip nonlinearity [BOU 09a, BOU 09b, CHE 17].

3 Acoustic waves perturbations on moving crack front

Moving crack can emit acoustic waves [THE 84, GRO 93, BOU 98]. These waves, propagating at a speed in the order of few kilometers per second, may interact with the crack and alter its motion. [RAV 84] shows that stress waves could affect the crack propagation direction, speed and may eventually induce the macroscopic crack bifurcations. [GOL 10a] reports that when an accelerating crack meets the shear waves, which generated at the crack initiation, after reflection at the sample boundary, Eq. 1.8 fails to describe the crack motion since the crack acquires inertia and exhibits a $\dot{v}$ dependent motion [MAR 91].

Instead of significantly changing the crack motion, local interaction of the crack front and acoustic waves slightly perturb the crack front and leaves localized markings on the fracture surface.

3.1 The Wallner lines

The Wallner lines (Fig. 1.10(a)), named by H. Wallner who first interpreted them on the fracture surface of the glass plates [WAL 39], are specific fracture surface markings that record the interaction between the crack front and acoustic waves. As illustrated in Fig. 1.10(b), when the crack front meets an edge defect of material, acoustic waves are emitted and propagate independently on the crack front. The Wallner lines are then generated by the successive interaction between the crack front and the acoustic wave front. According to the generation mechanism of the Wallner lines, one can notice that the shape of the Wallner lines depends on the crack velocity, the acoustic wave speed, and the crack front shape. Hence, one of them can be deduced through the other parameters. The Wallner lines are usually used to determine the fracture origin and the crack propagation velocity [FIE 71, PAY 76, RAB 06].

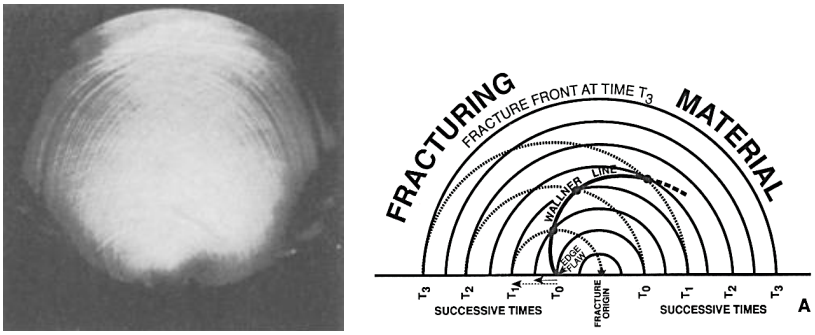

(a) (b)

FIGURE 1.10: (a) Wallner lines on the fracture surface of glass from [WAL 39]. (b) Schematic draw of the generation of the Wallner lines generated from material defects reported in [KUL 95].

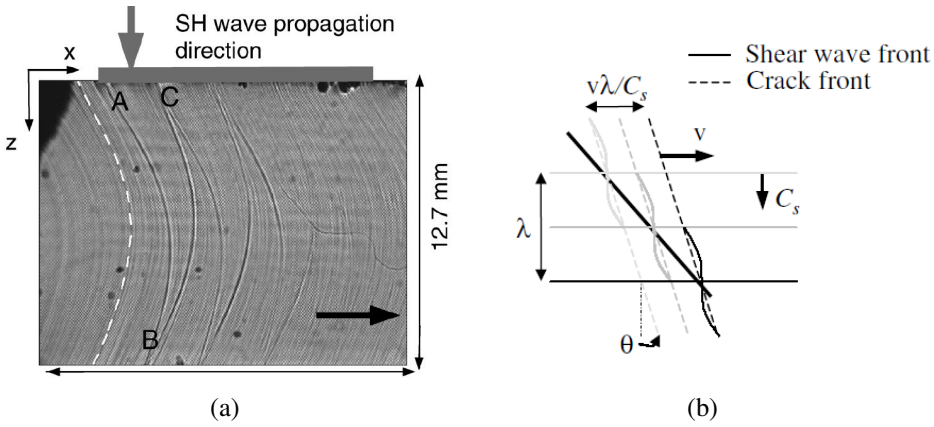

(a) (b)

FIGURE 1.11: (a) The Wallner lines generated by an ultrasonic transducer on the fracture surface of glass from [BON 03]. (b) Schematic draw of local deformation of the crack front perturbed by the shear waves from[BON 03].

How does the crack front locally deform to create the Wallner lines ? To study the localized perturbations of the crack front, controlled Wallner lines generated by an artificial ultrasonic transducer are studied [FIE 71, BON 03, BON 05]. The Wallner lines formation is shown in Fig. 1.11(a) : planar shear waves, propagating from top to bottom along the fracture plane at speed c_s and polarized out of the fracture plane, generate the Wallner lines once interacting with the crack front. Fig. 1.11(b) schematically presents the local response of the crack front when interacting with the shear waves, which involves a spatial and temporal coupling on the crack dynamics. The shear waves generate a mode III loading on the crack front that twists the front out of the fracture surface and leads to fracture surface undulations. As a result, the characteristics of the Wallner lines depend on the attributes of the shear waves. The wavelength of the Wallner lines, λ_{wl}, measured along the crack propagation direction, is given by $v\lambda/c_s$, where λ is the wavelength of the shear waves. Hence, λ_{wl} is invariant during the interaction of a steady-state propagating crack and known elastic waves. Besides, the undulation amplitude of the Wallner lines, A, relies on the amplitude of the shear waves, which follows a $1/r$ or $1/r^2$ decay as a function of the extending distance r, as presented in Fig. 1.12 from [BON 05].

3.2 Crack front wave perturbations

Crack front waves, another localized perturbative source on the crack front, were reported. [RAM 97b] first showed analytically that, when a tensile crack front propagates in an ideal linear elastic material, it supports a propagating mode along the crack front when encountering local material heterogeneities. This mode progresses at a speed slightly lower than c_R and its effects on crack front shape depend on the fracture toughness. [MOR 98, MOR 00] then reproduced this propagating mode in the simulations of dynamic mode I crack growth at constant fracture energy. They found that persistent *linear* elastic waves, called crack front waves, are generated in response to a localized hetero-

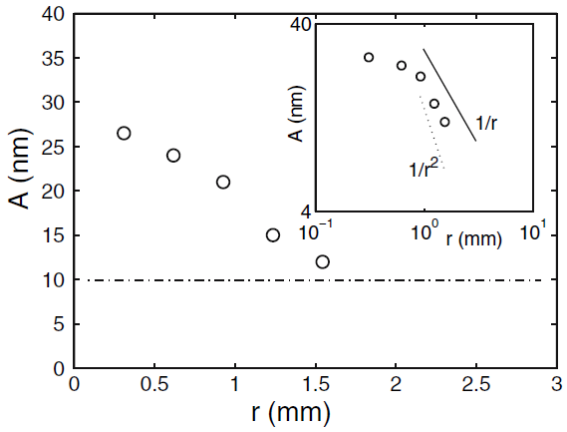

FIGURE 1.12: Undulation amplitude of the Wallner lines A as a function of the propagation distance of the shear waves reported in [BON 05].

geneity of fracture toughness of a crack front. The persistence of crack front waves was revealed by their exponential decay during which the crack front waves travel with long lifetime maintaining nearly constant amplitude. However, these works treated the 2D case where the crack front remains planar. Although the in-plane crack front waves can lead to a wavy crack front, they would not perturb the fracture surface leaving specific markings.

The out-of-plane nature of crack front waves was suggested by [ADD 13] inspired by the work of [WIL 97]. Small perturbations on the crack front like the microbranching event may lead to the out-of-plane propagating mode along the crack front (called corrugation waves) progressing at speed close to the in-plane crack front waves. Besides, the authors showed that the corrugation waves emerge at a critical velocity, $v_c(\nu)$, depending on the Poisson ratio of the material ν.

Since the corrugation waves cause the out-of-plane deviation of the crack front, one may expect them to leave specific markings on the fracture surface. [BOU 02] suggested that the corrugation waves could generate a self-affine fracture surface that can be characterized by a roughness exponent of $\zeta \simeq 0.5$. Fracture tests on soda-lime glass and PMMA sheets with intentional material asperities were carried out by [SHA 01, SHA 02, FIN 03] to generate corrugation waves. The asperities were introduced in the crack path by filling surface flaws with super glue adhesive, which induces localized fracture toughness heterogeneities. The corrugation waves were emitted when the crack front meets the asperities and left surface markings (see Fig. 1.13(a)). Besides, the authors showed that microbranching instabilities, which induce fracture energy fluctuations, can also trigger front waves (see Fig. 1.13(b)). Coinciding with the theoretical prediction, experimental observations showed that the corrugation waves propagate at approximately c_R and exhibit an exponential decay after an initial $1/r^2$ decay (see Fig. 1.13(c)). Fig. 1.13(a) shows the persistence of the corrugation waves, which undergo multiple reflections at the sample surfaces. Besides, in contrast to the analytical prediction, experimental results show that, after decay, the corrugation waves contain a scale-independent shape when scaled by the width of asperities, which evidences the *nonlinear* attribute of corrugation waves (see Fig. 1.13(d)).

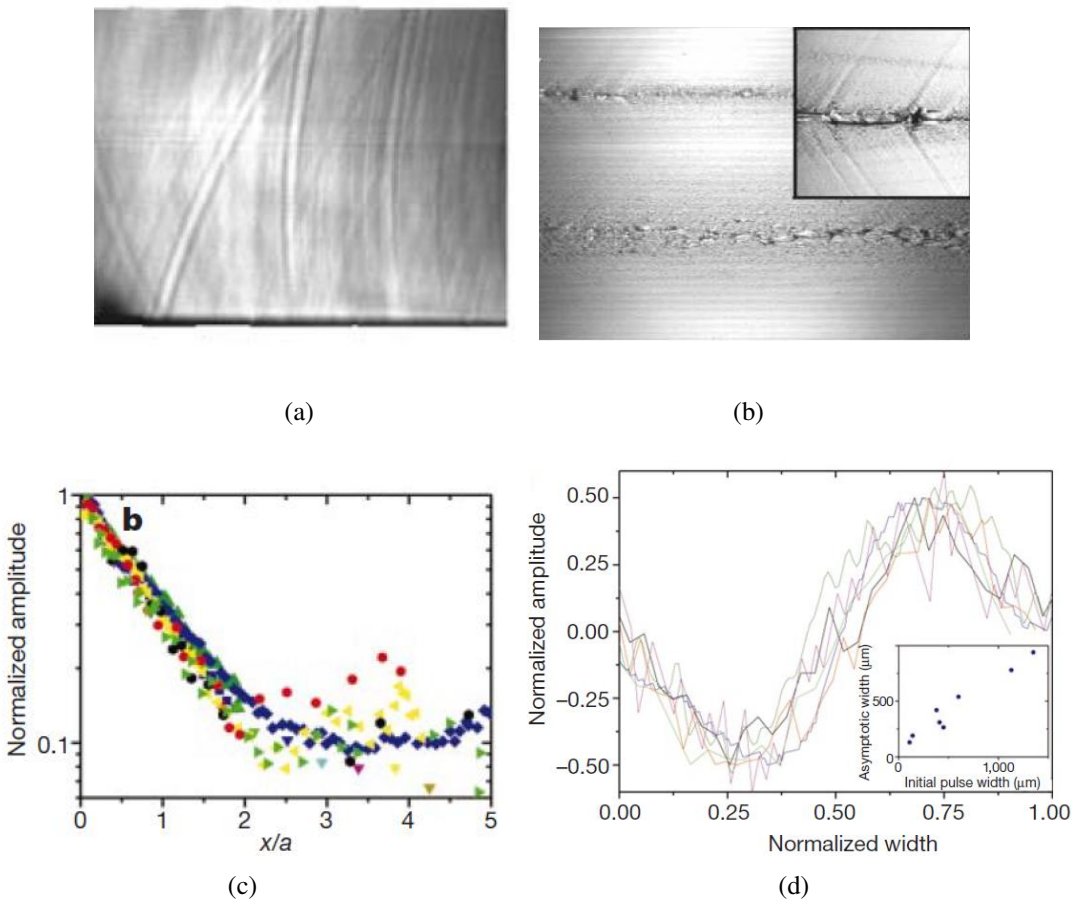

FIGURE 1.13: Front wave traces on the fracture surface of soda-lime glass generated from asperities (a) and microbranches (b) from [FIN 03]. Decay profiles (c) and scale-independent shape (d) of front waves from[SHA 01].

4 Fracture instabilities in silicon crystal

Until now, we have presented the experimental observations of various dynamic fracture behavior in brittle fracture of isotropic amorphous materials. The crack growth in a silicon crystal, due to anisotropic properties of silicon, exhibits more intriguing fracture behavior in link to the crystal lattice structure.

4.1 Low-speeding fracture instabilities

Although the fracture of silicon can be considered as ideal brittle at room temperature and the crack-tip plasticity is immune [LAW 93], the Griffith criterion (Eq. 1.3) is not sufficient to describe the crack growth in silicon crystal because of fracture instabilities at the atomic scale. For the crack initiation along the (111) cleavage plane (the crystal plane and direction notion can be found in Section. 1.1), a localized phase transformation of the

silicon lattice from 6-member rings to a 5-7 double ring at the crack tip (see Fig. 1.14) have been observed via molecular dynamics (MD) simulations [BUE 07]. This transformation blunts the crack tip at initiation and induces that the energy needed to break the 5-7 double ring γ_{5-7} is about 2.2 times larger than the (111) surface energy γ_{111}. As a result, once initiating, the crack instantaneously accelerates to a velocity of about 2 km/s. This phenomenon implies the possible existence of a velocity gap in silicon between 0 to 2 km/s [HAU 99]. However, experimental measurements of crack moving at speed lower than 1% of c_R [BEE 03, RAC 16] and atomistic calculations predicting extremely low speed in silicon crystal [KER 15] suggested that the crack velocity gap is not universal.

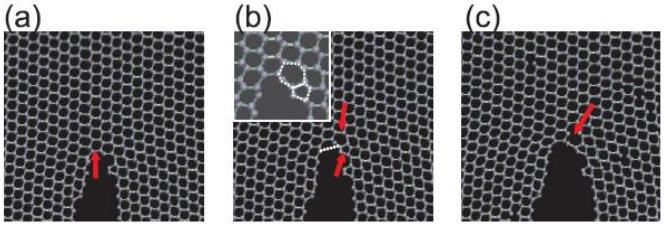

FIGURE 1.14: Transformation of the silicon lattice from 6-membered rings to a 5-7 double ring reported in [BUE 07].

During the crack propagation in silicon, MD simulations [PÉR 00b, PÉR 00a] revealed that the discontinuous bond breaking process manifests a lattice trapping effect, which depends on the crystallographic direction along which the bond breaks. For instance, the crack growth on the (110) plane along the <001> direction involves a strong lattice trapping effect, which induces that the crack propagation along the (110)<001> direction can not be achieved. Latter, [KER 08a] indicated that a (110)<001> crack would easily deflect to the (111) plane under any slight shear disturbance through MD simulations (see Fig. 1.15(a)). Furthermore, when the crack slowly grows along the (111)[1-10] direction, [KER 08a] also found the 6-7 member ring transformation. They observed that the breaking of subsequent 6-member rings after reconstruction of 7-member rings yields the step instabilities on the (111) cleavage surface (see Figs. 1.15(b) - 1.15(c)). The authors later found that the deflection of the step from the original plane can be induced by a crystal defect such as a single dopant atom [KER 13].

4.2 High-speeding fracture instabilities

Experimental investigations [CRA 00, SHE 04, ZHA 17] showed that when a single crack propagates in silicon single crystal wafers under mode I load, after the acceleration regime, the crack speed v can reach up to 0.8 - 0.9c_R and maintain at a steady-state regime, as shown in Fig. 1.16).

[CRA 00] found that for the tensile crack propagating along the (110)<1-10> direction at about $v < 0.6c_R$, the fracture energy Γ is nearly constant and equals to 2γ, while it sharply increases when v increases (see Fig. 1.17). Jointly, fracture surface instabilities arise. Fig. 1.17, adapted from [CRA 00], shows the fracture surface of (110) cleavage

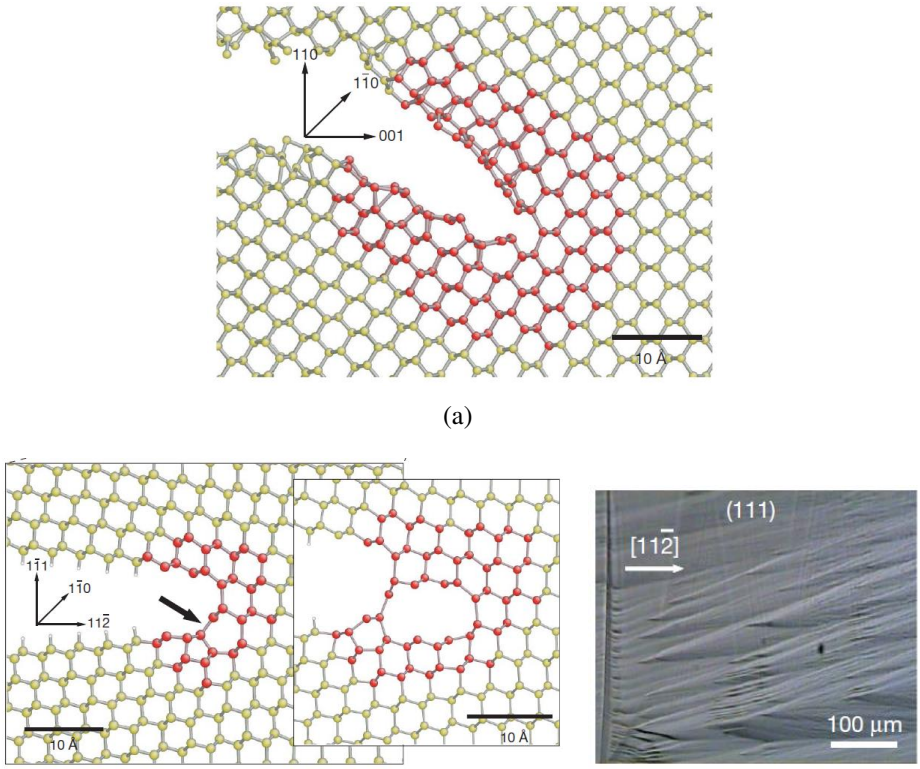

FIGURE 1.15: (a) MD simulations show the crack deflection from (110)<001> direction to (111)<11-2> direction. (b) Breaking of the 6-member rings after a reconstruction of 7-member rings and (c) step instabilities on the (111) cleavage plane from [SHA 01].

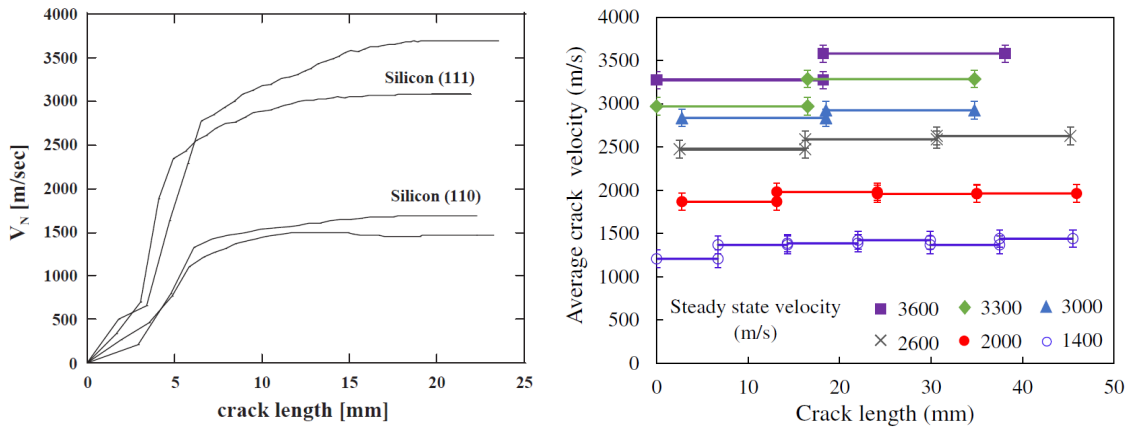

FIGURE 1.16: Crack velocity versus crack length measured by potential drop method [SHE 04] and by high-speed camera in fracture tests of silicon wafers under bending [ZHA 17].

plane of silicon wafer fractured under tension loads with v of about $0.8c_R$. Differing from previous fracture instabilities of amorphous materials at high-speeding crack propagation, the fracture surface of silicon plate is mainly mirror-like in the center of the fracture surface and is accompanied by tiny hackle zones consisting of $\{111\}$ facets near the sample surface. The author revealed that, albeit the occurrence of hackle zones, the energy dissipated by the $\{111\}$ facets is much lower than the significant increase of Γ. Hence, they conclude that the additional energy must be consumed by phonon emission.

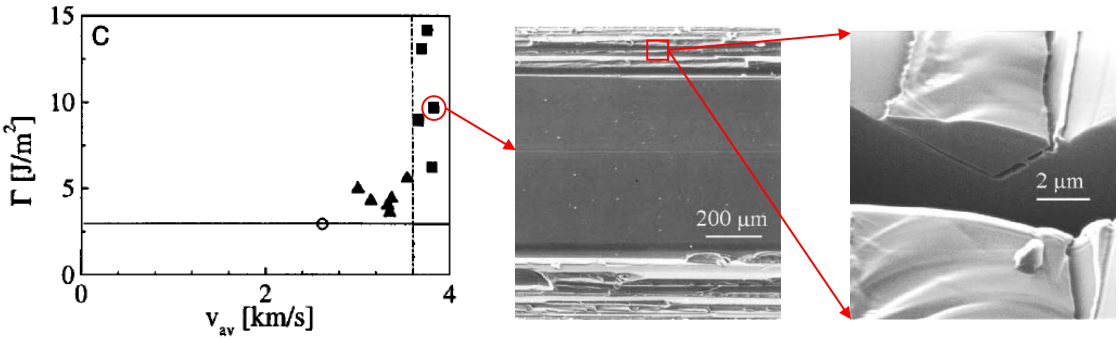

FIGURE 1.17: Fracture energy as a function of the crack velocity along the (110)<1-10> direction and fracture surface morphologies of the (110) plane adapted from [CRA 00].

Crack deflection instabilities have been first observed by [SHE 03b, SHE 04, SHE 05] in the (110) cleavage tests. As shown in Fig. 1.18, they found that when the crack velocity $v < 1560$ m/s, the crack propagates stably along the (110) cleavage plane owing to the lower fracture toughness. However, the crack deflects from the (110) plane to the (111) plane, which exhibits higher fracture toughness at higher crack velocity, and the crack entirely propagates along the (111) cleavage plane at $v > 2900$ m/s. Based on these phenomena, the author suggested that the dynamic fracture toughness of the (110) cleavage plane grows faster than the dynamic fracture toughness of the (111) plane. Hence when the crack velocity reaches a critical value, the (110) plane is no more energetically prevailing (see Fig. 1.19(a)), and the (111) plane would dominate the crack path.

This assumption was further validated by MD simulations on the rapid crack propagation along different crystallographic directions of silicon crystal [ATR 11a, ATR 11b]. The authors showed that the total fracture energy calculated by MD simulations, G_{MD} is larger than the energy needed to drive the crack propagation at velocity v, $\Gamma(v)$ according to LEFM (Eq. 1.7). The additional energy G_{MD} - $\Gamma(v)$ was considered as energy dissipated by thermal phonon emission, G_{ph}. As shown in Fig. 1.19(b), G_{ph} is strongly dependent on the crystallographic direction along which the crack extends. This induces the different growth rates of the dynamic fracture toughness. As a result, the preferential cleavage path would change during crack propagation. Based on these results, crack deflection instabilities at other cleavage systems are also revealed by [ATR 12].

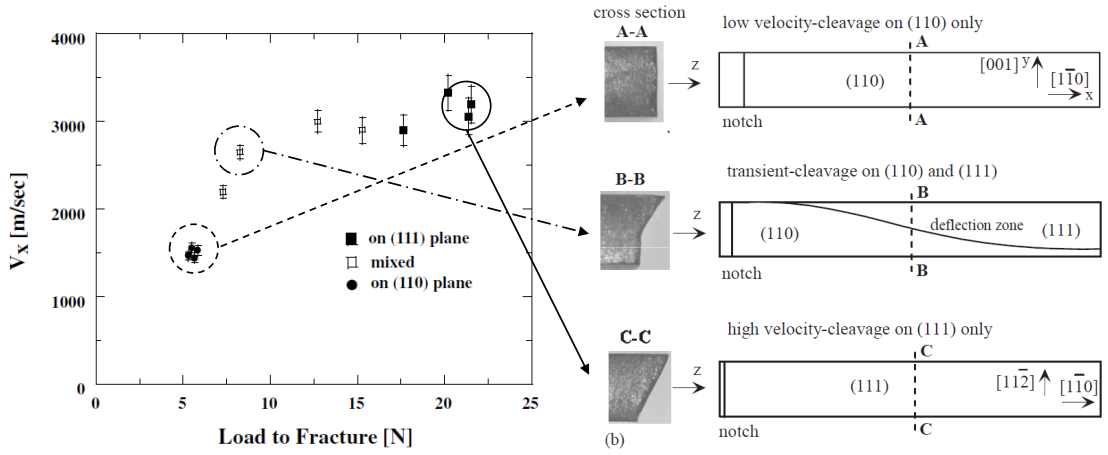

FIGURE 1.18: (110)-(111) cleavage plane deflections under three-line bending tests adapted from [SHE 04].

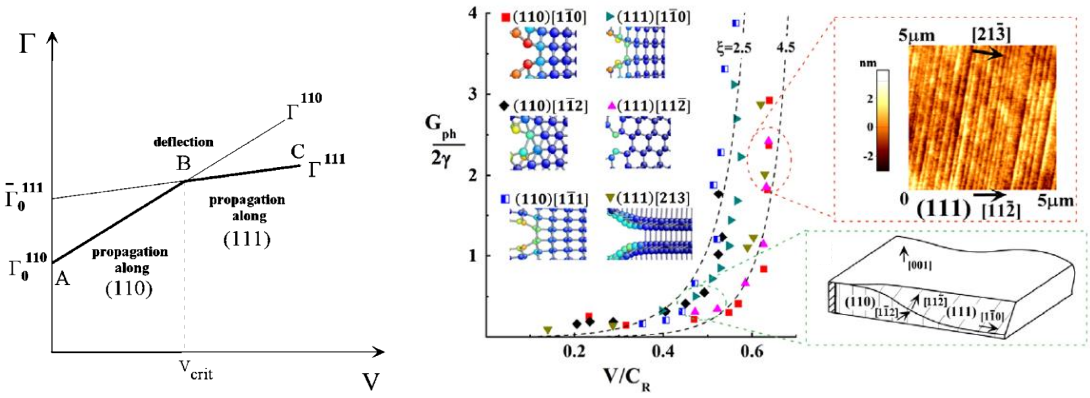

FIGURE 1.19: (a) Assumption of the dynamic fracture energy evolution of the (110) and (111) cleavage plane from [SHE 04]. (b) Crystallographic direction dependent energy dissipated by phonon emission as a function of the crack speed from[SHA 01].

5 Open questions

LEFM is a powerful way to describe the crack motion even for out-of-plane crack front perturbations, whereas it may fail to predict the crack behavior in silicon crystal due to atomic bond breaking instabilities. Atomic calculations on crystals would be necessary. MD simulations on the fracture of the silicon crystals have provided view-points at atomic scale on the origin of some fracture instabilities. However, how does the occurrence of the fracture instabilities at the atomic scale manifest in the macroscopic fracture instabilities in experiments still involve an open discussion.

Even though the MD simulations on the (110)<1-10> - (111)<112> deflection, as well as the crystallographic dependent dynamic fracture toughness evolution evidence the

possible nature of the crack deflection, [ZHA 18a] showed that, under four-line bending tests where the crack propagates between the punch rollers, the crack stably propagates along the (110) cleavage plane without deflection to the (111) plane, even when the crack speed reaches up to 3700 m/s. This result is in contrast with the crack deflection instabilities observed under three-line bending tests in which the crack propagates under the punch roller. Hence, besides the crack deflection instabilities occurring at several crystallographic directions, there must exist other mechanisms that induce the total crack front deflection from the (110) plane to the (111) plane under three-line bending tests.

Besides, in the brittle fracture of amorphous materials, the increase of fracture surface is responsible for the jump of dynamic fracture energy that governs the crack motion, as outlined in Section.2.4. However, instead of an increase of fracture surface, we have seen in Section. 4.2 that the dynamic fracture of silicon crystal is rather accompanied by phonon emission processes, depending on crystallographic directions, inducing a dynamic fracture energy jump. It is not clear yet, can the crystallographic dependent fracture energy jump be revealed by the macroscopic crack propagation ? How does this fracture energy jump controls the crack front motion, considered in the framework of LEFM ? How can the crack front dynamics be experimentally observed during dynamic crack propagation in silicon crystal ?

Moreover, interactions of the crack front with the acoustic waves in amorphous materials is mentioned in Section. 3.1. How does the crack front deform in silicon crystal in response to small, linear perturbations ? Whether the interaction of a moving crack front with a localized material asperity generates linear or nonlinear perturbations to the crack front remain unclear [SHA 04, BON 04]. Would the front waves occur in asperity-free crystalline materials and what is the source of front waves ? The front waves are distinct nonlinear entities and their attributes require further characterization.

Chapter 2

Fracture experiments on solar-grade silicon wafers

In this chapter, we introduce the basis of fracture property of silicon crystal and the manufacture of crystalline silicon wafers. Preparation of different silicon samples is outlined. Dynamic fracture experiments, jointly with high-speed crack velocity measurement method are presented.

Contents

1 Material

1.1 Silicon crystal and cleavage plane

Silicon crystallizes in the same structure as diamond, which is a faced-centered cubic lattice. The crystal structure is illustrated in Fig. 2.1. Each atom connects with four neighbor atoms via covalent bonds. Each of the eight atoms on the corners is repeated among each lattice, each of the six atoms at the center of faces is shared among two lattices and four extra atoms rest completely inside the lattice. The edge of the cubic lattice is 0.543 nm.

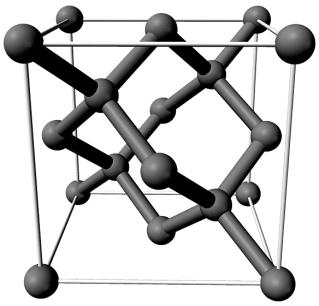

FIGURE 2.1: Face-centered cubic crystal structure of silicon

The crystal planes and crystallographic directions in a crystal lattice is determined by the Miller indices, denoted as *h, k* and *l*. Defining three lattice vectors $\mathbf{a}_1$**,** $\mathbf{a}_2$ and $\mathbf{a}_3$ forming the lattice axes of a unit lattice cell, any crystal plane would intersect the axes at three distinct points $\mathbf{a}_1/h$, $\mathbf{a}_2/k$ and $\mathbf{a}_3/l$. That is, the Miller indices are obtained by taking the reciprocal of the intercepted values and the crystal plane is defined as (hkl). If the planes do not intersect of axes, the related indices are zero. The lattice vector $\mathbf{a} = h\mathbf{a}_1 + k\mathbf{a}_2 + l\mathbf{a}_3$ denotes the crystallographic directions, defining as [hkl]. In other word, in a cubic lattice, a lattice vector **a** passing from the origin to a lattice node (h,k,l) determines the Miller indices. The crystal direction [hkl] is along the vector **a**, and the crystal plane (hkl) is orthogonal to the lattice vector **a**. In general, the adopted nomenclature corresponding the crystal planes and directions are described as below :

- A single crystal plane is represented by [hkl]
- The equivalent planes are denoted by {hkl}
- A single crystal direction is represented by [hkl]
- The equivalent directions are denoted by <hkl>

For example, Fig. 2.2 shows the {100} planes, {110} planes and {111} planes in a silicon crystal lattice. If we position a silicon single crystal in a Cartesian coordinate system, duo the symmetry of the cubic structure, it has 24 equivalent positions and hence the crystal planes in each family are identical.

The crystallographic directions and planes of silicon are geometric relations linking atoms of a crystal. The properties of the silicon crystal will be different at some directions and on some planes, which have different density of atoms, such as elastic modulus,

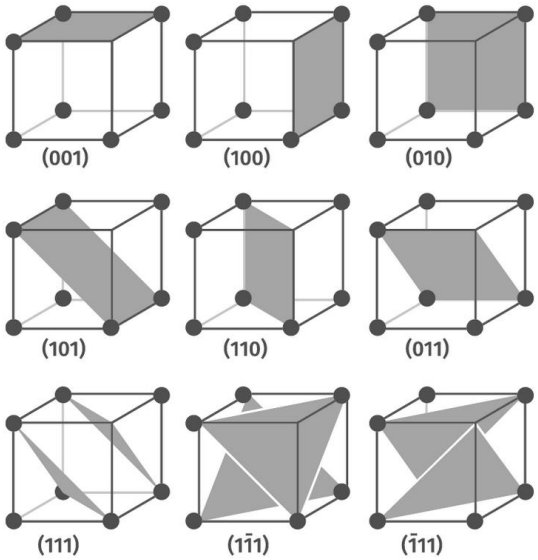

FIGURE 2.2: Crystal planes in a silicon single crystal

optical properties, thermal properties, and electrical properties, etc. In particular, this anisotropy can be also reflected on the fracture behavior of silicon.

Definite crystal planes along which the fracture of silicon splits are called cleavage planes. Crystal planes with low surface energies are the preferential cleavage planes that are dominant in the fracture process of an anisotropic crystal material. In crystalline silicon, it is reported that the $\{111\}$ and $\{110\}$ planes are the two preferential cleavage planes that exhibit lower toughnesses than other planes. A calculation of surface energy of silicon crystal planes based upon the atomic bonds density on the surface of planes [HES 93] is shown in Table 2.1. These results emphasized the lower surface energies of $\{111\}$ and $\{110\}$ but also suggests the possible cleavages of silicon on other crystallographic planes.

TABLE 2.1: Calculated surface energies of silicon crystal planes [HES 93]

Crystal plane	Surface energy (J/m^2)	Crystal plane	Surface energy (J/m^2)
(100)	1.99	(110)	1.41
(111)	1.15	(210)	1.78
(310)	1.89	(410)	1.94
(211)	1.63	(311)	1.80
(411)	1.88	(221)	2.00
(331)	1.72	(320)	1.80
(322)	1.65	(433)	1.45
(522)	1.46	(332)	1.65

1.2 Crystalline silicon wafer

As the dominant semiconducting material in photovoltaic systems, crystalline silicon is widely used for the production of wafer-based solar cells. It could be either monocrystalline silicon that contains a continuously single crystal or multicrystalline silicon that consists of multiple small crystals with grain sizes varying from 1 mm to 10 cm. Besides, polycrystalline silicon (grain sizes between 1 μm to 1 mm) and microcrystalline silicon (grain sizes < 1 μm) are also used.

• Monocrystalline silicon wafer

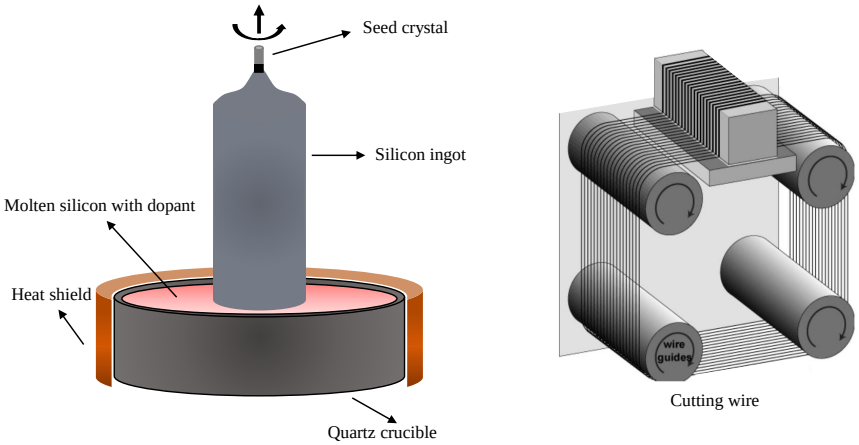

(a)

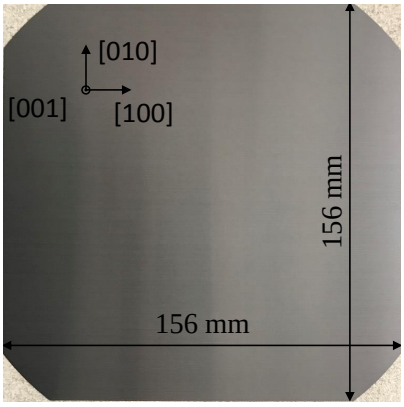

(b)

FIGURE 2.3: Manufacture of monocrystalline crystalline silicon wafer by Czochralski process (a), and the (001) monocrystalline silicon wafer (b).

Monocrystalline crystalline silicon wafers fabricated by the Czochralski (CZ) process [CZO 18] are the most widely used in the industry. The CZ process to manufacture a single crystalline silicon ingot is illustrated in Fig. 2.3(a). A crystal seed is dipped into the molten silicon with boron or phosphorous dopants. The silicon crystal solidifies by

rotating and pulling up under the lead of the crystal seed to keep the same crystallographic direction with the seed. The solidified silicon ingot is then cut into small ingot bricks at the size of the wafer and is finally sliced up into thin wafers with the diamond-wire sawn technique. The damaged outer layer of wafers is cleaned up by chemical etch to remove a thin layer. The dimension of 156 *times* 156 *times* mm^2 of the wafer is presented in Fig. 2.5(b), with a thickness of 190 μm. Nowadays, some novel sawing techniques are developed to manufacture thinner wafers to increase productivity [YU 12].

• Multicrystalline silicon wafer

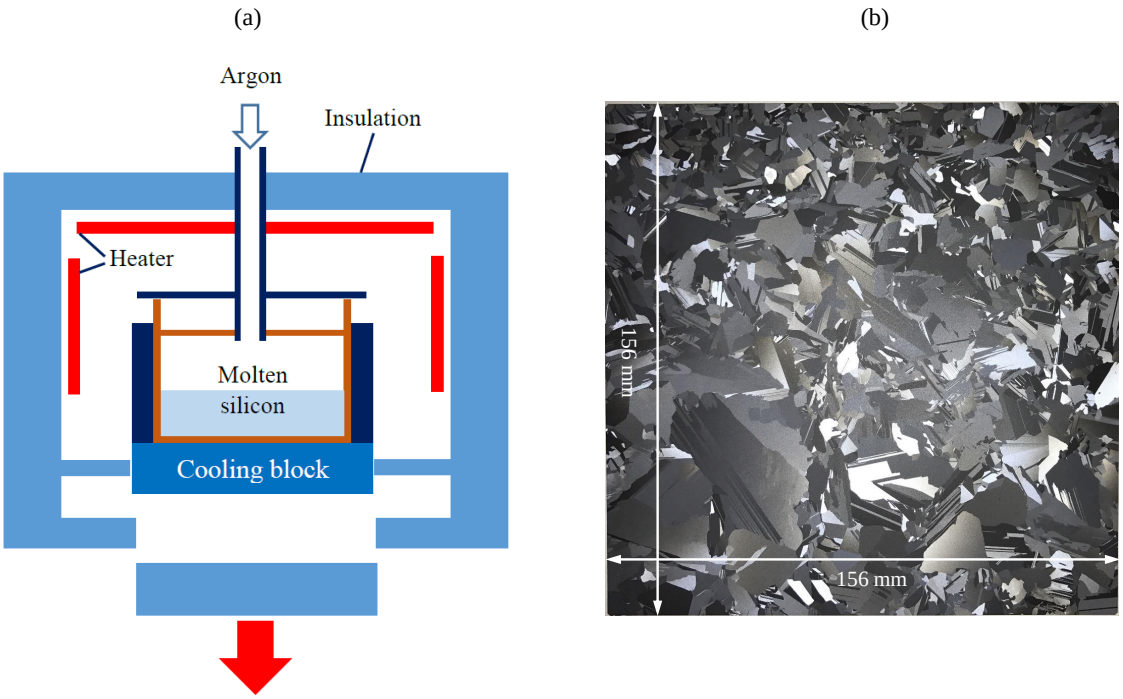

FIGURE 2.4: Manufacture of multicrystalline silicon wafer [ZHA 16b] (a), and the multicrystalline silicon wafer (b)

The manufacture of Multicrystalline silicon wafers is simpler, hence cheaper than that of monocrystalline silicon wafers using the CZ process. A schematic of the manufacture of multicrystalline silicon ingot is shown in Fig. 2.4a. Solid pieces of pure silicon filled in the crucible coated with silicon nitride are heated until the silicon melts. The crucible is then cooled by thermal extraction by moving downwards so that silicon crystal grow upward within the molten silicon. Meanwhile, the crucible is flushed with argon to avoid the oxidation. Large silicon grains are generated under well-controlled temperature in the hot zone. The solidified ingot is then removed from the crucible and finally sawed into silicon wafers. Fig. 2.4b shows a look on the top surface our multicrystalline silicon wafers. Most grains are of centimeter sizes. The grain shapes, as well as the grain boundaries can be directly identified by the naked eye due to different light reflections of different

crystallographic planes. The reflected light intensity of grains can help to distinguish the grain orientations [PAG 18].

The material quality of multicrystalline silicon wafers is lower than that of single crystalline wafers due to the occurrence of grain boundaries generated by the recombination of distorted silicon single crystal. Grain boundaries introduce energy band gaps that blocks carrier flows. Besides, they provide shunting paths for current flow across the p-n junction and thus reduce solar cell performance.

1.3 As-sawn single crystalline silicon specimens

The specimens were obtained by cleavage of diamond wire-sawn (001) single crystalline silicon wafers. As illustrated in Fig. 2.5(a), the single crystal is oriented such that the specimen surface is perpendicular to the [001] direction and the two edges are parallel to the <110> directions. The position of the (110) and (111) plane is illustrated in Fig. 2.5(a). The size of the specimen is $50\times50\times0.19$ mm^3. Fig. 2.5(a) shows the surface morphology measurement of a part of the wafer (1000 x 1000 μm), measured by laser scanning profilometer (Altisurf-500). The spatial resolution (in-plane) is 0.5 μm and the vertical resolution (out-of-plane) is up to 0.5 nm. The wire sawing traces can be observed at an angle of 45° relative to the edge of the specimen. It is found that the root mean squared of the surface roughness Rq is 1.025 μm. Meanwhile, surface defects such as surface peaks with height up to 17.524 μm and hollows with depth down to 11.023 μm were identified.

1.4 Surface-polished single crystalline silicon specimens

Mirror-polishing on silicon sample enable to eliminate the wire-sawn defects, hence permit to suppress the occurrence of Wallner lines generated from the sample surface defects during the crack propagation. The surface mirror-polished silicon samples were prepared from the as-sawn (001) single crystalline silicon wafer. A 10 μm out layer was cleaned up by mechanical polishing for both surfaces of the as-sawn silicon wafers. Mirror-polished silicon sample of size of $50 \times 30 \times 0.17$ mm^3 were then cleaved from the surface polished silicon wafers. The single crystal for all sample is oriented such that the surface of specimens is perpendicular to the [001] direction and the two edges are parallel to the <110> directions.

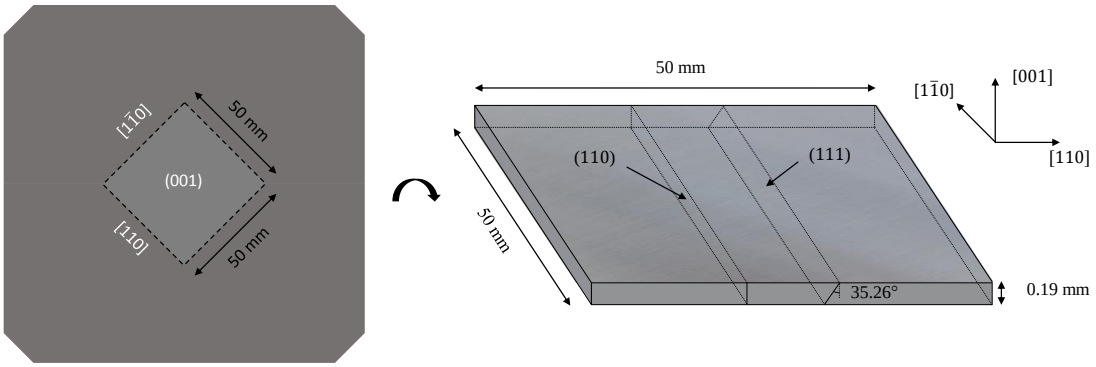

(a)

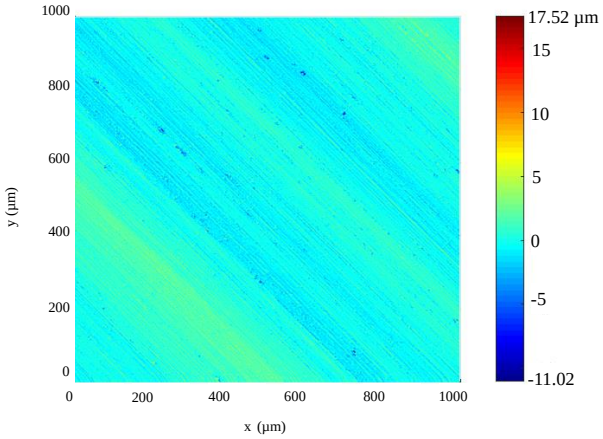

(b)

FIGURE 2.5: Geometry and crystallographic orientation of the single crystalline silicon specimen (a), and distribution of the wire sawing traces and roughness of the specimen surface (b).

2 Three-line bending test on as-sawn single crystalline silicon wafer

The first series of fracture experiments were conducted on as-sawn single crystalline silicon specimens with a three-line bending apparatus, to study the fracture behavior of silicon crystal under line-contact.

2.1 Three-line bending tests

The three-line bending configuration is shown in Fig. 2.6. The punch roller has a radius of 3 mm and the two support rollers involve a contact span of 40 mm. A quasi-static loading, *i.e.* a strain rate in the order of 10^{-6} s^{-1}, was ensured by a LLOYD-Ametek LF-

PLUS electro-mechanical machine under controlled displacement conditions. The strain rate is calculated by :

$$\dot{\varepsilon} = \frac{6h\dot{\delta}}{L^2} \tag{2.1}$$

where L and h correspond to the span of the support rollers and the thickness of the specimen, respectively, and $\dot{\delta}$ corresponds to the loading velocity of the punch roller. The vertical displacement and the reaction force on the punch roller were continuously recorded during the tests.

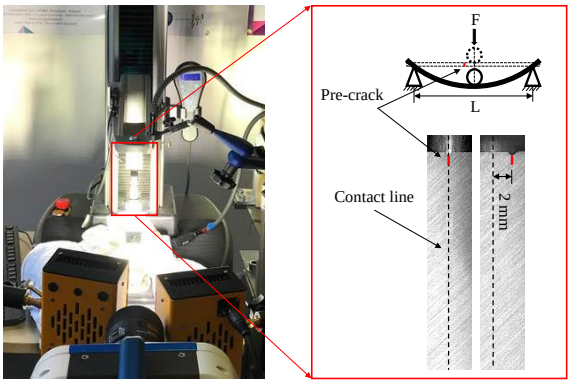

FIGURE 2.6: Three-line bending configuration. Pre-crack positions are illustrated on the right.

In the fracture of single crystalline silicon wafer under bending, it has been shown that, when the bending load is high enough, after the initiation of a first single crack, multiple cracks may occur subsequently and the wafer will break into more than two pieces [KAJ 11, ZHA 18b]. One of the reasons of this phenomenon is that under bending, the crack initiation is followed by the sudden relaxation of the curvature of specimens that will generate a burst of flexural waves, which will, in turn, increase the local deformation of specimens beyond their limit curvature and will finally induce cascading cracks [AUD 05a]. To avoid multiple-cracking, a pre-crack was made at an edge of each specimen using a Vickers indent. The indentation force is well controlled to obtain a sharp pre-crack of desired length varying from 235 µm to 2880 µm. In this case, a single crack is expected to initiate and propagate from the pre-crack. To investigate the contact effect, the pre-crack was located either in the mid-plane of the edge thus right under the contact line, or shifted off 2 mm. This distance was chosen to ensure that a single crack would initiate from the edge pre-crack instead of a surface defect.

According to the beam theory, the maximum tensile stress at fracture, σ_f, was estimated by the following equation :

$$\sigma_f = \frac{3F(L/2 - \Delta L)}{bh^2} \tag{2.2}$$

where F denotes the loading force at failure and ΔL represents the shift distance between the pre-crack and the contact line (0 mm or 2 mm in our tests). L, b and h correspond to the span of the support rollers, the width and the thickness of the specimen, respectively.

2.2 Crack velocity measurements

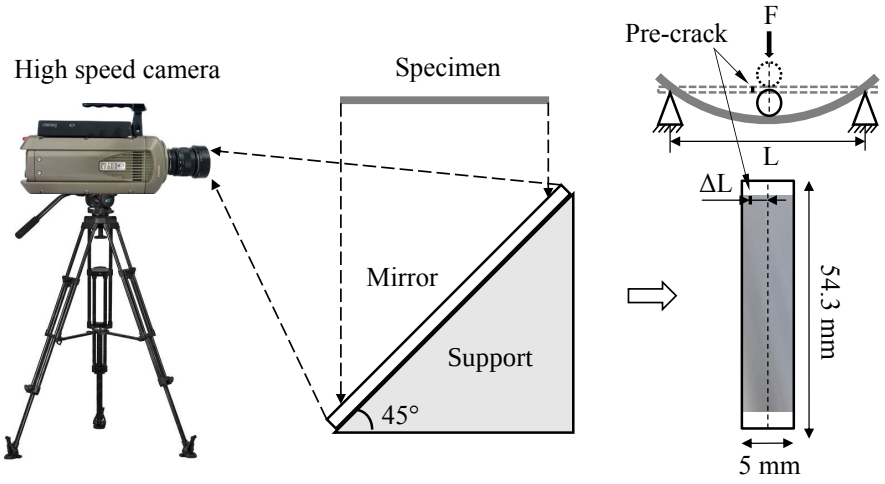

FIGURE 2.7: High-speed camera setup

A high-speed imaging technique, schematically presented in Fig. 2.7, was jointly instrumented with the aforementioned bending setup to record the fracture process of the bottom surface of the specimen. Since setting up the camera directly below the specimens can not be achieved, a tilted mirror with an inclination angle of 45° was placed right between the two support rollers. The crack was captured by a high-speed camera (Phantom V710) set in front of the mirror. We recorded images at an acquisition frequency of 180 kHz and image resolution of 608×56 pixels (corresponding to 54.3 × 5 mm^2). Both exposure time of 0.29 µs and 0.7 µs are used to investigate the influence of exposure time on the crack velocity measurement. A continuous light source (MultiLED G300) was used (see Fig. 2.6) to ensure a good light intensity. The high-speed camera was triggered by an automatic trigger based on the variation of luminosity, since the reflected light intensity of the specimen changes once the crack propagating. A continuous record mode of the camera was used and images during ± 1s around the trigger moment were saved to ensure the record of the entire fracture process. The crack length was disclosed by the subtraction between adjacent images and a wavelet algorithm to suppress the image noise. The crack propagation velocity was then computed with the time gap (5.556 µs) and the growth of crack length.

2.3 Results

2.3.1 Pre-crack length versus fracture stress

Seventy-five tests were performed with various sizes of pre-cracks and two different pre-crack positions. Two examples of a low fracture load F = 1.274 N and a high fracture load F = 5.325 N are shown in Fig.2.8(a). With the increase of the external load, the specimen follows a linear elastic deformation. The total strain energy U stored in the

configuration of the deformed specimen increases, which corresponds to the area under the load curve. According to LEFM [FRE 98], the pre-crack initiates when the stress intensity factor SIF $K_I = K_c$. Shorter pre-crack length corresponds to higher fracture load. The external load drops once the crack begins to propagate and the stored strain energy dissipates. It can be seen that the entire fracture of the silicon specimens is instantaneous since the load drops instantaneously.

The pre-crack length is measured by the post-mortem fracture surface under a digital microscope (VHX-2000F) as two examples shown in Fig.2.8(a). The correlation between the fracture stress σ_f and the pre-crack length a for all the fracture tests is shown in Fig. 2.8(b). With the pre-crack length decreasing from 2880 µm to 230 µm, the fracture stress increases from 19.13MPa to 177.8 MPa. According to the continuum fracture mechanics [AND 17], the relation between σ_f and a is expected to obey a $1/\sqrt{a}$ relation. The red curve shows a $1/\sqrt{a}$ function. It can be seen that σ_f and a obeys to the $1/\sqrt{a}$ relation at the pre-crack length a > 700 μm, where $\sigma_f < 50$ MPa. The $1/\sqrt{a}$ relation breaks at $\sigma_f > 50$ MPa and a sharp increase of the fracture stress as a function of the pre-crack length a appears at $\sigma_f > 70$ MPa. This variation reveals a sharp increase of the fracture energy at the crack initiation and will be discussed in Section. 4.

2.3.2 Crack velocity versus fracture stress

Two examples of crack propagation captured by high-speed imaging technique are presented in Figs. 2.9 (a) and (b), with a crack propagating at 3158 m/s and 840 m/s, respectively. Image N°0 in Fig 2.9a corresponds to the image of the bottom surface of the specimen without crack propagation and latter images show the post-treated images with the crack propagation. The crack path is straight since the crack propagation follows the cleavage along the [1-10] direction. The crack tip position can be clearly identified by the gradient of light intensity due to the curvature variation around the crack tip, so that the crack length can be determined for the crack velocity calculation computing with the time gap of 5.556 μs. The crack tip position uncertainty of 0.36 mm (4 pixel) due to the image processing is indicated by the yellow bar, which corresponds to a velocity uncertainty of 65 m/s.

Thanks to the continuous light reflection from the specimen surface during the fracture process, it is found that the exposure time of the high-speed camera has little effect on the crack length measurement. The number of measurement points along the crack path is from 2 to 8 depending on the crack propagation velocity. Meanwhile, the velocity variation within each two points can be neglected since the crack propagation length $\triangle$L is nearly constant. It implies that the crack velocity reaches a steady state at an early stage of the crack propagation. The steady-state crack propagation regime agrees well with previous study on tensile tests [HAU 99, CRA 00] and bending tests [BEE 03, ZHA 17]. Since the specimen was loaded in a quasi-static loading that leads to a uniform stress field as well as a homogeneous strain energy distribution along the crack path. After the crack initiation, the strain energy releases to support the crack propagation. A constant strain energy release rate ensure that the crack propagates in a steady-state velocity.

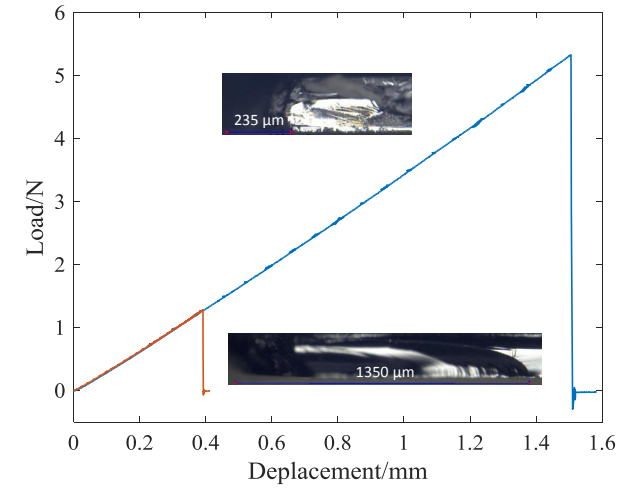

(a)

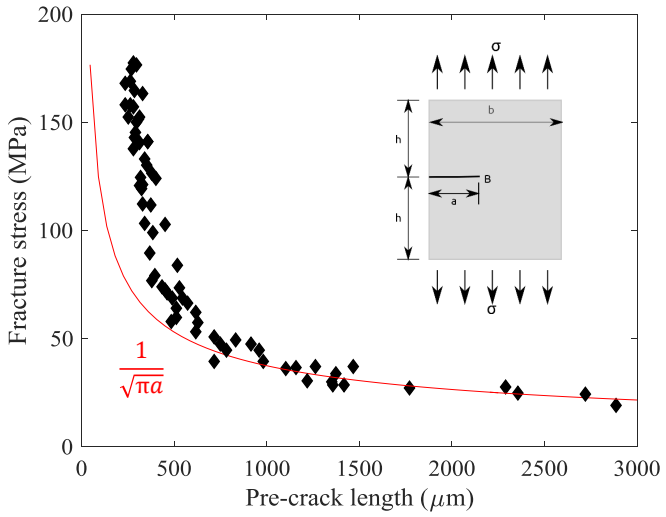

(b)

FIGURE 2.8: Representative experimental force-displacement curve and pre-crack length a (a). Fracture stress σ_f as a function of pre-crack length a (b).

Fig. 2.10 shows the steady-state velocity v_s as a function of the fracture stress σ_f. The crack steady-state velocity v_s varies from 610 m/s to 3780 m/s. A large slope change at around 2700 - 3000 m/s can be observed. It can also be noticed that the steady-state velocity converges towards $0.85c_R$ – the terminal velocity in silicon, where c_R stands for the Rayleigh wave speed along the (111)[1-10] direction here [COU 94]. These results are in good agreement with [HAU 99] and [CRA 00], where the terminal velocity is explained by the additional energy dissipation due to the phonon emission as well as the crack path instabilities such as hackle facets. According to the LEFM, the crack is expected to increase the propagating speed to respond to the increase of energy release rate,

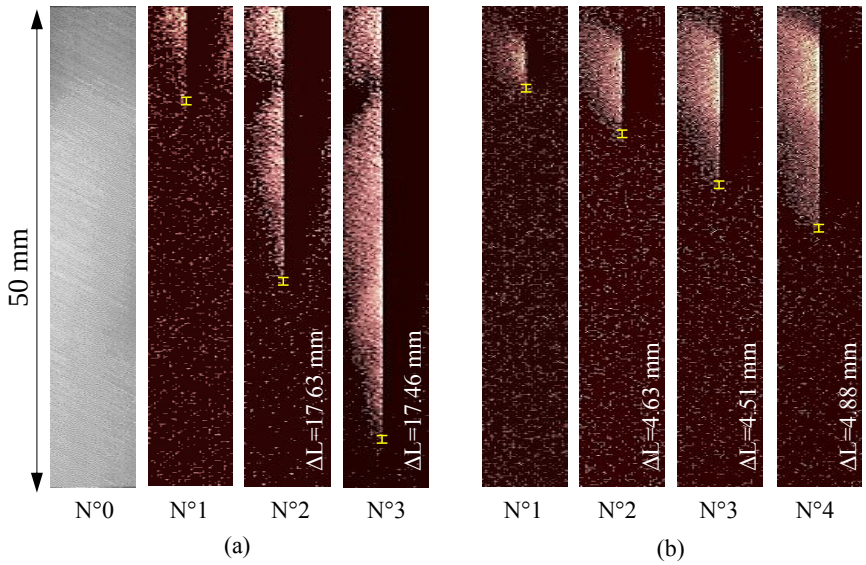

FIGURE 2.9: Crack velocity measurement with high-speed imaging technique for (a) a high crack velocity of 3158 m/s and (b) a low crack velocity of 840 m/s. The yellow bar indicates the uncertainty of the crack tip position (0.36 mm).

and the maximum crack propagation speed is expected to attain the Rayleigh wave speed c_R. However, the occurrence of microscopic crack path instabilities and the thermal phonon emission leads that the fracture energy, Γ, depending on the crack speed and state, increases with the crack speed. Besides, additional energy dissipation accompanied by the twist crack front can also induce the increase of Γ. A constant ratio between increasing energy release rate and fracture toughness results in the terminal crack propagation velocity lower than c_R [CRA 00].

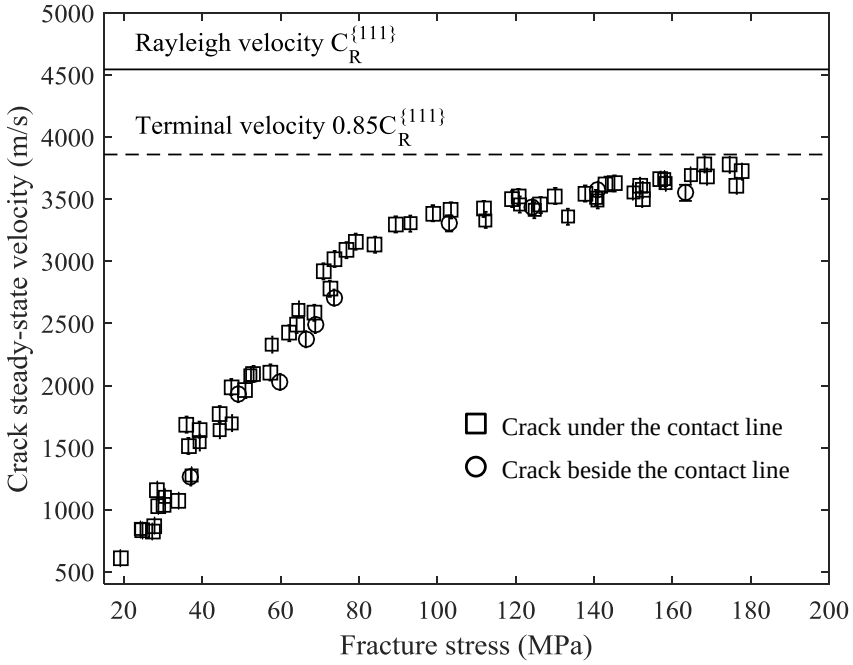

FIGURE 2.10: Fracture stress versus crack steady-state velocity. The two loading configurations are labeled with different symbols. The terminal and Rayleigh velocities are also reported.

3 Four-line bending test on surface-polished single crystalline silicon wafer

It has been shown in Chapter 1 (section 3.1) that the surface flows may generate the acoustic waves that lead to local perturbations on the crack front. To study the crack behavior in single crystal, external perturbations on the crack front need to be suppressed. The second series of fracture experiments were conducted on surface-polished single crystalline silicon wafers under pure bending load.

3.1 Four-line bending tests

Fracture experiments were carried out with standard four-line bending apparatus. The experimental setup is schematically illustrated in Fig. 2.11. The samples were loaded under pure bending condition along the [110] direction (y direction) via quasi-static displacement at a strain rate of $10^{-6}\ s^{-1}$. The strain rate is ensured by :

$$\dot{\varepsilon} = \frac{6h\dot{\delta}}{(a-d)(a+2d)} \tag{2.3}$$

where the spans of the support a and the punch roller d are 21 mm and 40 mm, respectively. h is the sample thickness, and $\dot{\delta}$ is the machine loading velocity.

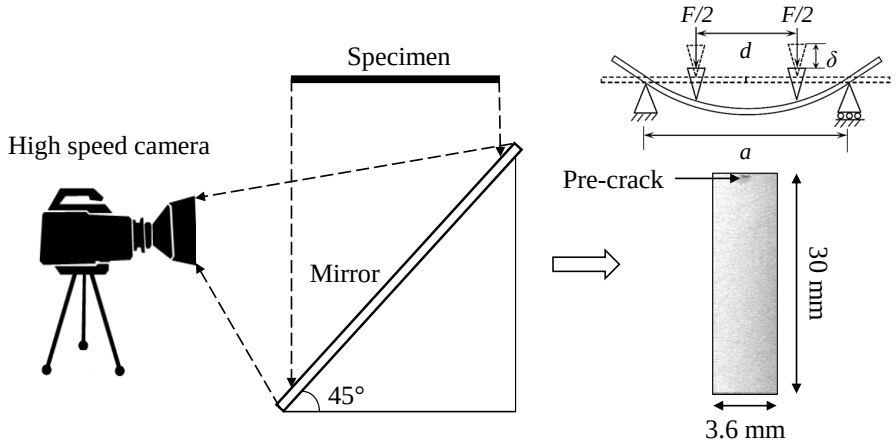

FIGURE 2.11: Experimental setup of four-line bending test.

The fracture stress, σ_f in four-line bending tests was estimated by :

$$\sigma_f = \frac{3F(a-d)}{bh^2} \tag{2.4}$$

where b is the sample width and F is the external load of the machine at the onset of the fracture.

3.2 Crack velocity measurements

A single crack that propagates on the (110) plane was driven from a pre-crack introduced at the center of the sample edge using a Vickers indent. The indentation force was well controlled to obtain a sharp pre-crack of the desired length located on the (110) plane. Fracture process of the bottom surface of the sample was captured with the high-speed camera (Phantom V710). We recorded images at a spatial resolution of 89.3 μm/pixel and an acquisition rate of 340,000 frames per second (the acquisition rate can be increased when the image window is reduced to match the sample dimension). The exposure time of 0.29 μs and the automatic trigger mode was used.

Thirty tests were carried out. Thanks to various seek crack sizes, the steady-state crack velocity v_s varying from 960 m/s to 3600 m/s was obtained. Two examples of the steady-state crack propagation at v_s = 3300 m/s and 1470 m/s, measured by high-speed imaging technique, are shown in Figs. 2.12

The steady-state crack velocity v_s as a function of the fracture stress σ_f is shown in Fig. 2.13. Similar as the v_s-σ_f correlation in three-line bending tests, the crack velocity sharply increases with the fracture stress and a large slope variation takes place at about 2700 - 3000 m/s. Then the crack velocity converges toward a terminal velocity of about $0.84c_R$, which is in good agreement with [CRA 00].

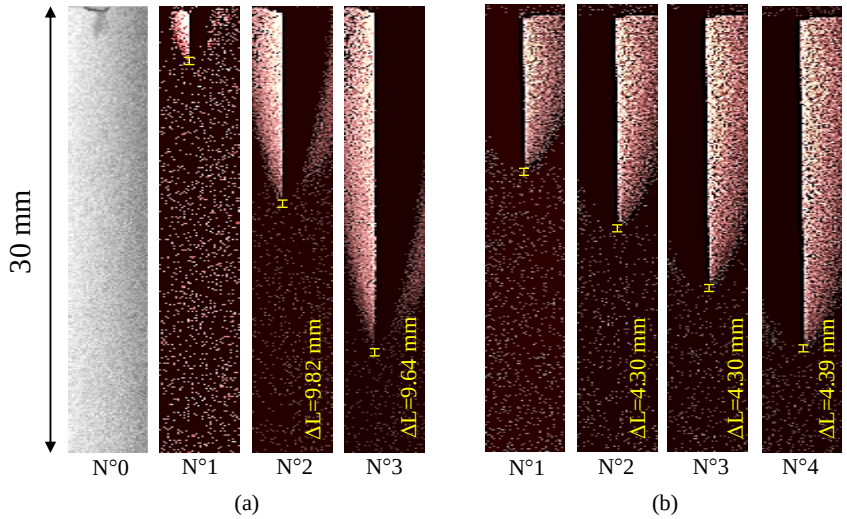

FIGURE 2.12: Steady-state crack propagation in surface-polished silicon wafers in four-line bending tests measured by the high-speed imaging technique with v_s of (a) 3300 m/s and (b) 1470 m/s. The yellow bar indicates the uncertainty of the crack tip position (4 pixels).

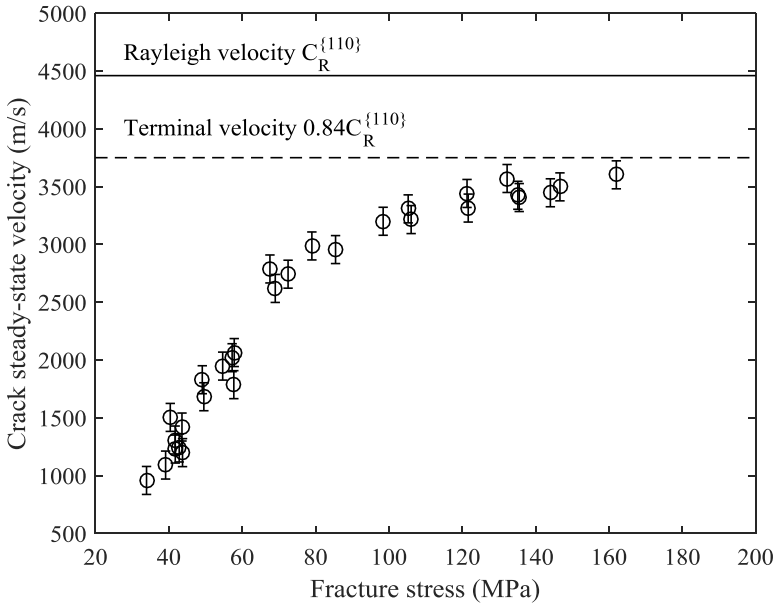

FIGURE 2.13: Fracture stress as a function of the crack steady-state velocity in four-line bending tests on surface polished silicon wafers.

4 Discussion

4.1 High-speed imaging technique

The high-speed photography has been widely used for the dynamic fracture process observation as well as the crack velocity measurement over decades [SCH 55, KNA 85, HAB 11, ZHA 16a]. The advantage of this method is that a direct visual information of fracture process can be obtained without predetermined models to interpret the observations. A good review of the measurement by high-speed photography can be found in [FIE 83]. However, this technique works well in measuring slow fracture but may have some difficulties in fast crack propagation. The first one is the trigger of the camera. The camera can be triggered to capture the entire crack motion only if the crack initiation time is known or detectable signals are output. For example in our tests, the sudden variation of the luminosity upon the crack initiation can trigger the camera. Besides, the sudden drop of the external loads can also be a trigger signal when synchronizes with the electro-mechanical machine. The second one is the exposure time of the camera. For example, for a crack velocity of 3000 m/s, the crack propagates 3 mm during 1 μs. Unless an extremely fine exposure time, the uncertainty of the crack propagation length during the closure of the camera shutter may induce a significant error in the order of the crack velocity. However, this did not occur in our test.

The comparison among the crack velocities measured with the exposure time of 700 ns, 290 ns as well as the crack propagation velocities of silicon wafer under bending presented in the literature measured by potential drop method [BEE 03] and the high-speed imaging technique [ZHA 18a] is shown in the Fig. 2.14(a). We can notice a good agreement among them which ensures the velocity measurement precision in our experiments. As the schematic drawing shown in Fig. 2.14(b), it is worth mentioning that in our velocity measurement, 1) every image capturing is completed when the exposure time is over (the shutter is closed). Nevertheless, between every two images, the crack propagates always during one entire frame interval (which is 1/image frequency), whatever the exposure time. We have used a continuous light source in the experiments, so as long as the shutter is open, sufficient reflected light from the specimen surface will be captured by the camera sensor. This is different from the case with pulsed light, in which the image capturing may be interrupted even when the shutter is open. As a result, we conclude that our crack velocity measurement is reliable and the exposure time has little effect on the crack length measurement in our tests. The third one is that, if the crack velocity is very high, the detail of the crack motion could not be captured since it needs a very high acquisition frequency. This is a limitation of crack velocity measurement in our case since we have only from 2 to 8 measurement points to calculate the crack velocity and the crack acceleration stage can not be measured. To investigate the crack motion in detail, an indirect measurement method based on the fractographic analyses to determine the instantaneous crack velocity will be further presented in Chapter 3 (section 3.5).

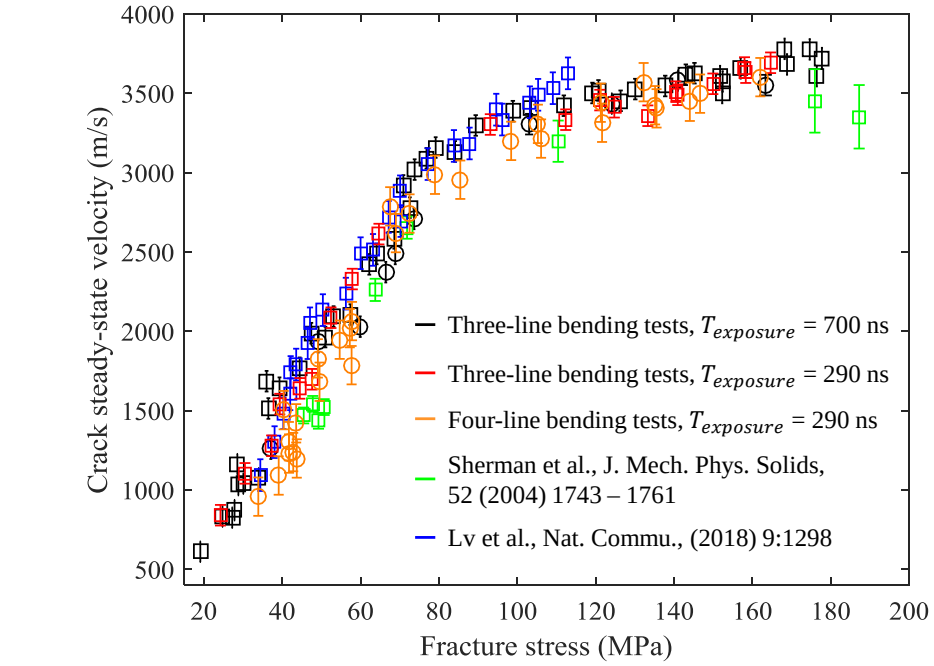

(a)

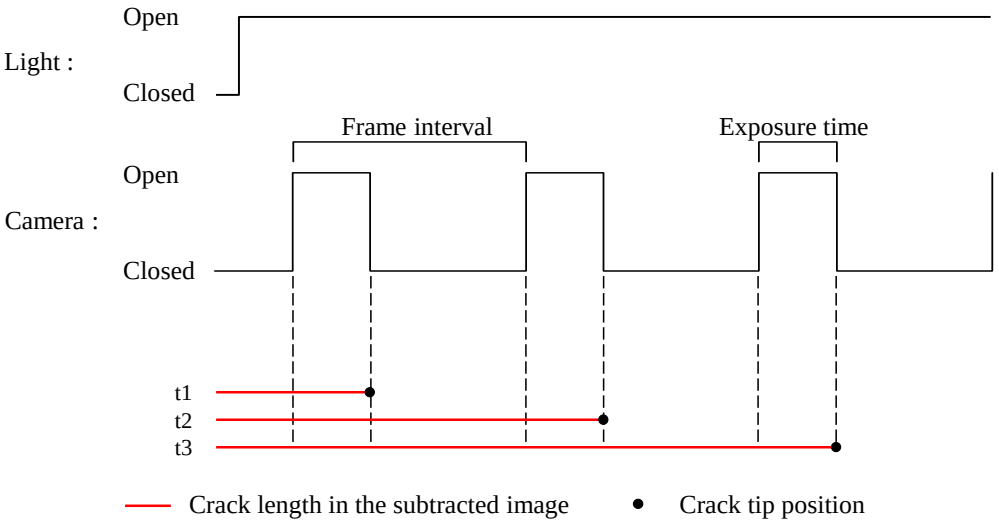

(b)

FIGURE 2.14: Comparison among the crack velocities measured with the exposure time of 700 ns, 290 ns and results presented in the litterature(a). Schematic draw of the principle of the crack velocity measurement by the high-speed camera (b).

4.2 Fracture energy at the crack initiation

In our loading configuration, the crack initiates at the bottom surface of the specimen which is solicited by the maximum tensile stress. [LIU 15] reports that, for a plate having the dimension of 2 h x b which contains an edge crack of length a, as the insert graph shown in Fig. 2.8(b), the stress intensity factor SIF K_I at the crack tip under an uniaxial stress σ can be calculated by :

$$K_I = \sigma\sqrt{\pi a}(1.122 - 0.231(\frac{a}{b}) + 10.55(\frac{a}{b})^2 - 21.71(\frac{a}{b})^3 + 30.382(\frac{a}{b})^4) \tag{2.5}$$

Considering only the bottom surface of the specimen for the crack initiation, since the pre-crack length (0.23 to 2.88 mm) is negligible compared with the dimension of the specimens (50 x 50 mm^2), the Eq. 2.6 can be simplified to :

$$K_I = \beta\sigma\sqrt{\pi a} \tag{2.6}$$

where β is a constant but depends on the loading configuration and the dimension of the specimen. Hence, the relation between the fracture stress and the pre-crack length should obey :

$$\sigma_f = \frac{K_c}{\beta}\frac{1}{\sqrt{\pi a}} = f\frac{1}{\sqrt{\pi a}} \tag{2.7}$$

Since the fracture toughness K_c is material dependent, the factor f is constant and the fracture stress σ_f as a function of the pre-crack length a should obey a $1/\sqrt{\pi a}$ dependency. It was found that in Fig. 2.8(b), the Eq. 2.7 (with f=2) is valid at $\sigma_f < 50$ MPa, which reveal that the crack initiates once K_I reaches K_c. However, the sharp increase of σ_f with a break the validation of the Eq. 2.7, which reveals that SIF as well as the fracture energy at the crack initiation G_0 increase, according to Eq. 2.6. The ratio between the fracture energy at crack initiation and the surface energy G_c can be calculated by :

$$\frac{G_0}{G_c} = (\frac{K_I}{K_c})^2 = \frac{\sigma\sqrt{\pi a}}{f} \tag{2.8}$$

Fig. 2.15 shows that when the crack initiates at very low stress, the fracture energy at crack initiation is approximately equals to the surface energy of silicon. However, the initial fracture energy increases up to 8 times more than the surface energy of the material with the increase of the fracture stress. This result is in a good agreement with [ZHA 17]. The authors found that, based on a finite element analysis, the energy flux ahead the pre-crack at the crack initiation is always higher than the material toughness in silicon. The value of energy flux is comparable to the strain energy release rate during the crack propagation [CRA 00] which results in a non-negligible initial crack velocity. Meanwhile, molecular dynamics simulations [BUE 07] on the crack initiation behavior of silicon cleavage shows that a localized formation of the 5-7 double ring of silicon lattice at the crack tip may have an energy barrier effect to blunt the crack tips and leads to the increase of fracture surface energy. Besides, albeit the Vickers indent produces sharp pre-cracks, small geometrical defects of the crack tip, such as misalignment, could induce the increase of fracture energy at initiation [GLE 14].

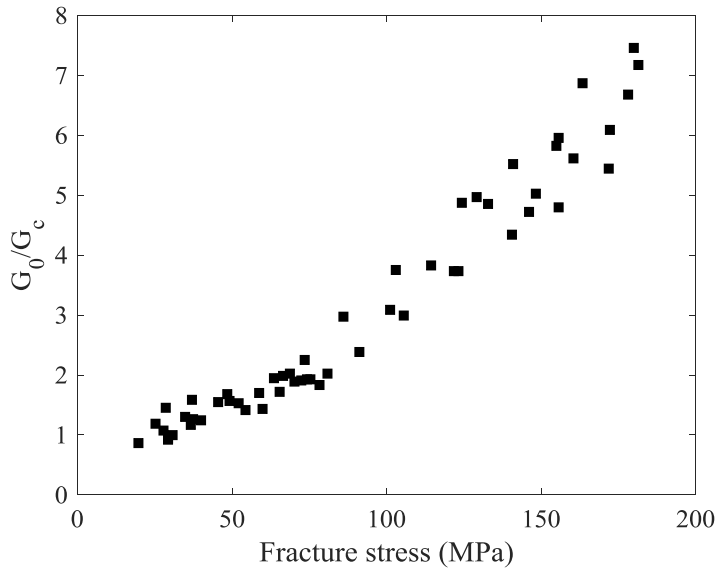

FIGURE 2.15: Ratio between fracture energy at crack initiation and surface energy, G_0/G_c, as a function of fracture stress.

5 Outlook

Figs. 2.10 and 2.14 show that crack steady-state velocity follows the same evolution of the fracture stress in three-line bending tests with crack propagation under and beside the line-contact, as well as in four-line bending tests. Indeed, since the crack initiates at the bottom of the sample surface under bending, and since we captured only the bottom surface of the sample, this correlation could be described by a 2D picture of a crack tip. However, like line-contact effects located on the top of the sample surface, perturbations on the crack along the sample thickness could not be revealed by 2D imaging. How do these perturbations affect the dynamic fracture of silicon crystal ? A 3D crack front must be described.

Besides, it is shown that the terminal velocity of a crack propagating in silicon crystal is much higher than that in amorphous materials. Fracture instabilities would be expected. Considering that the crack front involves stress gradient under bending, how does the crack front behave and what kind of instabilities will occur in such high velocity ? Noting that direct observation of the crack front during the crack propagation in silicon crystal is impractical, fractographic analysis seems to be necessary to reconstruct a 3D picture of the crack front propagation and will be shown in the next Chapter.

Chapter 3

Fractographic examination of as-sawn crystalline silicon wafer

Fracture paths in crystalline solid can be significantly altered upon encountering stress perturbations. Here, based on the Fractographic analysis, we investigate the dynamic cleavage deflection in as-sawn (001) silicon single crystal wafers under three-line bending tests. It is found that the crack propagates preferentially along the (110) cleavage plane. However, when the crack front interacts with shear waves induced by the line-contact, it tends to deflect onto the (111) cleavage plane and forms secondary Wallner lines. Yet, the crack deflection is not permanent and a recovery process to the (110) plane is observed, suggesting that the (110) cleavage plane remains energetically prevailing during the high-speed crack propagation. We show that the ratio between the dynamic fracture energy of the (111) plane and that of the (110) plane at the deflection position is invariably larger than the one when the local crack velocity is lower than 40% of the Rayleigh wave speed. This confirms that the crack deflection is triggered by shear waves. Therefore the theory of crystallographic direction dependence of dynamic fracture toughness evolutions proposed in earlier literature needs to be further assessed before generalization.

Contents

1 Introduction

The mechanical properties of silicon single crystal are highly dependent on the crystallographic orientation. The anisotropy is reflected by not only the elastic moduli, such as Young's modulus and Poisson's ratio [WOR 65, HOP 10, ZHA 16b], but also the fracture behavior [LI 05, PAG 18]. According to the Griffith criterion [GRI 21], the crack initiation in brittle materials takes place once the strain energy release rate, G, exceeds twice the surface energy of the fracture path, namely the fracture toughness, Γ. In this sense, crystal planes with low surface energies are dominant in the fracture process of an anisotropic crystal material. The fracture toughness of silicon has been widely investigated using different experimental techniques, such as double cantilever beam (DCB) set-up [GIL 60, JAC 63], knoop indentation [CHE 80] and double torsion (DT) loading [BHA 86]. It was found that the $\{111\}$ and $\{110\}$ crystal planes exhibited lower toughnesses than other planes and therefore are preferential fracture paths in crystalline silicon. Moreover, an in-plane fracture anisotropy has been identified for the $\{110\}$ cleavage planes. As unravelled by many experimental observations [PÉR 00c, ZHA 18b], the crack stably propagated along the (110)[1-10] path ((110) and [1-10] denote the crack plane and the propagation direction, respectively), while it systematically deflected from the (110)[001] path onto a (111) plane. This observation of in-plane anisotropy was at the origin of numerous investigations at the atomic scale and pushed forward the understanding of the fracture mechanism in silicon. In the light of molecular dynamics (MD) simulations, Pérez and Gumbsch [PÉR 00a] disclosed that under tension, the crack propagation along (110)[001] involved lattice trapping that would prevent the crack front from staying on the (110) plane. Later, the (110)[001] to (111)[11-2] deflection scenario was numerically reproduced by MD simulations using the LOFT hybrid classical/quantum mechanical method [KER 08b]. These various investigations reveal the fact that the Griffith criterion alone cannot predict the fracture of silicon due to the lack of accounting for atomic scale mechanisms.

When fracturing below the brittle-ductile transition temperature, the crack velocity in silicon is very high due to the absence of plastic dissipation and the low fracture toughness [SAM 89, HIR 89]. Fracture speed in silicon has been widely assessed using potential drop method [STA 83, HAU 98, SHE 05]. Recently, a new method based on the correlation between surface morphologies and crack propagation velocities was developed [ZHA 17]. This method enabled to capture a short acceleration phase of the crack that could not be covered by potential drop technique. According to the continuum fracture theories, the crack velocity can reach the Rayleigh wave speed, C_R, when a large enough energy flux flows to the crack tip [FRE 98]. However, a terminal velocity, defined around $0.85C_R$, has been revealed for the (110)[1-10] cleavage under tension [CRA 00]. Up to this terminal speed, the crack mainly propagated in the (110) plane (mirror-like zone), accompanied by tiny (111) facets in the hackle region near the surface of the specimen. Similar fracture behavior was found under four-line bending tests, where the crack propagated along the middle line of the inner contact span [ZHA 17]. Differing from the tensile and four-line bending tests mentioned above, three-line bending load with the (110)[1-

10] path right under the contact line resulted in total crack deflection from the (110) plane to the (111) plane at high crack velocities [SHE 04, SHE 05]. This deflection behavior was explained by a dependence of the fracture toughness as a function of the crack speed to the cleavage plane [ATR 12], without considering the external perturbations from the line-contact. The authors have shown numerically that the dynamic toughness of the (110) cleavage system, Γ_D^{110}, would increase faster than that of the (111), Γ_D^{111}. Hence, the (111) plane would become more energetically favorable when the crack velocity is higher than a critical value. However, in contrast to their former conclusions, Sherman and co-authors recently showed through tensile tests that Γ_D^{110} and Γ_D^{111} barely increase with the crack speed [SHA 18].

In the framework of bending tests, the determination of the crack front is crucial to assess the local crack behavior. [SHE 04] described the crack front shape along the (110) cleavage for low crack speeds by an ideal quarter-ellipse of semi-axes a = 3h and b = 0.85h (where h is the wafer thickness), then they also used this shape to study the local crack behavior in the case of high speed crack propagation. More recently, [ZHA 18a] assessed the (110) crack front shape for high crack speeds, and they highlighted that the crack front varies significantly with the crack propagation velocity and involves a curvature jump at around 2700 m/s.

In this Chapter, we revisit the (110)[1-10] cleavage under contact to confront the contradiction between three-line bending tests and four-line bending or tensile tests, better understand the fracture behavior in the presence of contact perturbations and review the effect of the dynamic fracture toughness evolution on the crack deflection. The results here are obtained from the three-line bending tests on (001) single crystalline silicon wafers presented in Chapter 2 (section 2). A pre-crack is introduced in each test sample to control the crack position and velocity. Two loading configurations are conducted, *i.e.* the pre-crack is located either right underneath the contact line or shifted off 2 mm. The high speed imaging technique is used to measure the crack velocity, and post-mortem fractography is carried out to assess the local crack behavior.

2 Fractographic analysis of single crystalline silicon wafer

Cracks generate intricate fracture morphology on the fracture surfaces due to the local deformation of the crack fronts. High-speed photography provides a direct method to study the local fracture behavior of the transparent material since the transient crack front during the fracture process can be visualized under the high-speed camera [GRÉ 07, HAB 11, KOL 18]. In the case where the visualization of the crack front during the fracture is impossible (the material is nontransparent or the fracture process is faster than the frame rate of the high-speed camera), fractography provides an appealing way to retrospect the 'history' of the crack recording on the fracture surface. It can be used to determine the origin of the failure to reveal the cause of the fracture, identify the types of fracture, study the topographic characteristics to understand crack growth behavior, and

eventually develop new theoretical fracture models [GON 18].

Our fractographic analysis focuses on the fracture surface at both the macroscopic and microscopic scales. The fracture surface of each specimen was firstly assessed by visual examination using a digital microscope (VHX-2000F) to determine the overall fracture surface morphology, such as the fracture initiation and propagation zone, typical fracture surface marks as well as special identities on the fracture surface, etc. The fracture surface was then scanned by the stereoscopic examination using the digital microscope and a laser scanning profilometer (Altisurf-500) which has a maximum out-of-plane precision of 0.5 nm and in-plane resolution of 0.5 μm that provides higher magnification and more information about fracture details, such as height variation of the fracture surface, out-of-plane profiles of the surface marks and fracture surface roughness, etc. The crack surface morphology was finally correlated with the fracture condition and the crack velocity for the further analysis of the fracture mechanics of our specimens.

2.1 Surface morphologies of (110) and (111) cleavage plane

The (110) and (111) plane are the two most energetically preferential cleavage plane due to low surface energies, as mentioned in Section. 1.1. When the specimen is loaded under bending, the (110) plane coincides with the maximum tension plane and becomes the most preferential fracture path ($G_c^{(}110) = 2\gamma = 3.46$ J/m^2 [PÉR 00c]). Note that albeit the (111) plane has a lower fracture toughness, the effective energy dissipation along the (111) plane will be larger than that along the (110) plane due to the 35.26° tilt angle relative to the maximum tension plane ($G_c^{(}111) = 2\gamma/\cos(35.26°) = 3.53$ J/m^2 [SHE 04]). However, both crack propagation along the (110) plane and the (111) plane are observed. Here, we give an overview of the fracture surface morphologies of these planes.

2.1.1 (110) cleavage plane and Wallner lines

Thanks to the given crystallographic structure of the single crystalline silicon wafer, the cleavage planes along which the crack propagates can be obtained by measuring the angle between the fracture plane and the specimen surface. For our specimens, mentioned in Chapter 2 (section 1.3), when the crack takes place on the (110) plane, the fracture surface is perpendicular to the specimen surface. Fig. 3.1(a) shows the surface pattern of the (110) cleavage plane under bending tests. The thickness of the specimens is along the [001] direction and the crack propagation direction is along the [1-10] direction. On the fracture surface, the well-known fracture surface marks - the Wallner lines come into view.

The Wallner lines widely occur in the fracture of brittle materials and provide a post-mortem method to analysis the dynamic fracture behavior [FIE 71, PAY 76, RAB 06, NAR 14]. Fig. 3.1(b) schematically illustrated the formation of the Wallner lines naturally generated from surface defects : when a crack front moving from left to right encounters a surface defect, elastic waves will be released and radially emit from the surface defect due

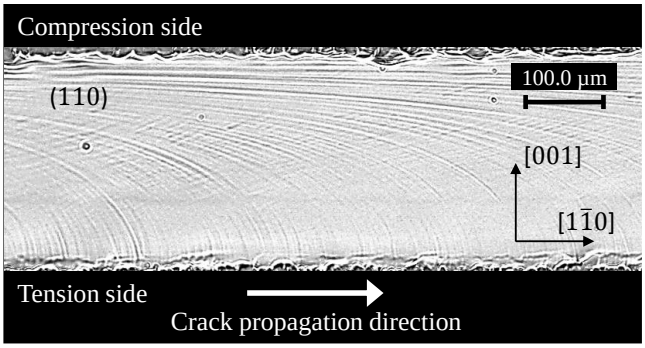

(a)

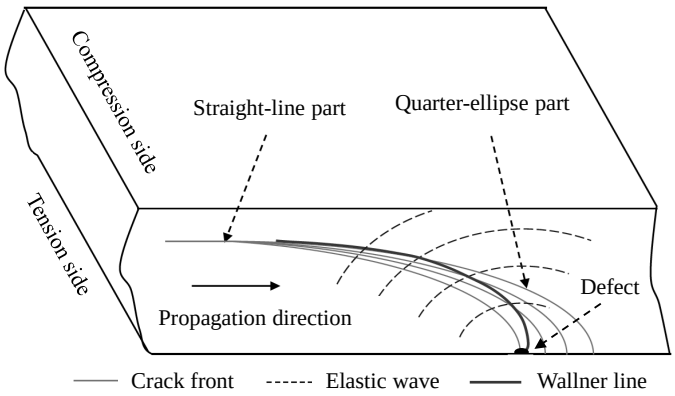

(b)

FIGURE 3.1: Typical Wallner lines on the (110) cleavage plane under three-line bending (a) and the schema of the generation of the Wallner lines from a surface defect(b)

to the sudden variation of the stress field ahead of the crack front. The latter then continuously interact with the moving crack front. Since the shear components of the elastic waves involving mode III fracture leads to the out-of-plane deformation of the crack front, surface undulations will be generated upon crack front-elastic waves interactions forming the Wallner lines. In our tests, due to the wire-sawn defects on the specimens surface, this type of Wallner lines appear on the (110) cleavage plane, as can be seen that generated from surface hollows at the bottom surface in Fig. 3.1(a). The crack propagation direction can be easily identified using the Wallner lines, and thus the fracture origin.

2.1.2 (111) cleavage plane and specific surface instabilities

When the crack takes place on the (111) plane, the fracture surface forms an angle of 35.26° relative to the maximum tensile plane. Instead of the Wallner lines on the (110) cleavage plane, special surface instabilities appear on the (111) plane. Fig. 3.2 shows the fracture surface morphologies of the (111) cleavage plane. The thickness of the specimens is along the [112] direction and the crack propagation direction is always along the [1-10] direction. Two distinguish morphologies on the fracture surface can be observed.

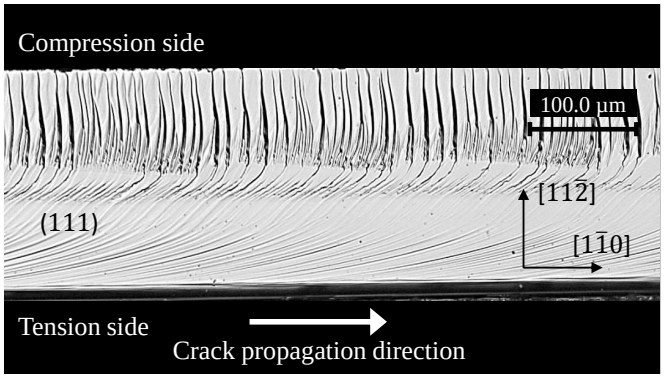

FIGURE 3.2: Optical image of the (111) cleavage plane of single crystalline silicon under three-line bending

The instabilities are as terrace-like kinks on the upper half part and are corrugated structures on the lower half part, as reported in [SHE 03a, SHE 08]. The authors found that the terrace-like kinks instabilities are generated because of the misalignment between the fracture plane and the maximum tensile plane, where shear stress components break the symmetry of the crack propagation, and the perturbations evolve always along the local crack front direction. Besides, the corrugated instabilities which point to the [112] direction are proposed to be generated by the unstable atomic bond breaking. In a word, the characteristics of the (111) surface instabilities provide us the crack propagation direction that allow to locate the crack origin and to investigate the crack front dynamic behavior.

2.1.3 Crack origin identification

Under bending loading, the crack nucleates at the bottom surface of the specimens which is subjected to the maximum tension. With the presence of the artificial (110) pre-crack, the crack initiates from the point locating at the bottom of the pre-crack and propagates along the (110) plane as shown in Fig. 3.3(a)(left inset). The Wallner lines appear around the crack origin and extend to the crack propagation direction. In the absence of the artificial pre-crack, the crack nucleation spot can be determined by tracking the Wallner line evolution. As shown in Fig. 3.3(a)(right inset), the Wallner lines growing in the opposite direction embrace a subsurface micro-crack with a length of about 87 mm that induced by the diamond wire cut. For the crack propagating along the (111) cleavage plane, the crack origin can be identified using specific surface instabilities on the (111) plane. Fig. 3.3(b) shows the crack nucleats from a subsurface micro-crack locating on the (111) plane. The specific surface instabilities extend to the opposite direction relative to the fracture origin.

2.2 Velocity dependent crack front shape

In this section, based on the fractographic analysis, we present the method to determinate the crack front shape during the steady-state crack propagation and demonstrate how

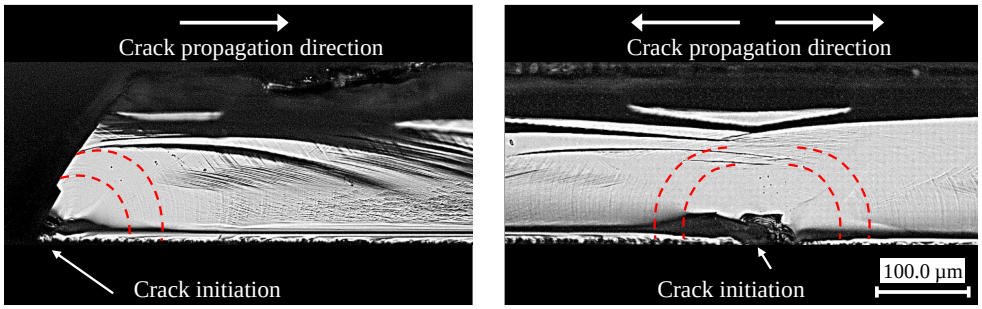

(a)

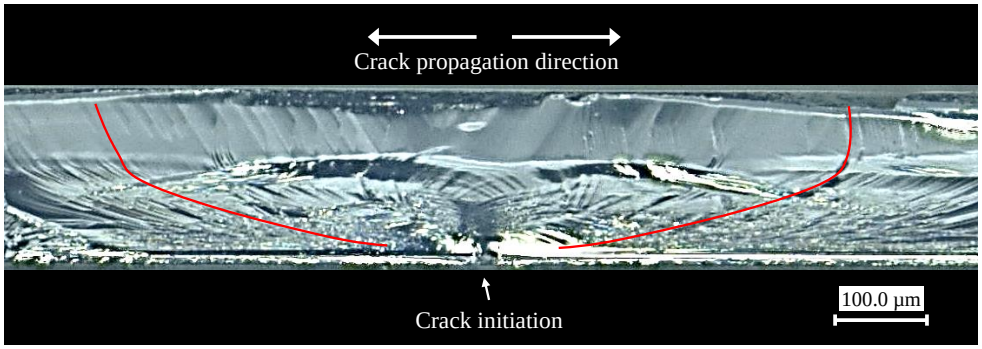

(b)

FIGURE 3.3: Fracture origin identification :(a) crack initiates from the artificial pre-crack (left figure) and a wire-cut induced surface defect (right figure) on the (110) plane. The Wallner lines are highlighted by the red dotted lines (b) Crack initiates from a surface defect located on the (111) plane. The specific surface instabilities are highlighted by the red full lines.

it varies with crack propagation velocity.

Crack shape in plate under bending has been well illustrated by analytical solutions [NEW , NEW 81], numerical analyses [LIN 99, SHI 04] and experimental methods [BEE 03, SHE 04]. When the crack propagates in a bending plate, the stress gradient along the thickness of the plate induces the decrease of the necessary energy release rate along the crack front (from maximum tension side to the maximum compression side) to drive the crack front. According to the LEFM (Eq. 1.8), at a low crack velocity where the fracture energy Γ equals to the material toughness 2γ, the decrease of the energy release rate leads to the decrease of the local crack velocity along the crack front. As a result, the crack front is curved.

As mentioned in the Introduction, in thin silicon wafer under bending [BEE 03, SHE 08] describe the crack front shape during the steady-state propagation along the (110) and (111) plane as an ideal quarter-ellipse, which contains a long 'tail' behind the quarter-ellipse. They find that the top surface of the specimen starts to crack only after full propagation of the bottom surface, so this 'tail' could be as long as the specimen width.

However, here we find that the crack shape behaves as a quarter-ellipse only at the crack speed lower than 2700 m/s. When the crack velocity is higher than 2700 m/s, the crack shape becomes a more complex curve involving a local curvature variation, which varies with the crack velocity, on both (110) and (111) plane.

2.2.1 Velocity dependent Wallner line shape

As mentioned in Section. 2.1.1, when the crack propagates along the (110) plane, the Wallner lines are generated along the fracture surface during the successive interaction of the crack front and elastic waves emitted from surface defects. Based on analysis of the fracture surface correlated with the crack propagation velocity, we found that the shape of the Wallner lines is highly dependent on the crack propagation velocity. In Figs. 3.4, we present the fracture surface morphologies for ten different steady-state propagation velocities. The Wallner lines are highlighted by the red curves. For the crack propagation velocity lower than 2700 m/s, the Wallner lines are a part of an ellipse with a long 'tail' behind at the upper portion, which agrees well with the literature [SHE 08, ZHA 18a]. However, when the crack velocity is higher than 2700 m/s, the Wallner lines show a hook shape containing a local curvature kink, highlighted by the green circle in Fig. 3.4. It can be noticed that the local curvature kink evolves from the bottom to the upper surface of the specimen when the crack velocity increases.

The dependency of the height of local curvature kink of the Wallner lines on the crack propagation velocity provides us a criterion to estimate crack propagation velocity. The constant height of the local curvature kink also reveals that the crack propagates at steady-state velocity as can be seen in Fig. 3.4 when the crack velocity is higher than 2700 m/s.

Based on the formation mechanism of the Wallner lines (see Fig. 3.1(b)) as mentioned in Section. 2.1.1, the shape of Wallner lines is dependent on the crack front shape, the elastic waves speed and the crack propagation velocity. Hence, by knowing the crack velocity and the elastic waves speed, the crack front shape can be determined through the Wallner lines shape, and will be presented in the next section.

2.2.2 Determination of the crack front shape

A simple method to determine the crack front shape [ZHA 18a] is based on the kinetics of the Wallner lines generation as presented in Figs. 3.5(a) and 3.5(b) : for a given Wallner line generated from a surface defect, we choose a fixed time increment Δt and discretize the Wallner line with a couple of (n) stress waves initiating from the same surface defect and radially expanding outward with an interval of $C\Delta t$, where C corresponds to the stress waves speed. Then, by horizontally recovering each discretized point on the Wallner line from bottom to top with translation length of 0, $V_s\Delta t$, $2V_s\Delta t$, ..., $nV_s\Delta t$, we obtain n new discrete points along the crack front. The crack front shape can be finally obtained by connecting these points. It has been reported that when a moving crack in a brittle material crosses a surface asperities [FIN 03, SHA 01], stress waves will be generated which interact with the crack front at the Rayleigh waves speed. Hence, the Rayleigh waves speed

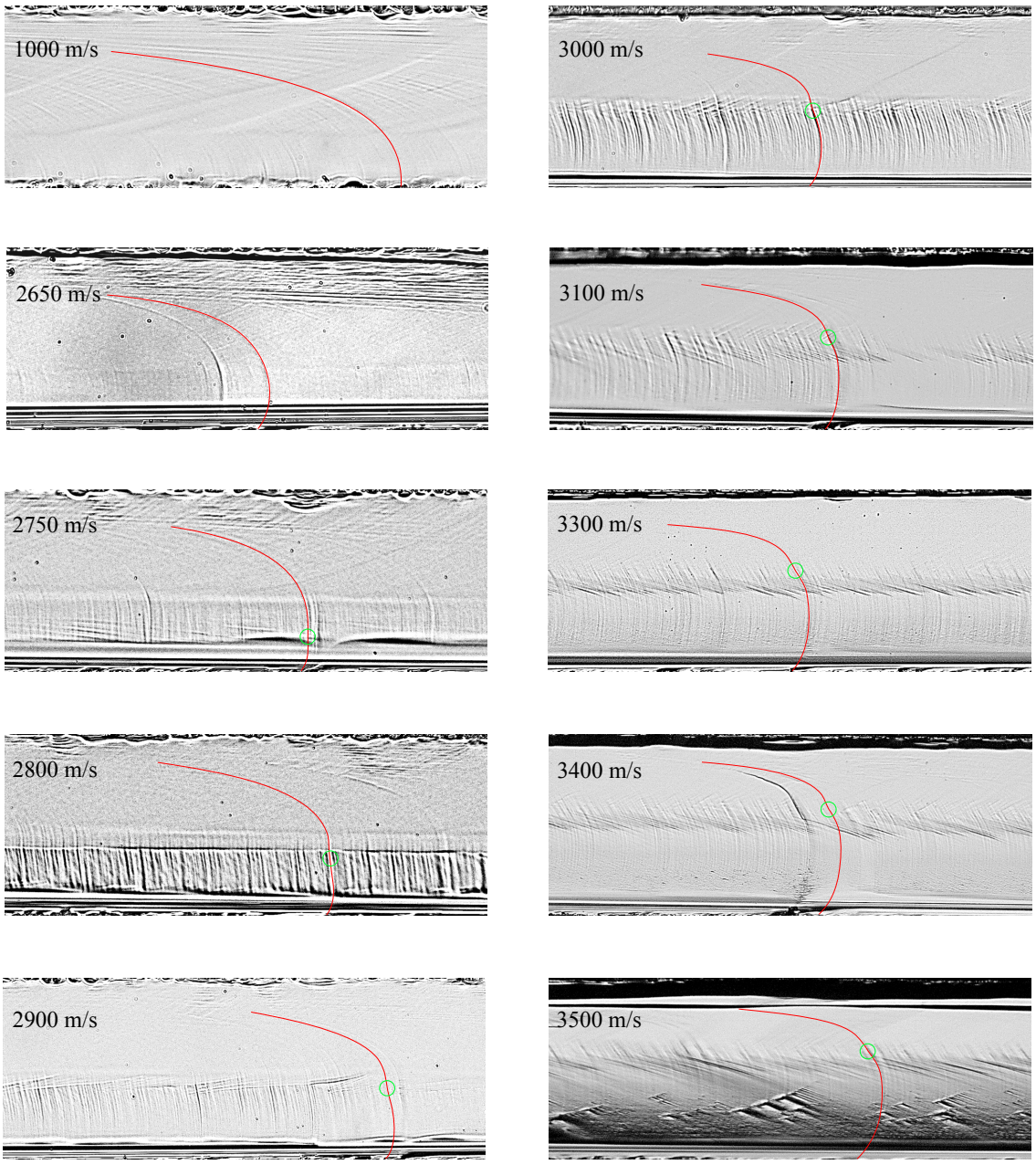

FIGURE 3.4: Fracture surface morphology of the (110) cleavage plane under three-line bending tests with the crack velocity of 1000 m/s, 2650 m/s, 2750 m/s, 2800 m/s, 2900 m/s, 3000 m/s, 3100 m/s, 3300 m/s, 3400 m/s and 3500 m/s. The Wallner lines shape is highlighted by the red curve and the local curvature kink is highlighted by the green circle for the crack velocity higher than 2700 m/s.

is considered for the front-waves interaction in this section, thus $C = C_R$. However, due to the anisotropy of silicon, the Rayleigh waves speed along different crystallographic directions is not constant [PRA 69]. Here, we provide a mathematical method to determinate

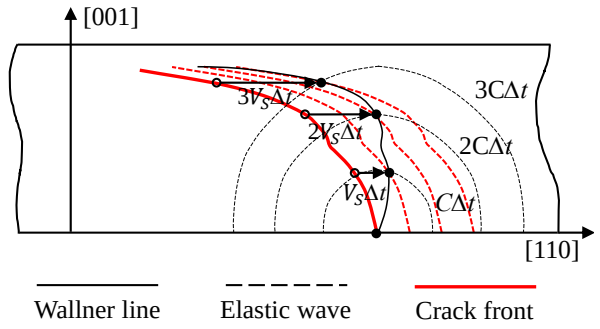

(a)

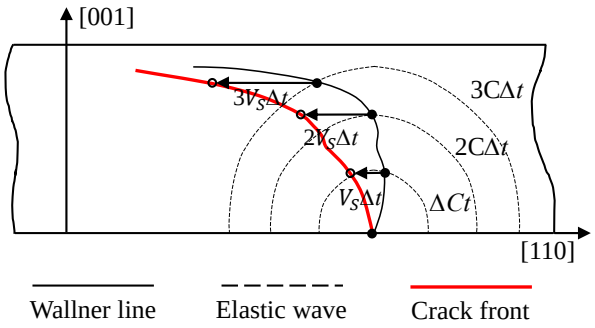

(b)

FIGURE 3.5: Schematic draw of the kinetics of the Wallner lines generation from surface defect : (a), and the crack front shape recovering : (b). V_s and C are the crack propagation velocity and the elastic waves speed, respectively.

the crack front shape based on the retroactive kinetics of an arbitrary segment of Wallner lines.

The scheme of the crack front reconstruction is illustrated in Fig. 3.6(a), where x and y are the crack propagation direction [1-10] and the specimen thickness direction [001], respectively.

We assume that a Wallner line is generated from the point $O(x_0, y_0)$ and extends towards the upper side of the specimen. Fig. 3.6(a) illustrates the Wallner line growth between point A and point B from time t_1 to $t_1+\Delta t$. At the intersection point $A(x_1, y_1)$, the propagation direction of the Rayleigh wave $\overrightarrow{OA}$ forms an angle γ with the x direction and the Wallner line forms a tangent angle β. When the time step Δt is small enough, the extending velocity of the Wallner line, V_{WL}, at the point A can be calculated in the triangle OAB :

$$\lim_{\Delta t \to 0} \frac{OA + C_R \Delta t}{sin(\beta - \gamma)} = \frac{OA}{sin(\angle OBA)} = \lim_{\Delta t \to 0} \frac{V_{WL} \Delta t}{sin((\beta - \gamma) - \angle OBA)} \tag{3.1}$$

hence,

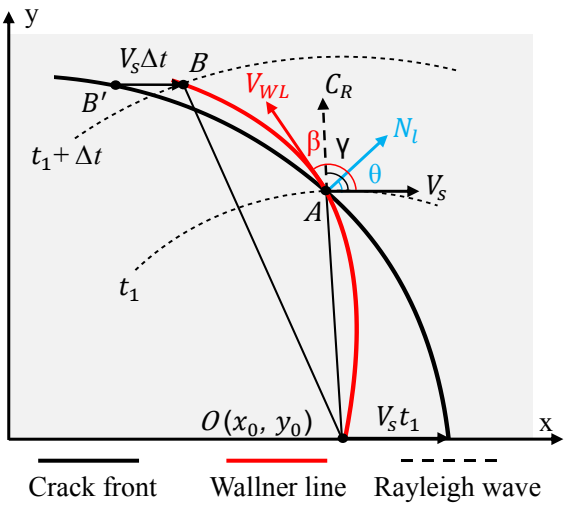

(a)

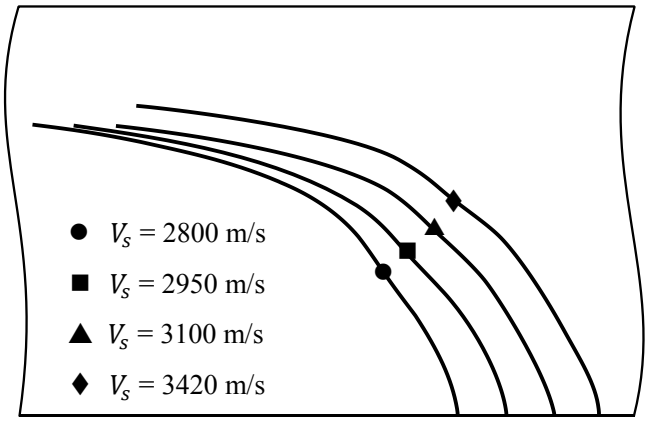

(b)

FIGURE 3.6: Crack front shape determination : (a) schematic drawing for determining the local normal direction along the crack front, and (b) crack front shapes for different crack steady-state velocities. The curvature jump spot on the crack front is highlighted with different marks.

$$V_{WL} = \lim_{\Delta t \to 0} \frac{\sqrt{(OA + C_R\Delta t)^2 - OA^2 sin(\beta-\gamma)^2} - OAcos(\beta-\gamma)}{\Delta t} \tag{3.2}$$

where,

$$OA = \sqrt{(x_1 - x_0)^2 + (y_1 - y_0)^2} \tag{3.3}$$

After the time step Δt, the point B' on the crack front interacts with the Rayleigh wave at B. The local crack direction, which is assumed to be the normal of the local crack front (noted N_l) at the point A, forms an angle θ with the x direction. In the triangle ABB' :

$$\frac{V_{WL}\Delta t}{sin(\theta+\frac{\pi}{2})} = \frac{V_S\Delta t}{sin(\theta+\frac{\pi}{2}-\beta)} \tag{3.4}$$

thus, the angle θ can be calculated as :

$$\theta = asin\frac{V_{WL}sin(\beta)}{\sqrt{V_{WL}^2 - 2V_{WL}V_s cos(\beta)+V_s^2}} - \frac{\pi}{2} \tag{3.5}$$

Hence, the normal direction along the crack front and the crack front shape can be obtained, using the Wallner line's shape, the Rayleigh wave speed C_R as a function of the crystallographic direction γ [PRA 69] and the crack steady-state velocity V_s. Fig. 3.6(b) presents the crack front shapes at the steady-state for V_s of 2800 m/s, 2950 m/s, 3100 m/s and 3420 m/s. Same as the Wallner lines, the front shape varies with the steady-state velocity and contains a curvature kink. The curvature jump spot is located higher along the thickness of the specimen when the crack propagation velocity increases. This curvature jump is also reflected in the Wallner lines when V_s is higher than 2700 m/s.

Zhao and co-authors suggested that this phenomenon is induced by the sudden increase in the dynamic toughness of the (110) plane at 2700 m/s [ZHA 18a]. Indeed, when the crack front propagates at low velocity ($<$ 2700 m/s), the dynamic fracture toughness along the (110) plane is nearly constant that $\Gamma_D = 2\gamma$ = 3.46 m/s [PÉR 00c, CRA 00, ATR 11a]. The local crack velocity, which is normal to the crack front, monotonically decreases from the bottom to the top of the crack front from V_s to approximately 0. According to the LEFM (Eq. 3.10), the strain energy release rate decreases from bottom to the top along the crack front with a uniform distribution accommodating the local crack velocity variation, so that the crack front shape evolves with the variation of the crack front propagating velocity to adapt the necessary energy flux. Meanwhile, when the crack front propagates at high velocity ($>$ 2700 m/s), if the dynamic fracture toughness at a local position of the crack front suddenly jumps, the local crack velocity will slow down. As a result, the gradient in local crack velocity produces a kink on the crack front. The detailed analysis will be further presented in Section. 3.

3 Crack plane deflection and shear wave effects in the dynamic fracture of silicon single crystal

Note that the (110) cleavage plane is the most preferential fracture path, why the crack propagates along the (111) plane ? In this section, we present the crack path deflection from the (110) cleavage plane to the (111) cleavage plane in three-line bending tests. Based on the fractographic analysis, we show how the dynamic crack behaves in response to

the local stress perturbations inducing the deflection of the crack path. A general discussion on the dynamic fracture energy, and the source of the stress perturbations related to the punch line-contact in the light of control experiments of the crack propagation under and beside line-contact will be carried out in the next section.

3.1 Crack velocity versus cleavage plane

All the cleavage planes were examined through fractographic analysis, and selected fracture surface morphologies are presented in Fig. 3.7. When the crack propagates on the (110) plane, primary fracture surface marks, *i.e.* the Wallner lines [WAL 39] can be identified. These lines evolve with respect to the crack steady-state velocity V_s, as can be seen in Figs. 3.7(a)-(c). When the crack velocity is high ($>$ 2700 m/s), front waves traces are observed in the steady-state (110) cleavage plane [ZHA 18a], as highlighted by the purple lines in Figs. 3.7(b) and (c). Moreover, when the (111) plane dominates the fracture, (111) surface instabilities arise [SHE 08], as underlined by the blue line in Fig. 3.7(d).

Owing to the (110) pre-crack, the cracks initiate on the (110) plane for all the tests. However, four different crack propagation scenarios have been identified. The first case, where the crack propagates stably on the (110) plane, is named full (110) cleavage plane and denoted by blue marks in Fig. 3.8. The second case, where the crack deviates to the (111) plane only at the upper portion of the fracture surface and quickly returns back to the (110) plane, is named partial crack deflection and denoted by purple marks in Fig. 3.8. The third case, where the (110)-(111) plane deflection covers the whole fracture thickness, followed by a recovery onto the initial (110) plane, is called complete crack deflection and represented with red marks in Fig. 3.8. The fourth scenario, where the deflection is maintained until the end of the fracture process, is called full (111) cleavage plane and represented by green marks in Fig. 3.8.

The tests carried out with pre-cracks under and beside the contact line are shown in Fig. 3.8 with square and circle marks, respectively. It is found that when the crack propagates under the contact line, the cleavage plane deflection occurs at about 1600 m/s (40 MPa). Then as the crack velocity increases, the (110) cleavage perturbation develops from the partial crack deflection to the complete crack deflection at 3300 m/s (90 MPa) and finally to the full (111) cleavage scenario at 3600 m/s (150 MPa). However, when the crack propagates 2 mm away from the contact line, one can notice that the fracture deflection takes place at a higher crack velocity for each scenario compared to the first loading configuration. In general, the complete crack deflection always occurs beyond 3400 m/s in the present three-line bending tests, even if the direct contact effect is discarded, as for the second loading configuration. This fracture behavior is different from that observed during four-line bending tests in which the crack stably propagates on the (110) plane up to 3700 m/s [ZHA 17].

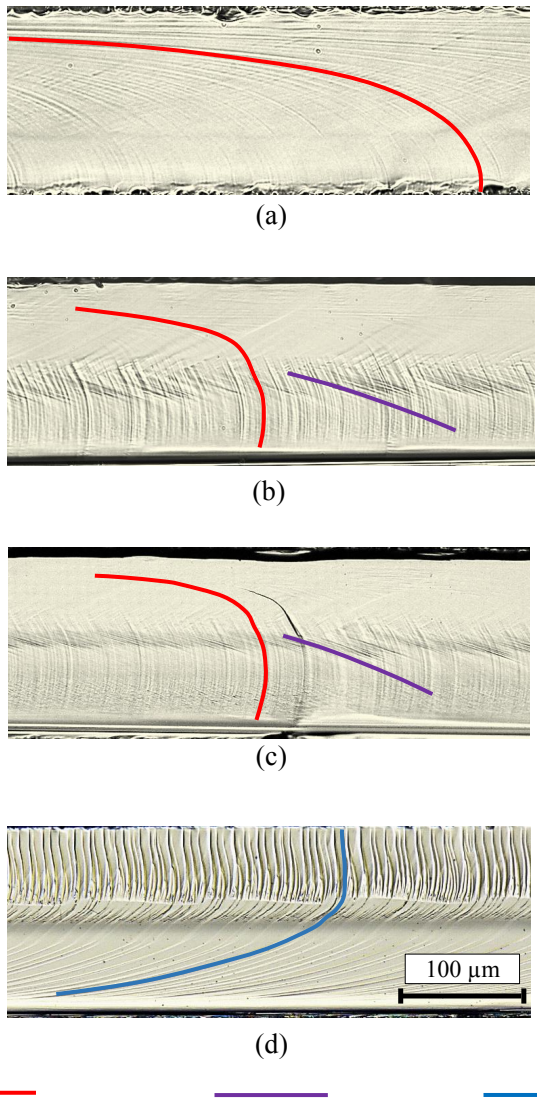

FIGURE 3.7: Fracture surface morphology of (a) (110) cleavage plane under the contact line with the crack velocity of 610 m/s, (b) (110) cleavage plane under the contact line with the crack velocity of 3000 m/s, (c) (110) cleavage plane *beside* the contact line with the crack velocity of 3300 m/s, (d) (111) cleavage plane under the contact line with the crack velocity of 3600 m/s.

3.2 Cleavage plane deflection

As presented in Fig. 3.8, the crack plane deflection phenomenon involves a strong dependence on the crack velocity as well as the cracking position relative to the contact line. The partial and complete deflection behaviors will be described in detail in this section.

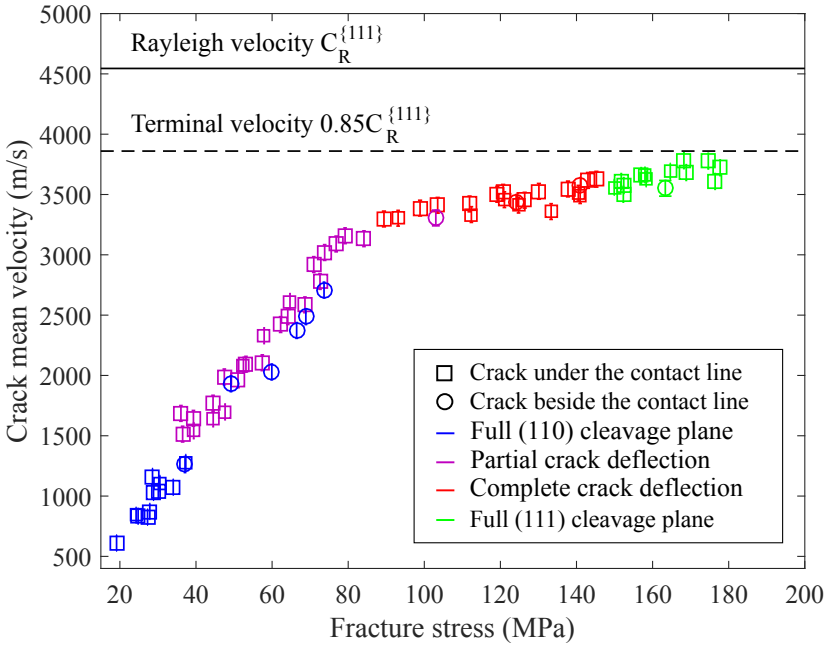

FIGURE 3.8: Correlation of fracture stress with crack steady-state velocity and the cleavage plane. The two loading configurations are labeled with different symbols and the fracture planes are labeled with different colors. The terminal and Rayleigh velocities are also reported.

3.2.1 Partial crack deflection

Fig. 3.9 presents the reconstruction of the fracture surface for a partial crack deflection case under the contact line with σ_f = 79.18 MPa and V_s = 3100 m/s. The first 20 mm of the fracture surface is shown at the center of the figure, surrounded by close-ups of high magnification for 6 different locations along this crack surface (Figs. 3.9a - f). The crack surface at the center was observed from the [110] direction so that the bright zone represents the (110) cleavage plane due to the full light reflection and the dark zone presents the (111) cleavage plane. As shown in Fig. 3.9a, the first partial crack deflection occurs at the crack initiation position. The crack nucleates on the (110) plane from the bottom surface of the specimen. Very smooth fracture surface can be noticed close to the initiation spot. When extending to the upper surface, the crack deflects onto a (111) plane at a height of approximately $0.5h$, where h denotes the specimen thickness. The crack front is therefore non-planar to accommodate the misorientation between the (110) and the (111) planes, at an angle of 35.26°. However, as shown in Fig. 3.9b, the crack comes back to full (110) plane after a propagation distance of 3.05 mm. Two other partial deflections (see Figs. 3.9c and 3.9e) arise at about 6.83 mm and 15.04 mm, involving an extension length of 2.9 mm and height of $0.4h$ prior to full (110) cleavage recovery (see Figs. 3.9d and 3.9f). The fracture process beyond 20 mm is not shown here but consists of the (110)-(111) deflection and recovery zone decreasing until vanishing. This feature

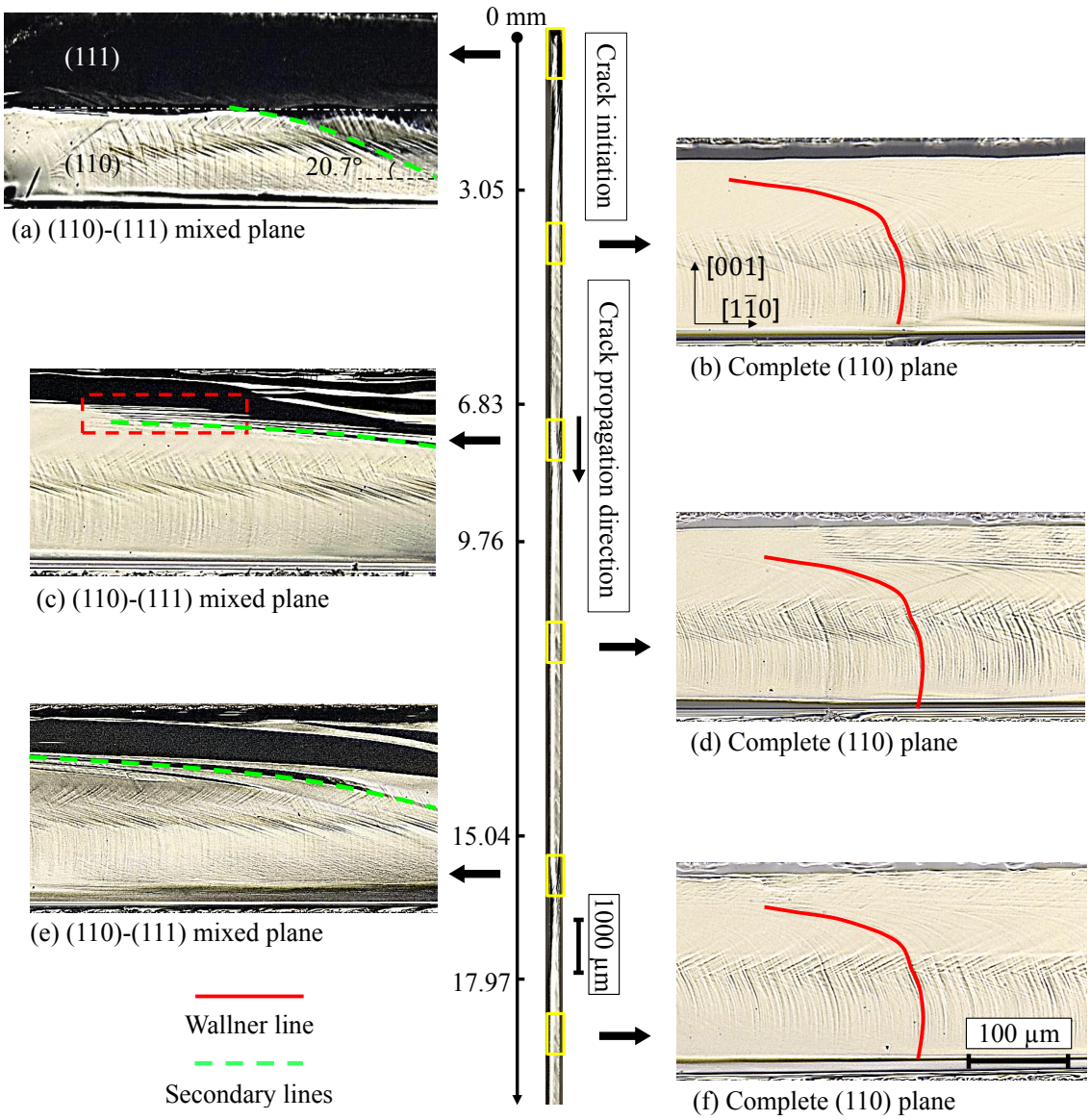

FIGURE 3.9: Fractography of a test with the crack velocity of 3100 m/s. The first 20 mm of the fracture surface is shown in the center. Six close-ups with partial crack deflections and recoveries are shown from (a) to (f) and their locations are highlighted by yellow rectangles. The crack propagation direction is from up to down in the central figure and from left to right in the close-ups.

suggests that the partial deflection is an occasional and transient phenomenon.

Focusing on the deflection surface, some secondary lines (SL) can be observed between the (110) and the (111) cleavage planes, highlighted by the green dotted lines in Fig. 3.9. In Fig. 3.9c, at the beginning of the deflection section, the red dotted rectangle indicates the so called crack flip-flops reported in [SHE 05]. These unstable short-range

crack undulations are considered as the onsets of SL. As the SL extend, the perturbation of the (110) plane takes place and the deflection tends to expand toward the lower side of the crack surface (see Figs. 3.9a and e). Albeit the (110) plane is perturbed, the fracture surface encompasses only a part of (111) plane in the upper side. Besides, the Wallner lines keep very similar shapes after the partial crack deflection, as it can be seen in Figs. 3.9b, d and f. This indicates that the crack deflection has little effect on the crack steady-state velocity.

Another reconstruction for a partial crack deflection of the fracture surface for the test with pre-crack under the contact line with σ_f = 84.15 MPa and V_s = 3160 m/s is presented in Fig. 3.10. The crack propagates stably along the (110) cleavage plane (see Figs. 3.10(a) and (c)), while the occurrence of secondary lines breaks this stabilization. The crack tends to deflect from the (110) plane to the (111) plane from the upper side of the fracture surface as can be seen in Fig. 3.10(b). The perturbation length of the fracture surface of about 3.7 mm. The crack then recovers and propagates on the (110) cleavage plane when the perturbation of SL disappears.

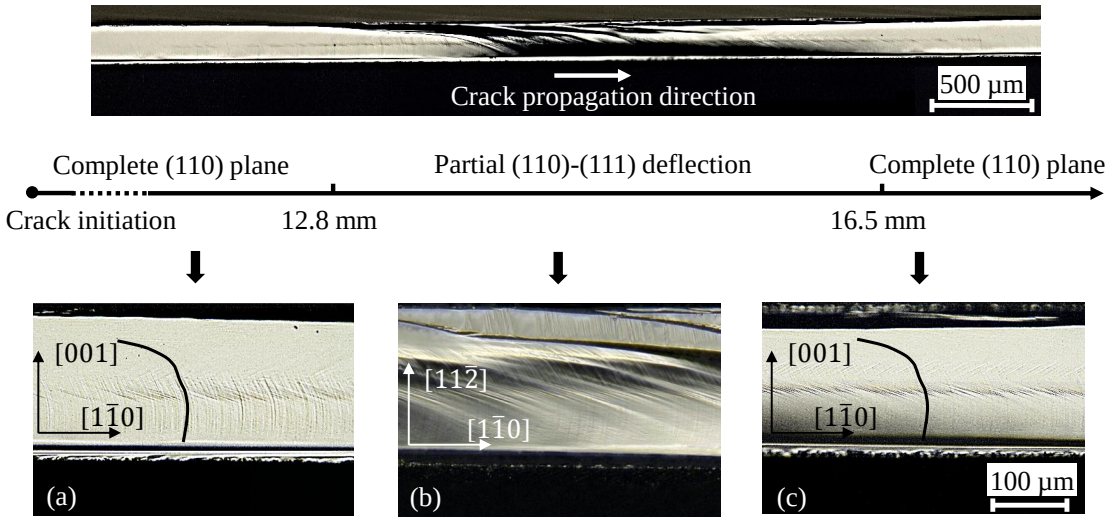

FIGURE 3.10: Fractography of a partial crack deflection with crack velocity of 3160 m/s. (a) Stable crack propagation along the (110) cleavage plane, (b) partial (110)-(111) crack deflection in the presence of SL, and (c) re-stabilization of the crack propagating along (110) cleavage plane.

3.2.2 Complete crack deflection

When the crack is driven by higher fracture stress, the (110)-(111) deflection is more extensive. Figs. 3.11 display a complete crack deflection during the fracture process under the contact line with σ_f = 103.5 MPa and V_s = 3420 m/s. As highlighted in Fig. 3.11(a), the deflection at the fracture initiation is similar to the case of partial crack deflection where the crack initiates from the (110) plane and deflects to the (111) plane when extends to the upper side as shown in Fig. 3.9. Yet, what differs from the partial deflection scenario

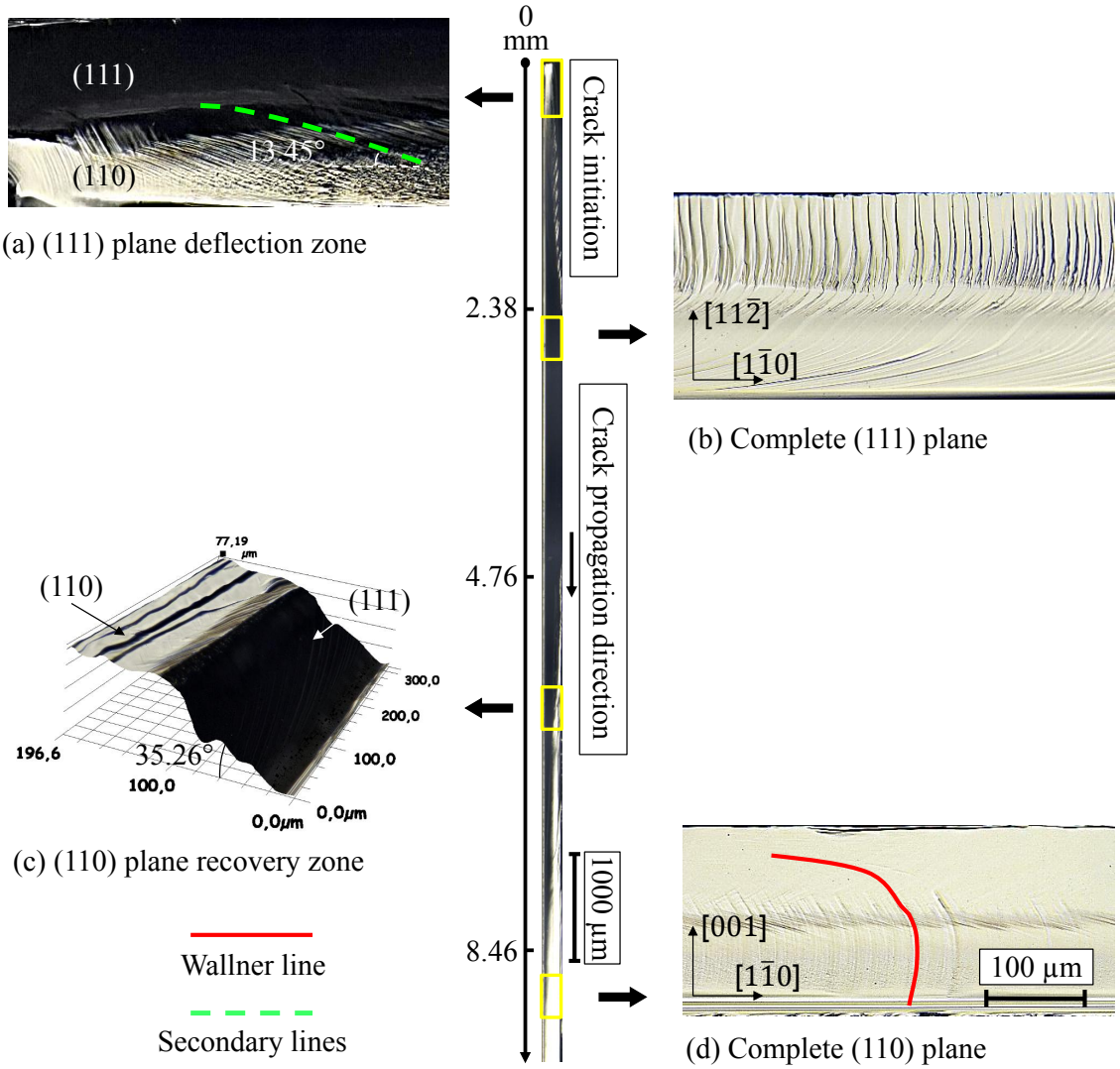

(a) (111) plane deflection zone

(b) Complete (111) plane

(c) (110) plane recovery zone

(d) Complete (110) plane

FIGURE 3.11: Fractography of a test with crack velocity of 3420 m/s. The first 9.5 mm of the fracture surface is presented in the center and four close-ups of complete crack deflections and recoveries are shown from (a) to (d) as well as their locations highlighted by the yellow rectangle.

is that, after a (110)-(111) co-existent phase, the (111) cleavage plane develops over the entire thickness of the specimen and dominates the fracture process. As it can be seen in Fig. 3.11(b), the (111) surface instabilities with a constant height confirm the crack steady-state velocity along the (111) plane [SHE 08], as mentioned in Section. 2.1.2.

However, the (111) cleavage is not permanent. At the propagation length of 4.76 mm, the crack begins to switch back to the (110) plane from the upper side of the crack surface. The full (110) recovery is obtained at 8.46 mm after a (111)-(110) transition zone, as highlighted by Fig. 3.11(c). The crack then propagates on the (110) plane (see Fig. 3.11(d)) with occasional partial crack deflections till the end of the fracture path. Besides, the Wall-

ner line shape shown in Fig. 3.11(d) confirms the steady-state crack velocity. Note that in the crack deflection region (see Fig. 3.11(a)), similar SL are observed. The SL only appear in the deflection region, suggesting a correlation with the crack deflection.

3.3 Fracture behavior in deflection zone

3.3.1 Deflection surface morphology

In the crack deflection regions, complex surface morphologies are observed. This is presented by the fractographies containing half topographic feature for three cracks propagating under the contact line at V_s of 2800 m/s, 2950 m/s and 3620 m/s, respectively (Figs. 3.12(a), (b) and (c)). The fracture surface encompasses a dark zone and a bright zone, corresponding to the (111) plane and the (110) plane, respectively. The SL highlighted by green lines nucleate at the upper side of the crack surface. At the early stage of the crack deflection, the crack deflects along the SL (highlighted by the green continuous lines). The fracture surface profiles at this stage are measured along the [001] direction by laser scanning profilometry and are shown in Fig. 3.13. The schematic drawing of the cleavage planes and SL is given on the right side in Fig. 3.13. The surface undulations on the (110) plane correspond to the fracture surface markings, while the large undulation between the (110) and the (111) plane represents the SL. It can be observed that the crack plane switches from the (110) plane to the (111) plane once encountering the SL which act as the boundaries between the (110) and the (111) plane. In the case of partial crack deflection as shown in Figs. 3.12(a) and b, with the SL expanding into the lower part of the fracture surface (highlighted by green dotted lines), the crack plane stays on the (110) plane instead of jumping to the (111) plane. Nevertheless, the lower part is not sitting on a planar (110) plane, as it is still perturbed and deviated from the perfect (110) plane. This perturbation is progressive and manifests in line with the SL (highlighted by black arrows). Conversely, for the case of complete crack deflection shown in Fig. 3.12(c), the crack plane sharply deflects from the (110) plane to the (111) plane through the whole wafer's thickness, and the deflection is perfectly in line with the SL. These observations imply that the crack deflection behavior is related to the SL.

3.3.2 Secondary Wallner lines

What are the SL? Similar to the Wallner lines, the shape of SL depends on the crack velocity, as reflected by the different tilt angles for the crack cases presented in Figs. 3.9a, 3.11a and 3.12. Generally, fracture surface marks are produced by the interactions between the moving crack front and the elastic waves, and the amplitude of the marks corresponds to a decay with respect to the nature of the elastic waves, for instance a linear decay for the Wallner lines generated by surface waves [WAL 39, BON 03, SHA 04] and an exponential decay for the front wave traces generated by solitary waves [MOR 98, SHA 01, SHA 04]. Therefore, the decay behavior is crucial to identify the nature of the SL.

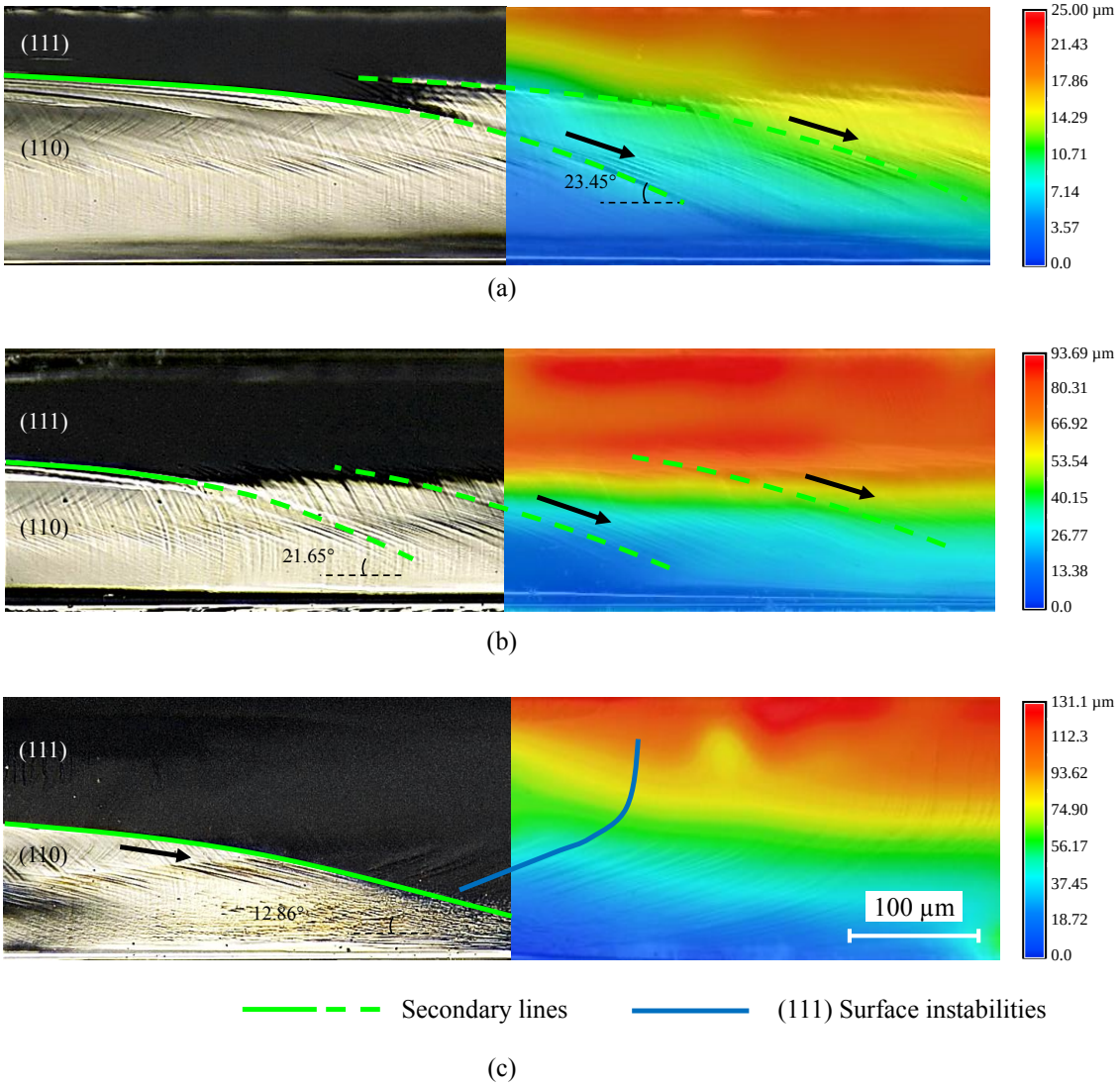

FIGURE 3.12: Fractographies and topographies of the (110)-(111) deflection zones : (a) partial crack deflection with V_s = 2800 m/s, (b) partial crack deflection with V_s = 2950 m/s, and (c) complete crack deflection with V_s = 3620 m/s).

Figure 3.14(a) shows the reconstructed topography of SL for V_s = 3100 m/s before interacting with the FW traces, measured with the laser scanning profilometer. The undulation amplitude during the decay stage of four SL (noted as A_{SL}), measured from peak to trough, is shown in Fig. 3.14(b), as a function of the distance from the generation spot of SL (noted as r). The A_{SL} is found continuously decay, following a linear decay on logarithmic scale with a rate of $1/r^2$. This behavior fulfills the characteristic of Wallner lines [SHA 04, BON 05], which suggests that the SL can be referred to as Wallner lines.

The SL should be generated when the crack front interacts with the expanding surface waves. In order to establish the relationship between the SL and the crack front, the crack

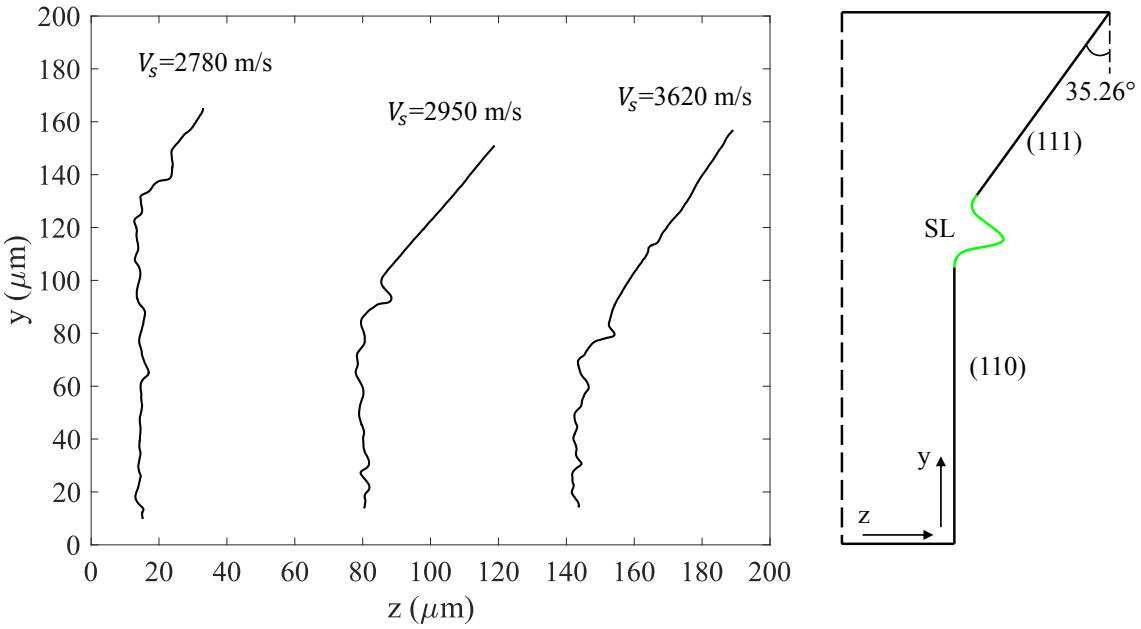

FIGURE 3.13: Fracture surface profiles along the [001] direction at the early stage of the crack deflection for V_s = 2800 m/s, 2950 m/s and 3620 m/s. Profiles have been shifted horizontally for the sake of clarity. The schematic drawing of cleavage planes versus the SL position is shown on the right, where y and z are along the [001] and [110] directions, respectively.

front shape is reconstructed via the retroactive kinetics of the Wallner lines and the elastic waves, so that the speed of surface waves can be calculated.

As shown in Fig. 3.15(a), we suppose that the SL are generated at point O by means of surface waves propagating at V_{SW} to the lower side of the specimen, and interacting with the crack front at a velocity of V_{SL}. The direction of V_{SW} and V_{SL} forms an angle φ and α with the x direction, respectively. With the local crack normal direction, N_l defined in Fig. 3.6a and Eq. (3.5), V_{SL} can be expressed as :

$$V_{SL} = \frac{V_s sin(\theta + \frac{\pi}{2})}{sin(\alpha + \theta + \frac{\pi}{2})} \tag{3.6}$$

With the same principle as Eqs.(3.1) and (3.2), V_{SW} can be calculated by :

$$V_{SW} = \lim_{\Delta t \to 0} \frac{\sqrt{(V_{SL}\Delta t)^2 + 2V_{SL}\Delta t * OA * cos(\alpha - \varphi) + OA^2} - OA}{\Delta t} \tag{3.7}$$

Figure 3.15(b) shows the V_{SW} in the case of V_s = 2800 m/s, 2950 m/s, 3100 m/s and 3420 m/s, with α varying from 7.5° to 20°. The errorbar corresponds to the crack propagation velocity uncertainties. It can be noticed that the surface waves expand at around the Rayleigh wave velocity. Moreover, due to the small curvature variation of SL, it is found that the V_{SL} is similar to the V_{SW}. Since both V_{SL} and the front wave speed are close to the

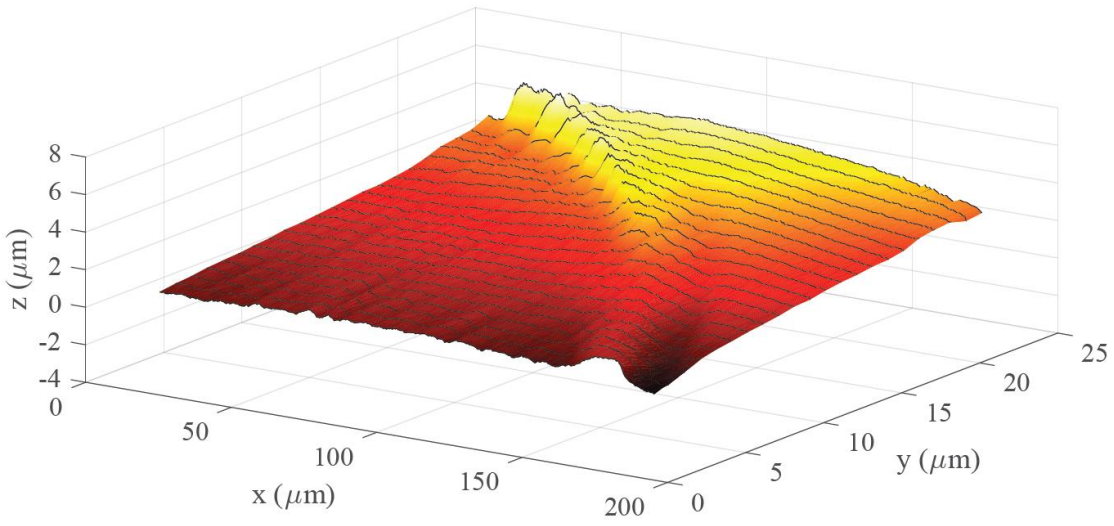

(a)

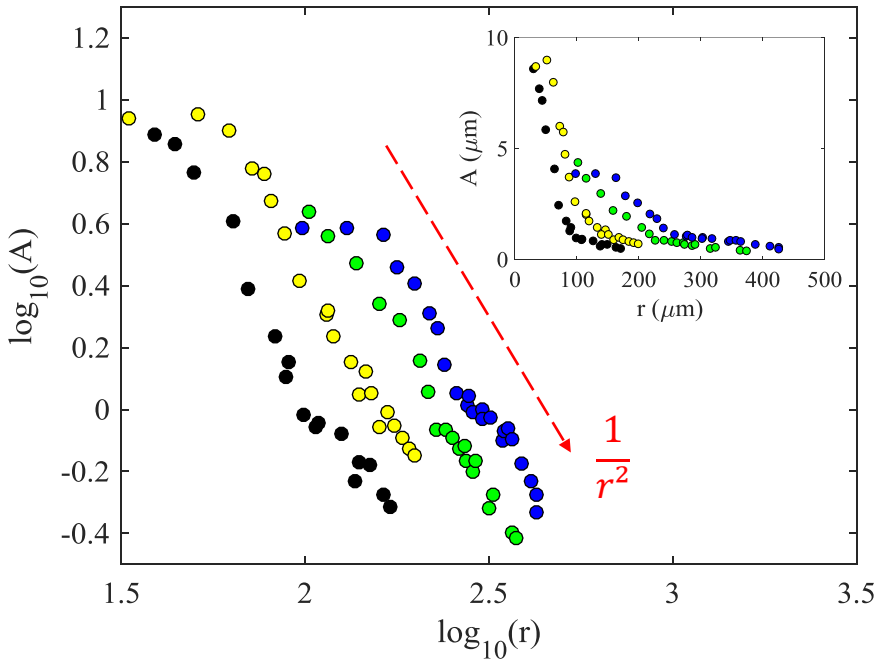

(b)

FIGURE 3.14: SL decay measurement : (a) topography of a SL at V_s = 3100 m/s, and (b) decay of the undulation amplitude A_{SL} of secondary lines (measured from peak to trough) as a function of the extending distance r on the logarithmic scale with inset graph on linear scale and the red dotted arrow represents the $1/r^2$ decay.

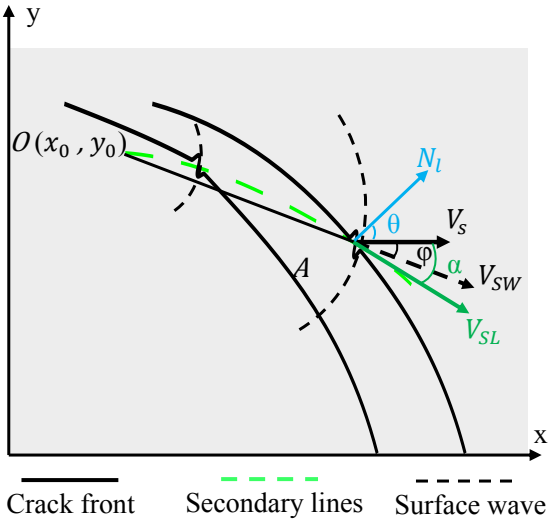

(a)

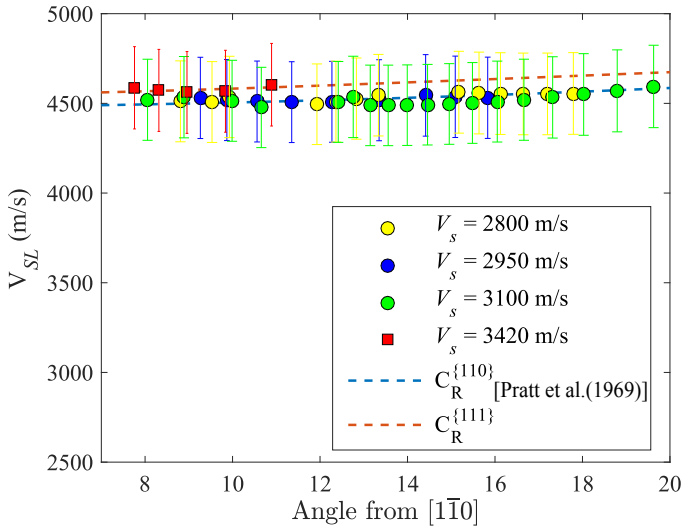

(b)

FIGURE 3.15: Schematic drawing for determining the surface wave velocity generating the secondary lines (a), evaluated wave expanding velocities for four different cracks (b).

Rayleigh wave speed [MOR 00, SHA 01], the SL are superimposed with the front wave traces at the lower part of the crack surface, as it can be observed in Fig 3.12.

From the analysis above, it is found that the undulation amplitude of SL, A_{SL} decays with the $1/r^2$ rate (see Fig. 3.14) and the original elastic waves generating the SL propagate at the Rayleigh wave speed (see Fig. 3.15(b)). Hence, we can refer to the SL as secondary Wallner lines (SWL), to differ from the primary Wallner lines generated from

the specimen surface flaws (see Fig. 3.7). The unstable short-range crack undulations (see Fig. 3.9(c)) are the signature of the SWL initiation involved in the crack deflections. Moreover, as the plane deflection locally breaks down the pure mode I fracture configuration by introducing a mode III due to the shear stress component, we conclude that the SWL are engendered by anti-planar shear waves propagating from the upper to the lower side of the fracture surface. The anti-planar shear waves likely result from the contact between the specimen and the punch roller, as it will be discussed later in section 4.3.

3.3.3 Local crack velocity

During the (110)-(111) crack deflection, the non-planar fracture plane implies that the crack front is twisted when the crack deflects from the lower (110) plane to the upper (111) plane. Figs. 3.16(a) and (b) present the steady-state (110) cleavage zone and the very beginning of the (110)-(111) deflection zone for the crack propagating at V_s = 2950 m/s (also presented in Fig. 3.12(b)). It can be seen in Fig. 3.16(b) that the crack front twist influences the Wallner line shape with a kink across the (110)-(111) deflection zone, illustrated by the point #1.

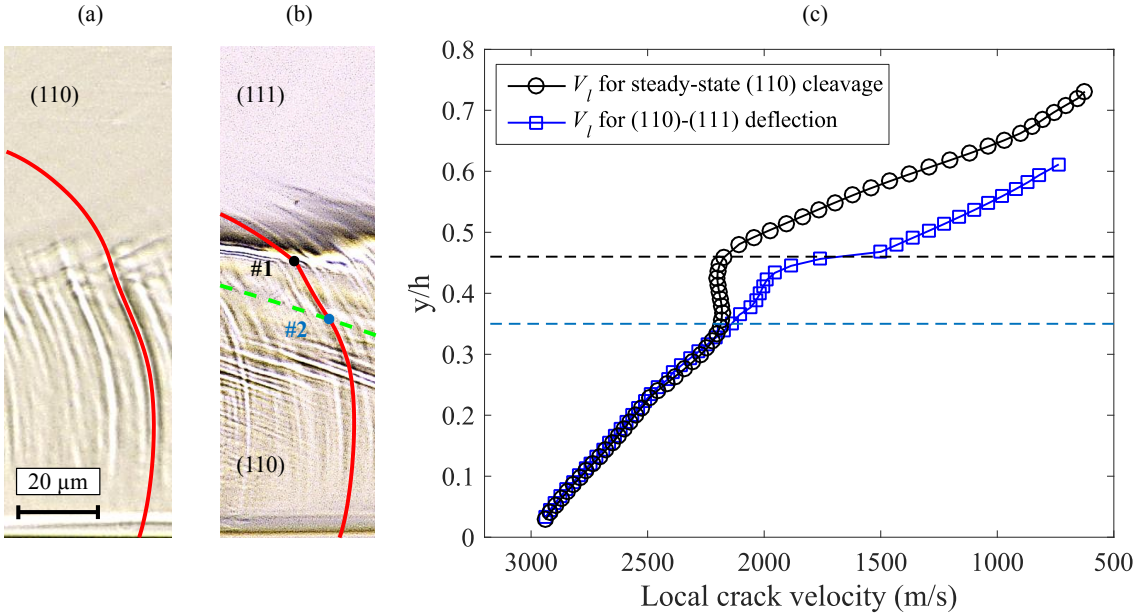

FIGURE 3.16: Local crack velocity calculation for the crack of 2950 m/s : (a) Wallner lines in the steady-state (110) zone, (b) Wallner lines in the (110)-(111) deflection zone, where the red and green lines highlight the primary and secondary Wallner lines, respectively, and (c) local crack velocities in the two different zones.

The crack local velocity V_l, normal to the crack front, is calculated by :

$$V_l = V_s cos(\theta) \tag{3.8}$$

As shown in Fig. 3.16(c), V_l on the steady-state (110) plane and the (110)-(111) deflection zone are determined using the Wallner lines (highlighted in Figs. 3.16(a) and (b)) unfolded on the same plane. The horizontal blue dotted line (Fig. 3.16(c)) at $0.35h$ presents the height of the point #2 in Fig. 3.16(b), which corresponds to the cross-point between the primary Wallner line and the first SWL observed along the fracture surface. Thus, the portion of the crack front higher than the point #2 is affected by the anti-planar shear waves while the lower portion is not affected. The black horizontal dotted line (Fig. 3.16(c)) at $0.46h$ presents the height of the point #1 in Fig. 3.16(b), which corresponds to the onset point of the (110)-(111) deflection. Under bending load, the local crack velocity, V_l decreases from the lower part to the upper part of the specimen thickness. However, V_l in the case of (110) cleavage, highlighted by the black marks in Fig. 3.16(c), locally increases and decreases again at the curvature jump of the crack front. This in-plane local velocity oscillation was considered as the source of front waves in [ZHA 18a]. In particular, V_l in the (110)-(111) deflection zone, highlighted by the blue marks in Fig. 3.16(c), decreases faster than that in the steady-state (110) cleavage. This is likely related to the interaction between the crack front and the shear waves in the deflection zone. Indeed, the crack front is locally deviated by the shear waves and deflects away from the (110) plane, hence the increase of effective dynamic fracture toughness during the (110)-(111) transition induces a decrease of V_l compared with the steady-state (110) cleavage case. Furthermore, when the crack surface deflects on the (111) plane, the crack front twists at point #1 with a variation of θ. Consequently, V_l drops from 1760 m/s to 1500 m/s across the onset of the crack plane deflection. Since the dynamic fracture energy relates to the crack velocity [CRA 00], the local crack velocity drop enables assessing the dependency of the cleavage plane toughness to the crack velocity. This will be addressed in section 4.1.

3.4 Cleavage plane recovery

The (111)-(110) recovery phenomenon described in section 3.2 implies that the (110) plane is a more favorable fracture path than the (111) plane, in the present loading configuration. As indicated in Fig. 3.9, Fig. 3.10 and Fig. 3.11, the deflection takes place first in the upper portion of the fracture surface, where the local crack velocity is very low, and then extends to the lower portion of the fracture surface, where the local crack velocity is much higher, until the (110) dominates the whole crack path.

Why does the (111)-(110) recovery initiate from the low speed portion ? Indeed, when the crack switches from the (111) plane to the (110) plane under bending, there are two possibilities illustrated in Fig. 3.17. One is that the deflection initiates from the lowest point, where the local velocity coincides with the global velocity and is the largest, see Fig. 3.17(a). The other is from the highest point, where the local velocity is almost zero, see Fig. 3.17(b). Assuming that the recovery is instantaneous, for the first possibility, the crack needs to rotate twice 90°, while a single rotation of 35.6° is involved for the second one. This clearly shows that the recovery takes place easier from the upper side to avoid large angle mismatch during the recovery.

Furthermore, the recovery is not instantaneous even though initiating from the low

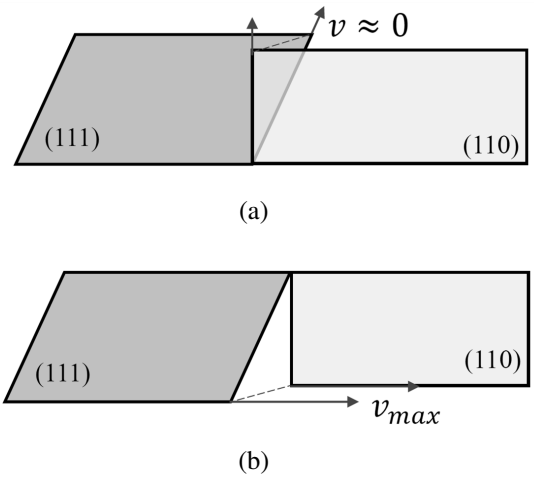

FIGURE 3.17: (111)-(110) recovery : schema of the assumption of instantaneous recovery from (a) the bottom of the fracture surface, and (b) the top of the fracture surface.

speed portion. It covers a transition length in the complete crack deflection much longer than that in the partial crack defection (see Fig. 3.10 and Fig. 3.11). Based on the tests carried out in this work, the full (111) cleavage length following the deflection and the (111)-(110) recovery length are plotted versus the crack steady-state velocity, as presented in Fig. 3.18. Only the cracks under the contact line are considered. Indeed, the higher the crack velocity, the larger the full (111) cleavage and the (111)-(110) transition regions. This correlation suggests that high crack velocity is not prone to the crack recovery, even when the recovery is in favor of the most energetically favorable fracture plane, *i.e.* the (110) plane here. The fact that the high velocity impedes the crack plane change is likely a signature of the crack front inertia generated from the crack tip-shear waves interaction at the crack deflection zone, as proposed by [GOL 10b]. It has been shown in Fig. 3.8 that the (110) recovery was not observed when the crack velocity is higher than 3650 m/s. However, this result is obtained with a specimen length of 50 mm, and the emergence of the (110) recovery is expected with larger specimen size.

3.5 Transient crack velocity determined with secondary Wallner lines

According to the relationship between the Wallner lines and the crack front, as shown in Fig. 3.6(a) and 3.15(a), we propose here a small scale method to measure the global crack velocity in the transient phase $V_{transient}$, *i.e.* the phase between the crack initiation and the steady-state. With Eqs. (3.4) and (3.6), $V_{transient}$ can be determined as :

$$V_{transient} = \frac{V_{SL}V_{WL}sin(\alpha+\beta)}{V_{SL}sin(\alpha)+V_{WL}sin(\beta)} \tag{3.9}$$

where V_{SL} is obtained from Eq. (3.7) by replacing V_{SW} with C_R. Based on this method,

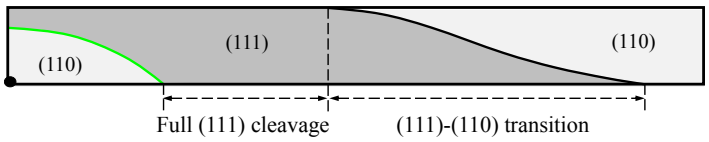

(a)

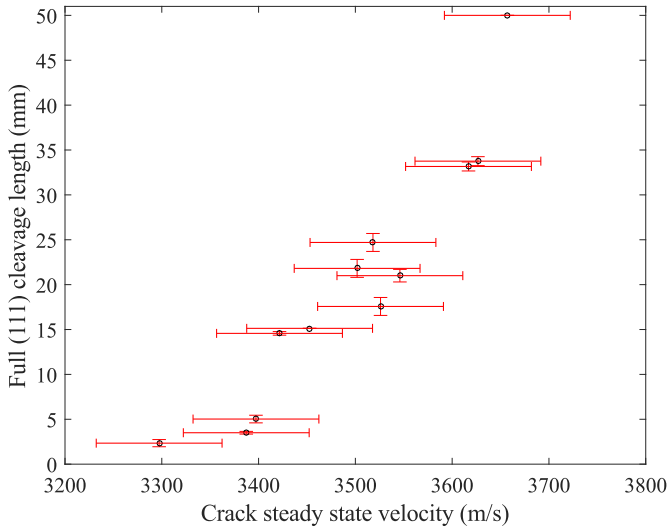

(b)

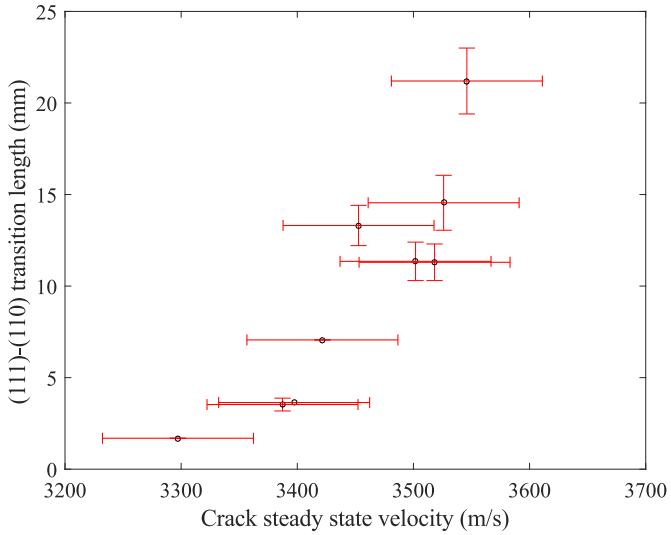

(c)

FIGURE 3.18: Correlation between the (111) plane involved region and the crack steady-state velocity : (a) schematic drawing of complete crack deflection scenario, (b) full (111) length versus crack velocity, and (c) (111)-(110) transition length versus crack velocity.

the acceleration phase of the crack for V_s = 3420 m/s is analyzed. Fig. 3.19(b) displays $V_{transient}$ as a function of the crack propagation length till the steady-state. It can be noticed that the crack acceleration phase is very short. The crack front velocity already exceeds 2686 m/s at the crack length of 105 µm and reaches the crack steady-state velocity at a crack length around 450 µm, which shows a good agreement with [ZHA 17].

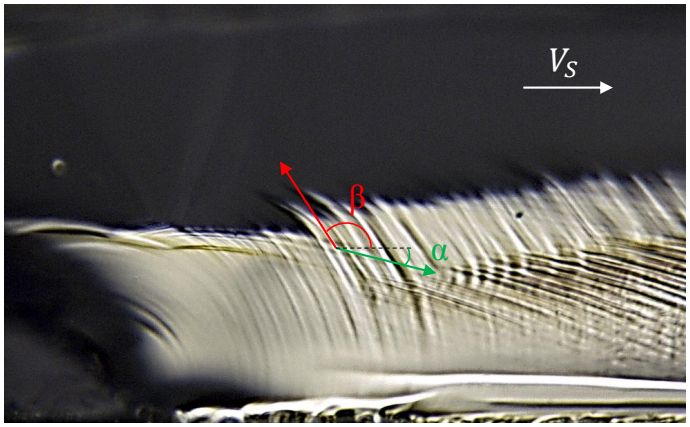

(a)

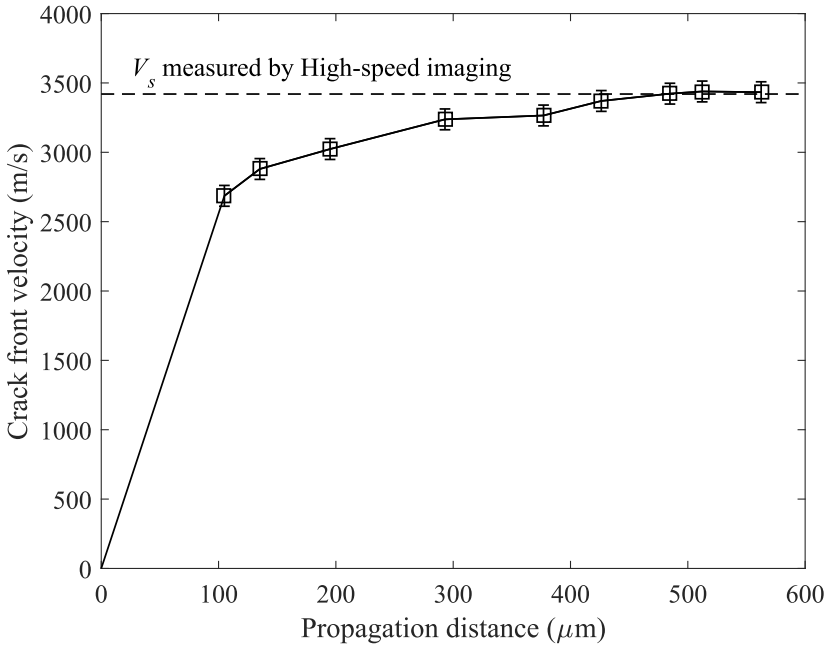

(b)

FIGURE 3.19: Crack front propagation velocity determined based on the Wallner lines. Determination of the extension direction at the interaction spot for the primary Wallner lines and the secondary Wallner lines(a), and $V_{transient}$ as a function of the crack propagation length (b).

4 Discussion

The fracture toughness of low energy planes in silicon has been calculated with full-density functional molecular dynamic simulations, as Γ_0^{111}=2.88 J/m^2 and Γ_0^{110}=3.46 J/m^2 [PÉR 00c]. When the load is perpendicular to the (110) cleavage plane, which is the case in this work, the effective fracture dissipation of the (111) plane becomes $\Gamma_*^{111} = \Gamma_0^{111}$ / cos(35.26°) = 3.53 J/m^2 due to the 35.26° tilt angle (see Fig. 2.5(a)). Thus, the (110) plane is the lowest energy fracture path under the present three-line bending tests.

As shown by experimental results, at low V_s, the crack propagates solely on the (110) plane. As V_s increases, the (110)-(111) crack deflection occurs and the complete crack deflection rises at $V_s > 3300$ m/s. In line with these observations, a theory of dynamic fracture toughness evolution [SHE 04, SHE 05] was proposed, such that as the local crack velocity increases, the dynamic fracture energy of the (111) plane Γ_D^{111} would become lower than that of the (110) plane Γ_D^{110}, as a result of different evolution rates. However, the stable (110) cleavage under tension [HAU 99, CRA 00] and four-line bending load [ZHA 17, ZHA 18a] at high crack velocity (up to $0.85C_R$) reveals that aforementioned theory might not be generalized.

4.1 Dynamic fracture energy of (110) and (111) plane at crack deflection point

For the elastodynamic crack propagation in a brittle solid, the Freund condition [FRE 98] can be used to determine the dynamic fracture energy Γ_D, based on the energy balance with the energy release rate G, the crack propagating velocity V and the Rayleigh wave speed C_R :

$$\Gamma_D = G(1 - \frac{V}{C_R}) \tag{3.10}$$

Equation (3.10) predicts that a variation of Γ_D, G or C_R will induce an instantaneous change on the crack velocity V. Upon the cleavage plane's deflection during the crack propagation, the local crack velocity drop highlighted in Fig. 3.16c is hence generated by the sudden variation of the dynamic fracture energy and the Rayleigh wave speed. In this respect, the local velocity drop enables to estimate the variation of Γ_D at the deflection position.

In order to compare Γ_D^{111} and Γ_D^{110} around the crack deflection point, only the (110)-(111) transition zone at the beginning of the crack deflection is taken into account to ensure that the crack front standing on the (110) plane rests planar. The local crack velocity drop (see Section. 3.3.3) is determined by Eq. (3.8) and the local kink of primary Wallner lines at the deflection point, as shown in Fig. 3.20(a). With the Rayleigh wave speed C_R on both the (110) and the (111) planes [PRA 69], the ratio between Γ_D^{111} and Γ_D^{110} can be calculated as :

$$\frac{\Gamma_D^{111}}{\Gamma_D^{110}} = \frac{G^{111}}{G^{110}} \frac{C_R^{110}(C_R^{111} - V_l^{111})}{C_R^{111}(C_R^{110} - V_l^{110})} \tag{3.11}$$

We presume that the energy release rate is continuous along the crack front and no instantaneous jump occurs at the deflection points. Thus, the ratio of G^{111} to G^{110} is set equal to one. Fig. 3.20(b) shows the ratio between Γ_D^{111} and Γ_D^{110} as a function of the local crack velocity on the (111) cleavage plane, V_l^{111} at the (110)-(111) deflection points. It can be noticed that the ratio is nearly constant and is equal to 1.026, with V_l^{111} varying between $0.29C_R^{111}$ and $0.38C_R^{111}$, and V_l^{110} varying between $0.3C_R^{110}$ and $0.4C_R^{110}$. Experimental results [CRA 00] show that, for the crack velocity below $0.6C_R^{110}$, Γ_D^{110} is approximately equal to 3.46 J/m^2. Hence, it can be deduced that Γ_D^{111} remains equal to 3.53 J/m^2. Consequently, we can conclude that during the (110)-(111) crack deflection, Γ_D^{111} remains larger than Γ_D^{110}, which confirms that the (110)-(111) crack deflection is not driven by the evolution of dynamic fracture toughness reported in the previous works [SHE 04, ATR 12]. Moreover, Sherman and co-authors recently proposed that Γ_D is barely dependent of the crack speed for the (110)[1-10] and (111)[11-2] cleavage systems [SHA 18], which is also in contrast to their theory of dynamic fracture toughness evolution.

4.2 Crack deflection and recovery

What is the main reason for the crack deflection ? When comparing the crack deflection phenomena between the two pre-crack positions shown in Fig. 3.8, one can notice that the crack deflections occur at higher velocity for the crack propagating 2 mm beside the contact line than that propagating under the contact line. This clearly indicates the influence of contact perturbations. According to Hertz's contact theory [JOH 87], both the contact half-width and the depth of the maximum shear stress under the contact line are less than 10 μm for all tests. In this sense, this dimension is small compared with the total specimen thickness 200 μm, hence, the static contact stress field should have little effect on the crack propagation.

From the previous analysis, it is found that the crack deflection involves the SWL and develops along these lines. Considering that the Wallner lines result from the crack front-shear waves interactions, the crack front is thus locally perturbed by the shear stress component, leading to a mixed-mode fracture. At the fracture initiation, the crack passes from static to dynamic state with a steady-state crack propagating velocity. Fig. 3.19 shows that this transition is extremely fast. Under the constant displacement loading configuration, the contact stresses under the punch line are suddenly released, accompanied by the drop of the external load. Hence, in the light of the crack deflection at crack initiation, we propose that shear waves are engendered upon sudden release of the contact stress. Due to the diamond-sawn surface of the wafer, the surface roughness leads to multiple point-contact scenarios instead of a perfect line contact. The surface roughness can break the symmetry of the contact stress field [BAI 91, NOG 97]. Hence, anti-planar shear waves will be generated and promote the crack deflection. In the light of the intermittently subsequent partial crack deflections (as seen in Fig. 3.9c and d), we suppose that shear waves are released

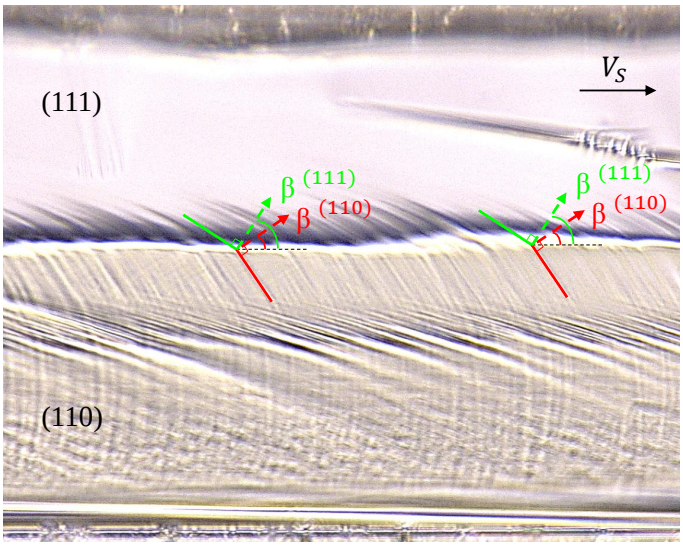

(a)

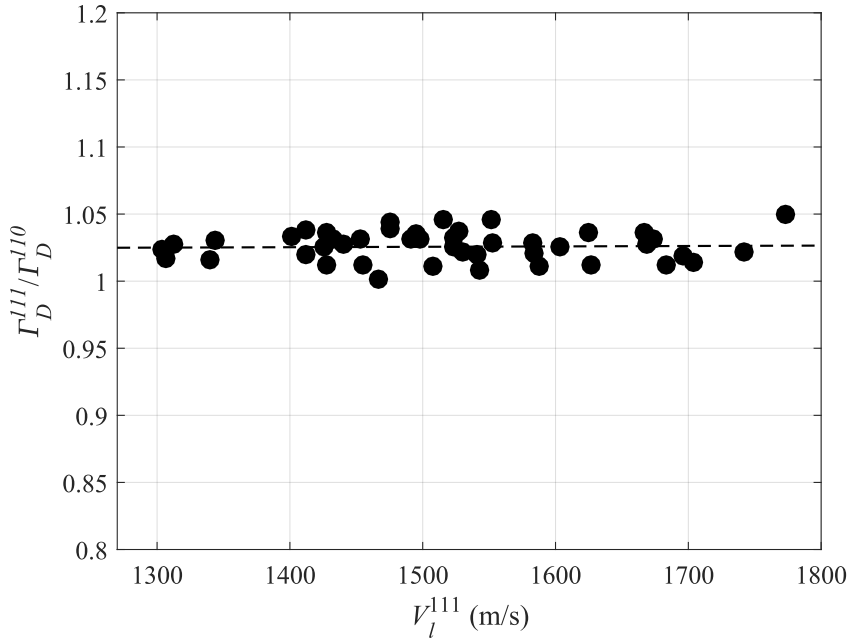

(b)

FIGURE 3.20: $\Gamma_D^{111}/\Gamma_D^{110}$ determination. (a),Kink of the primary Wallner lines at the (110)-(111) deflection point. (b), Ratio of dynamic fracture toughness between the (111) cleavage system, Γ_D^{111}, and the (110) cleavage system, Γ_D^{110}, versus local crack velocity on the (111) cleavage plane V_l^{111}, at the (110)-(111) crack deflection point.

by the local contact stress concentrations due to the as-sawn surface morphology of the wafer. As a result, anti-planar shear waves emanate. With the increase of the crack length,

the local contact overstresses weaken and the effect of shear waves disappears. Upon the crack initiation, since the crack front expands from the bottom of the fracture surface, the crack front interacts with shear waves in the middle of the fracture surface. Upon the crack propagation, this interaction raises from the top side of the crack front, since the crack front is well developed. This explains why the crack deflection at the crack initiation occurs in the middle of the fracture surface and subsequent crack deflections occur near the top surface of the specimen.

The strength of the shear waves depends on the contact stresses. When large contact stresses are released, as in the case of high fracture stress, the shear waves have a strong effect on the crack deflection. As a result, not only the (110)[001] cleavage system will deflect to the (111)[11-2] cleavage system in the presence of any slight shear contribution [KER 08b], but the total (110) cleavage system would switch to the (111) cleavage system. Hence, when the fracture stress is sufficiently high, as in the high crack velocity case, the (110)-(111) crack deflection will develop exactly along the SWL (see Fig. 3.12c). Moreover, since the shear waves are characterized by a strong decay (following a $1/r^2$ decay), the (110)-(111) deflection may not develop through the total specimen thickness and the partial crack deflection occurs. Besides, the deflection for a crack propagating 2 mm beside the contact line will engender at a higher fracture stress than that under the contact line due to the decay of the shear waves prior to affecting the crack front.

When the contact induced shear waves disappear along the crack propagation, the (111)-(110) crack recovery takes place. This implies that the crack always pursues the most preferential cleavage plane. The dependence of the recovery length on the crack velocity indicates that the (111)-(110) deflection is independent of the previous shear waves perturbations. Since the local crack velocity at the lowest side of the crack front is maximum (see Fig. 3.16c), so is the dynamic fracture energy, the crack recovery from the lowest side is not energetically favorable. Hence, the crack recovers to the (110) plane from the top side of the specimen and progressively spreads to the lower side to minimize the extra energy dedicated to the crack plane switch. In this respect, the fracture path in the absence of stress perturbations in crystalline silicon conforms to the principle of minimum energy dissipation.

4.3 Experimental validation of the shear waves effect

In this part, we present a typical fracture result to highlight the shear waves effect on the cleavage plane deflection. The fracture test was carried out under the bending tests, in which no pre-crack was produced in the silicon specimen [ZHA 18b]. It was found that the first crack nucleates and propagates straightly right underneath the punch roller. Afterward, since the sudden release of the curvature of the bent specimen generates a burst of flexural waves that lead to local overstresses of the specimen [AUD 05b], multiple cracks appear. Here, we focus only on the initiation of the first crack where the stress waves generated by other cracks have no influence yet.

Fig. 3.21 shows the fractography of the crack initiation and propagation of about 1.8 mm. It can be noticed that the crack initiates from a wire-sawing induced sub-surface

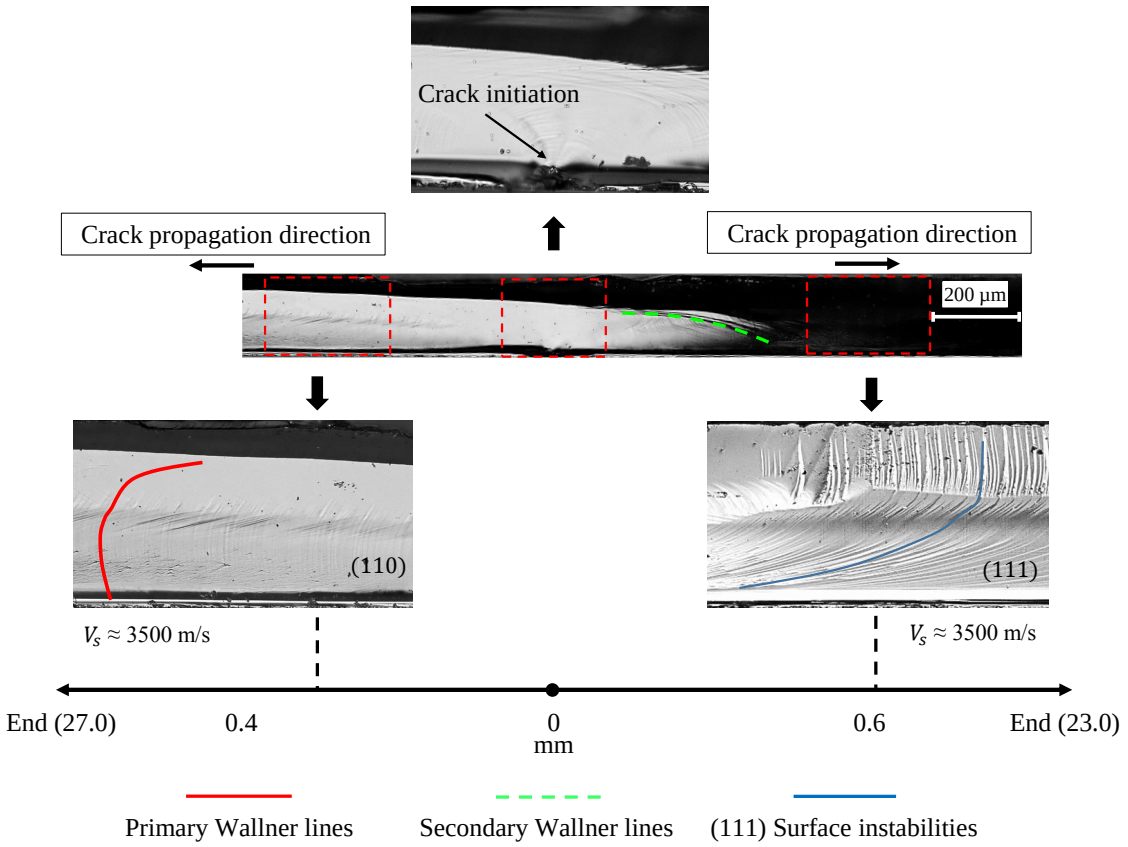

FIGURE 3.21: Crack deflection under contact perturbations. Fractographic reconstruction of the crack initiation and propagation. The first 1.8 mm of the fracture surface is presented in the center and surrounded with three close-ups highlighting the crack initiation, crack propagation on the (110) plane as well as crack propagation on the (111) plane.

micro-crack. The fracture history is outlined below :

• The fracture initiation takes place on the (110) plane which produces a smooth fracture surface and the primary Wallner lines appear. The fracture origin is located near the half length of the specimen, so the crack propagates in two opposite directions, as can be reflected by the opponent expanding direction of the primary Wallner lines.

• When propagating to the right side, quickly, the crack front is affected by the shear waves emitted from upper part of the crack surface to the lower part, and secondary Wallner lines are generated. Meanwhile, the deflection nucleates and the crack front gradually deflects from the (110) plane to the (111) plane during the crack front-shear waves interaction. The crack finally propagates on the (111) plane at about 0.6 mm as highlighted by the close-up fractography after the shear waves perturbations.

• However, when the crack propagates to the left side, no secondary Wallner lines appear on the fracture surface, hence the crack front is not affected by the shear waves perturbations. As a result, the crack propagates stably on the (110) plane.

• From the morphology of the fracture surface, one can infer that the crack fast acce-

lerates to the steady state propagation velocities for both sides, which are equal to about 3500 m/s. This velocity corresponds to 78.5% of the Rayleigh wave speed.

This experimental result clearly evidences the shear waves effects on the moving crack front which leads to the (110)-(111) crack deflection under contact perturbations. Discrete contact points with various heights lead to different strength of the local contact overstress. Hence, we suggest that the burst of shear waves only occurs at one side of the crack propagation direction is due to the random surface roughness of the as-sawn silicon wafer.

5 Conclusion and remarks

The fractographic analysis provides the possibility to systematically investigate and understand the material failure, especially for the brittle fracture in the case where the whole fracture of material occurs abruptly. Concerning the fracture of the solar-grade single crystalline silicon wafer, it is found that the fracture origin is commonly due to the subsurface micro-crack induced by the diamond wire sawing. Once initiating, the fracture of the silicon wafer takes places very fast since the crack instantaneously accelerates to a high propagation speed.

Jointly with the high speed-imaging technique and the controlled pre-crack, the dynamic fracture behavior during the failure of the silicon wafer can be studied, using the fractographic analysis. The (110)-(111) cleavage deflection of the (001) single crystal silicon wafer has been revisited based on a large amount of three-lines bending tests. Contact effects have been investigated using two crack positions (right under the contact line and 2 mm beside) and fractographic analysis. It is deduced that the contact induced shear waves affect the crack propagation. The crack front-shear wave interaction impels the crack to deflect from the (110) plane to the (111) plane and leaves secondary Wallner lines on the fracture surface. Besides, the (110)-(111) crack deflection tends to dominate the whole fracture surface when encountering high-strength shear waves. Moreover, we highlight that the dynamic fracture energy of the (111) plane is always higher than that of the (110) plane until a crack velocity of $0.4C_R$. In spite of complete (110)-(111) crack deflection, the (111) cleavage is not permanent and the crack recovers to the (110) cleavage plane. The (111)-(110) recovery occurs even though the crack velocity reaches $0.8C_R$, confirming that the fracture energy criterion dominates the cleavage plane selection even in high speed fracture process.

6 Outlook

- Microbranches

When propagating at high velocity, the crack front performing as a 'single' planar front at low velocity, however, becomes unstable and the microbranching instability occurs. The instability appears at a critical crack velocity of about $0.3C_R$ - $0.4C_R$, where C_R is the Rayleigh wave speed. It has been observed in amount of brittle materials, such as glass

[SHA 99, SHA 02], poly-methyl-methacrylate (PMMA) [SHA 96a, SHA 96b, SHA 99] and brittle polyacrylamide gel [LIV 05, BOU 15]. Above critical velocity, microscopic crack branches sprout from the main crack that extend away for a short distance inside the material and disappear. This is differs from the macroscopic crack bifurcation where a single crack separates into multiple cracks propagating at different directions.

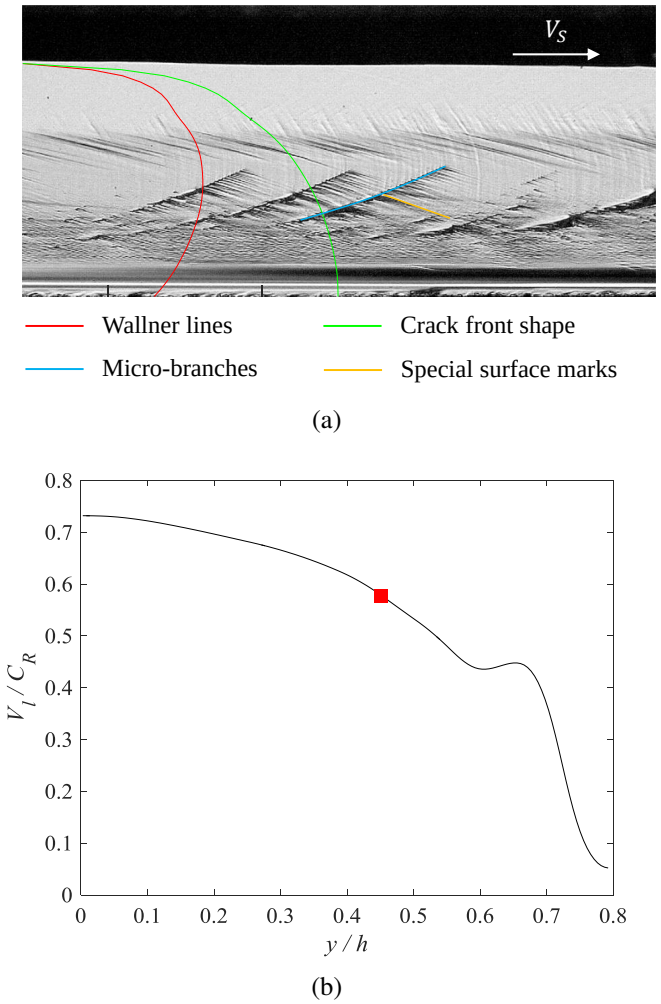

FIGURE 3.22: (a) Fractography of microbranching instabilities on the (110) cleavage plane at the crack steady-state propagation velocity of 3500 m/s. The Wallner line and the crack front shape are highlighted by the red and green curves, respectively. The local microbranch is highlighted by the blue line. (b) Normalized local crack velocity as a function of the height along the crack front. Red mark highlights the death position of the microbranches.

Fig. 3.22(a) shows the fracture surface morphology of single crystalline silicon wafer at V_s = 3500 m/s. At the lower half portion of the fracture surface, periodic local microbranches can be observed, as highlighted by the blue line. The microbranching morphology observed on the fracture plane is generated by the initial portion of microbranches

while the rest extends inside the material. However, the behavior of microbranches inside the material remains to be discovered. The crack front shape (green curve) reconstructed from the Waller line (red curve) is shown. It can be noticed that the onset of microbranching phenomenon is spatially continuous and localized, which emerges at the higher local crack velocity side and extends to the lower local crack velocity side along the normal direction of the crack front, and finally dies at approximate the height of 0.45h, where $V_l = 0.59C_R$, as shown in Fig. 3.22(b). The spatial localization of the microbranches is the result of the bistable-state coexistence of the planar crack front and the local crack branches [LIV 05, BOU 15].

With the occurrence of microbranches, some special surface markings pointing to the lower side of the fracture surface appear right behind the microbranches, as highlighted by the orange line in Fig. 3.22(a). These markings emerge without interruption from the microbranching lines and form a corrugated fracture surface. [SHA 02, LIV 05] first reported that crack front waves will be generated by the microbranching events due to the local jump of the fracture energy dissipated via microbranches, and leave typical surface marks on the fracture plane. The crack front waves are found as nonlinear entities which behave like solitary waves [SHA 01]. Hence, it will be interesting to study : do these surface markings are crack front waves traces ? how do they emerge ? and what are their characteristics ? With these questions, the next chapter will focus on the investigation of corrugated fracture surface traces of single crystalline silicon wafer.

Chapter 4

Rapidly propagating crack front and self-emitted corrugation front waves

Elastic waves are fostered when dynamic crack front travels through material heterogeneity. The interaction between the elastic waves and the crack front leads to the out-of-plane motion of the crack and alters the morphology of fracture surface. Among them crack front waves are predicted as solitary waves that propagate solely along the crack front in linear elastic medium. However, due to various characteristics of different elastic waves, the crack front dynamics under the wave perturbation and the corresponding fracture surface patterns remain elusive. Here, we show that in single crystalline silicon excluding material asperities, local intrinsic heterogeneity of fracture toughness kinks crack front and continuously produces nonlinear elastic waves, which we call corrugation waves because they incorporate periodic out-of-plane component. These waves twist the crack front and generate periodic markings on the fracture surface. They grow from angstrom amplitude to few hundreds of nanometers and propagate with long lifetime at a frequency-dependent speed, while keeping a scale-independent shape. In particular, the corrugation waves collide in a particle-like manner rather than proceeding with a linear superposition upon interaction, which presents a characteristic of solitary wave motion.

Contents

1 Introduction

Crack propagation is the main cause of catastrophic material failures. It has been intensively studied for decades but remains challenging due to intricate dynamic behavior in link to atom vibration. Linear elastic fracture mechanics (LEFM) [FRE 98] describes crack tip in two-dimensional media as an energy sink, around which all the dissipation processes when the crack propagates. The crack propagation speed v is determined by the balance between the elastic energy flux into the crack tip G and the dynamic fracture energy $\Gamma(v)$ (the energy needed to create a crack of unite area with speed v). In three dimensional (3D) systems, crack front geometry should be considered. The local crack velocity at every point of the front v_l is governed by the local energy balance $G_l = \Gamma_l(v_l)$ which controls the global fracture dynamics [RAM 97b, KOL 18].

Crack front is generally stable under pure tension (mode I) which produces 'mirror-like' fracture surface [RAM 97a, CRA 00], while fluctuation of the fracture energy breaks the stability and generates 3D markings on the fracture surface [FIN 91, PON 10, CHE 17]. A recent study [KOL 18] showed that the crack front develops a localized 'cusp-like' shape in response to asymmetric energy sink which leads to the faceted fracture surface. In brittle amorphous materials, translational symmetry of the crack tip breaks and micro-cracks branch out from the main crack at v 30% - 40% of the Rayleigh wave speed, generating the so-called micro-branching instabilities [SHA 96a, BOU 15]. In brittle gels, the straight crack becomes oscillatory due to near-crack nonlinear elastic fields at ultrahigh-speed (v $\sim$ 90% of the shear wave speed) achieved by suppressing the micro-branching event in very thin samples [LIV 07, CHE 17].

Elastic waves can also destabilize the crack. Shear waves emitted from material flaws or ultrasonic transducers have been shown to twist the crack front and generate the well-known Wallner lines [BON 03, WAN 19]. Lamb waves emitted by the propagating crack during the debonding of implanted silicon layers interact with the crack front after reflection from the specimen boundaries and leave periodic surface patterns [MAS 18]. Among others, crack front waves have been first numerically predicted as the production of interaction between a moving crack front and local inhomogeneities with different fracture toughness [MOR 98, MOR 00]. These waves propagate along the crack front and locally change the in-plane dynamics of the crack. Out-of-plane components [WIL 97, ADD 13] were later on revealed by extended modelling studies. Surface markings produced by crack front waves were first reported in fracture tests on brittle soda-lime glass incorporating artificial material asperities [SHA 01, SHA 02], and then observed on the fracture surface of the brittle polyacrylamide gels generated from the microbranches [LIV 05]. However, the triggering of the crack front waves through intentional material flaws makes the study debatable [BON 03, SHA 04, BON 04], since the possibility of Wallner line generation cannot be clearly excluded. More recently, in the fracture test of as-sawn single crystalline silicon wafer under pure bending load, [ZHA 18a] found that the crack front involves a local velocity fluctuation and generates periodic undulation on the fracture surface at high velocity. The authors suggested that these surface markings are traces of crack front waves resulting from the local crack velocity fluctuation. Since Wallner lines

are also present on the fracture surface, no in-depth characterization of these markings has been performed in their work.

In this chapter, we investigate the special fracture surface markings at both macro and micro scale of the single crystalline silicon wafer under pure bending, which exclusively arise in high-speed cracks. The objective is to validate the proposal of self-emitting elastic waves and characterize their attributes. Both as-sawn silicon wafers and mirror-polished silicon wafers are used to study the crack front behavior and the surface corrugations excluding influences of the Wallner lines, respectively. We propose that the special surface markings are generated by a new kind of nonlinear elastic waves, namely corrugation waves, that nucleate from intrinsic heterogeneity of fracture toughness or micro-branching events during high-speed crack propagation. We demonstrate that the dynamic fracture energy along the crack front, depending on the crystallographic direction, performs an abrupt increase from twice surface energy at critical velocity. This jump coincides with the emergence of out-of-plane corrugation waves which run along the crack front and twist the crack front to leave well-defined surface corrugation markings. Besides, the corrugation waves were found to be nonlinear entities, exhibiting a scale-independent shape along the steady-state crack front and a long lifetime with the amplitude down to angstroms. This fulfills, in some respects, the solitary character of the front waves [SHA 01]. Furthermore, we show, in addition to the a scale-independent characteristic shape [SHA 01], two unrevealed attributes of these waves : nonlinear dispersion and soliton-like interaction.

2 Materials and experimental methods

100 experiments, including 30 on mirror-polished silicon samples (section 1.4 in Chapter 2) and 70 on as-sawn silicon samples (section 1.3 in Chapter 2) were carried out under four-line bending tests (section 3 in Chapter 2). The dimensions for polished and as-sawn silicon samples are $50 \times 30 \times 0.17$ mm^3 and $50 \times 50 \times 0.19$ mm^3, cut from (001) silicon wafers with a doping concentration (p-type) of 5.44 x 10^{15} atoms/cm^3. The single crystal is oriented such that the surface of specimens is perpendicular to the [001] direction and the two edges are parallel to the <110> directions. A single crack was driven from a (110) seed crack introduced at the center of the sample edge using a Vickers indent. The crack velocity was measured by the high-speed camera (Phantom V710). For the as-sawn silicon samples, we recorded images with a spatial resolution of 97.6 μm/pixel and an acquisition rate of 180,000 frames per second. For the mirror-polished silicon samples, we recorded images at a spatial resolution of 89.3 μm/pixel and an acquisition rate of 340,000 frames per second. The uncertainties on crack speed measurement are 70 m/s and 121 m/s for as-sawn and mirror-polished samples, respectively, since we took an uncertainty of 4 pixels on the crack tip location.

Abundant tests were performed to ensure the reliability of the experimental results. Thanks to various seek crack sizes, a wide range of steady-state crack velocities v_s, from 960 m/s ($0.22c_R$) to 3650 m/s ($0.82c_R$) was obtained, allowing extensive examination on crack dynamics.

3 Crack front dynamics

It has been shown in Chapter 3 (section 2.2) that the crack front involves a local curvature kink at $v_s > 2750$ m/s ($0.62c_R$). In this section, we will focus on the dynamics of the crack front under pure bending based on the fracture tests on as-sawn sample, to explain why this local kink of the crack front occurs.

3.1 Crack front kinks

Fig. 4.1 shows the (110) cleavage surface at different v_s. The crack front shape is reconstructed via the retroactive decomposition of the Wallner lines (see Chapter 3, section 2.2) and is shown in Fig. 4.2(a). The anisotropic shear wave speed along the (110) plane [PRA 69] was used in this work. The Wallner lines shape were determined via the striking visual differences through the microscopic observations thanks to the contrasting light intensity of the peak and valley of the Wallner lines or the topographic measurements through the laser scanning profilometer (Altisurf-500). At $v_s < 0.62c_R$, the crack front exhibits a quarter-ellipse shape. At $v_s > 0.62c_R$, jointly with the Wallner lines kinks, we found that the crack front incorporates a local kink as highlighted by the red circles in Fig. 4.1. The kink appears at a higher position along the crack front with the increase of v_s. The local crack front velocity v_l, which is normal to the crack front and forms an angle θ relative to the x direction (Fig. 4.2(b)), is given by $v_s cos(\theta)$. As shown in Fig1. 4.2(b). in low-speed cases, v_l monotonically decreases from bottom to top along the crack front, while in high-speed cases, the local kink of the crack front is reflected by a v_l fluctuation.

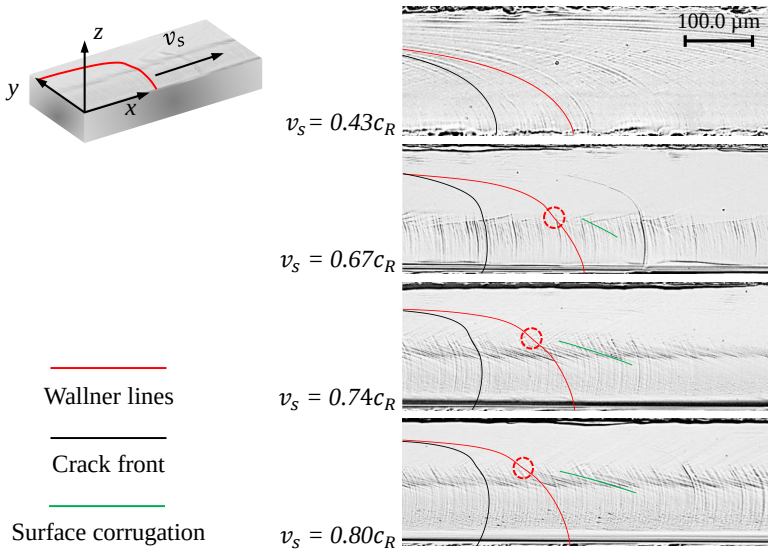

FIGURE 4.1: Fracture surface patterns of (110) cleavage plane (xy plane) at different crack steady-state propagation velocities v_s. The crack front propagates along the axis x pointing to the [1-10] direction. Local kinks of the crack front are highlighted by the red dotted circles.

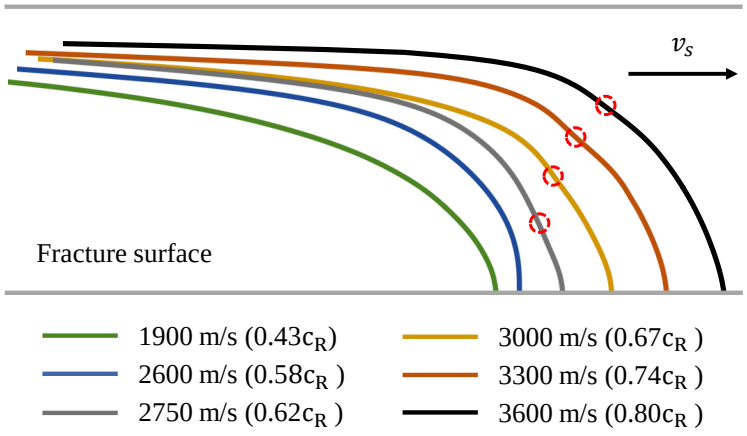

(a)

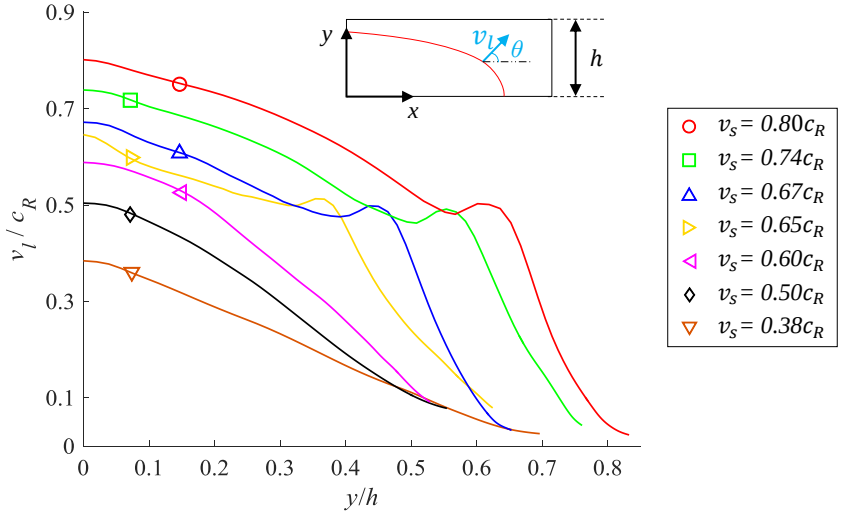

(b)

FIGURE 4.2: (a), Crack front shapes for different v_s. Local kinks of the crack front are highlighted by the red dotted circle when $v_s > 0.62c_R$. (b), Normalized local crack front velocity v_l/c_R as a function of the vertical position y/h along the crack front for seven experiments with different crack steady-state propagation velocities v_s. The angle θ depicts the local crack front direction relative to the x direction and h represents the thickness of the specimen.

What determines the crack front motion ? As the crack front advances, a driving force must be provided to the crack in order to create new fracture surface, i.e. the stored mechanical energy release rate G. In the case of quasi-static crack propagation, G is equal to twice surface energy 2γ. While in the case of a dynamic crack propagation, G is balanced with the dynamic fracture energy $\Gamma(v)$ including all material and crack velocity-dependent energy dissipations [FRE 98, SHA 99, BUS 01]. LEFM [RAM 97b] describe

the local energy balance for every position along the crack front as $G_l = \Gamma_l(v_l)$, where v_l is the local crack velocity normal to the crack front, Γ_l is the local fracture energy and G_l is the local energy release rate.

When the applied load to the crack is time-independent, the local energy balance for a steady-state propagating crack can be given by :

$$\Gamma_l(v_l) = G_l(L)(1 - \frac{v_l}{c_R}) \tag{4.1}$$

where $G_l(L)$ is the local energy release rate for a crack at rest of length L, which is independent of v_l but determined by the sample geometry and the applied loading. Equation (4.1) implies that a sudden variation in Γ_l will induce a corresponding variation in v_l. Hence, the v_l fluctuation is expected to be the consequence of a local fluctuation of dynamic fracture energy.

3.2 Anisotropic dynamic fracture toughness

Equation (4.1) is strictly applicable to the crack propagation in a bounded body before the stress waves reflected from the boundaries, which perturb the stress field around the crack front [FRE 98]. Hence, in order to calculate $G_l(L)$, only the crack geometry at the very beginning of the steady-state regime was simulated assuming that the crack front was not perturbed by these stress waves [1].

We used the commercial finite element (FE) software Abaqus 6.14-5 to calculate the strain energy release rate G_l along the crack front. The computation took into account the experimental condition and the crack front shape. For each simulation, the seek crack length and the crack geometry at the very beginning of the steady-state regime was modelled, which were determined by the post-mortem analysis of the fracture surface, as shown in Figs. 4.3. Half of the system was considered due to the symmetric configuration with respect to the fracture plane. The stiffness matrix of the orthotropic elasticity of the single crystalline silicon was used as reported in [ZHA 16b]. The silicon sample was meshed by 20-node quadratic brick elements with reduced integration (C3D20R element in Abaqus), and the crack front was surrounded by 15-node quadratic triangular prism elements (C3D15) to well represent the crack-tip sharpness. Moreover, a mesh refinement (down to 3 μm) was employed around the crack front to obtain higher accuracy of the stress field which is critical for the contour integration computation. The number of elements varied from 38300 to 86000 depending on the dimension of the crack front. The model was first validated through the coincidence of the experimental and numerical load-displacement curves prior to fracture (see Figs. 4.4). The morphology of the seed crack was not considered since the influence of the seed crack on the crack front behavior at steady-state is

1. One can assume that the crack front propagates along the (110)[1-10] direction at a mean velocity of 1000 m/s, and the longitudinal waves are emitted at the crack initiation, which propagate along the (110)[110] direction at a velocity of 9183 m/s [MAD 02]. After the wave reflecting from the sample boundary and reaching the crack. The crack front has propagated a distance of 5.44 mm and has attained the steady-state before it is affected by the longitudinal waves

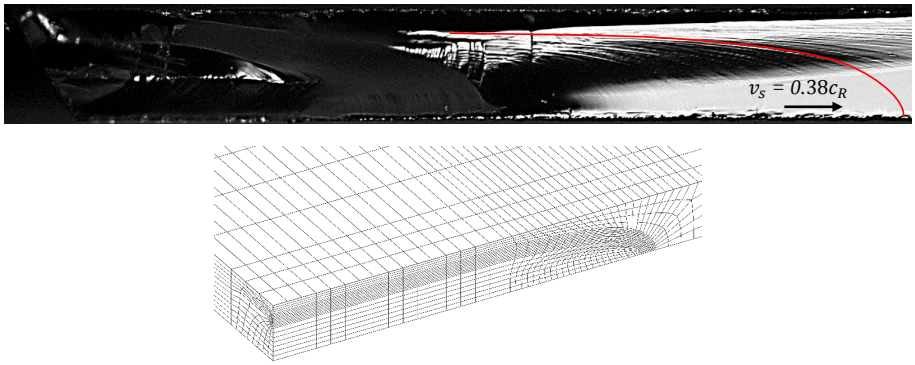

(a)

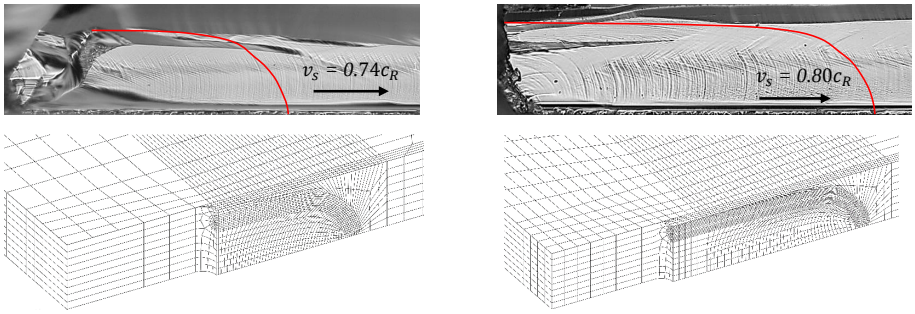

(b)

FIGURE 4.3: Mesh of a crack front at the beginning of the steady-state regime for (a), $v_s = 0.38c_R$, (b), $v_s = 0.74c_R$ (left) and $v_s = 0.80c_R$ (right). The crack front shape and length at the beginning of the steady-state regime are highlighted by the red curve.

trivial (see Figs. 4.7). Besides, only the in-plane crack front deformation was considered. The out-of-plane corrugations on the crack front presenting a nano-scale dimension could not be addressed by the present FE simulations. However, the influence of these corrugations on the stress field can be neglected since the J-integral takes contours far away from the crack front. The strain energy release rate along the crack front was calculated using the J-integral method [RIC 68] when the applied punch displacement in the simulations reached the punch displacement upon fracture in the experiments.

Seven cracks with v_s varying from $0.38c_R$ to $0.80c_R$ are analyzed. The results of $G_l(L)$ distribution along the crack front as a function of normalized vertical position y/h for different v_s cases are shown in Fig. 4.5(a). The $G_l(L)$ increases monotonically along the crack front from top to bottom, while a local fluctuation appears due to the curvature kink of the crack front. The local dynamic fracture energy Γ_l is then calculated using v_l (Fig. 1b), G_l and c_R [PRA 69]. The Γ_l distribution along the crack front for each v_s is presented in Fig. 4.5(b). The error bars were generated by the uncertainties on the v_s measurement. It is found that $\Gamma_l$is almost constant for $v_s < 0.60c_R$, while it significantly increases for $v_s > 0.65c_R$, manifesting as a local jump at different heights for different v_s. The sharp variation of Γ_l along the crack front occurs at a higher position along the crack front at

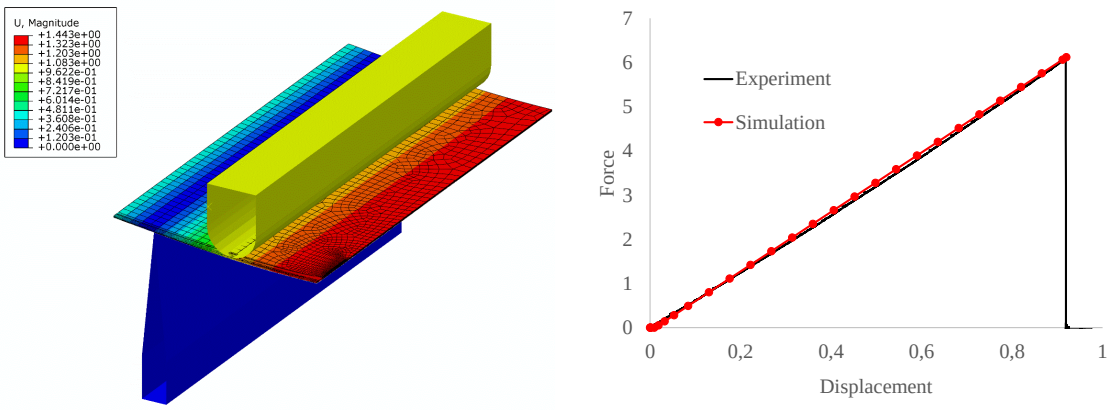

(a) (b)

FIGURE 4.4: (a), Finite element modeling for the G_I calculation. (b) Comparison between the numerical and experimental load-displacement curves.

higher v_s and is well correlated to the v_I fluctuation. After that, Γ_I gradually increases until the bottom of the crack front. Indeed, a sharp increase in local dynamic fracture energy locally slows down the crack front, and the resulting gradient in the local crack velocity consequently produces a kink of the crack front. This phenomenon is similar to the crack front dynamic behavior during the microbranching generation, where the crack front involves an in-plane curvature variation along microbranching formation lines due to the effective increase in local fracture energy caused by the incipient microbranches [KOL 15].

Why does the fracture energy jump at a local position on the crack front ? In the case of dynamic crack propagation, the crack growth criterion applied on the crack front depicts that the relationship that the fracture energy must satisfy the resistance of the material to the crack growth. This resistance, i.e., the dynamic fracture toughness, includes the small-scale dissipations of the advance process of the crack front, which depend on the material and the crack velocity [FRE 98]. Fig. 4.6(a) shows Γ_I as a function of the v_I for the same seven calculations. The local crystallographic direction varying from [1-10] direction (0°) to [001] direction (90°) is reflected by the color code. Γ_I should be considered as the dynamic fracture toughness here. Several phenomena are brought to light : Γ_I at $v_I < 0.46c_R$ is nearly constant and close to the fracture initiation toughness 2γ[PÉR 00b], it then increases at a critical speed v_c varying between $0.47c_R$ and $0.60c_R$, depending on the crystallographic direction along which the crack locally advances. For instance, Fig. 4.6(b) highlights that the increase of dynamic fracture toughness takes place at around $v_c = 0.50c_R$ along (110)[1-11] direction and at around $v_c = 0.60c_R$ along (110)[1-10] direction. It is worth mentioning that the $\Gamma(v)$ evolution in the (110)[110] and (110)[111] cleavage systems are in excellent agreement with ref. [ATR 12], where the authors explain the sharp increase of dynamic fracture toughness by additional energy dissipation of thermal phonon emission during the crack propagation. Besides, the increase of dynamic

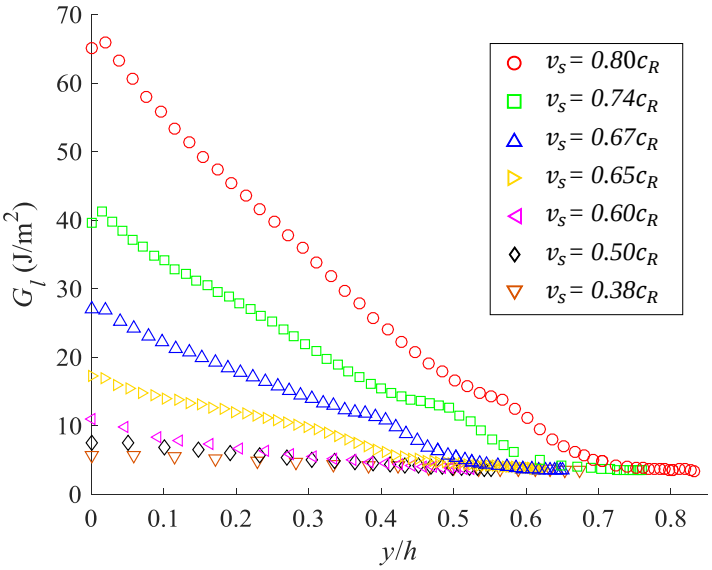

(a)

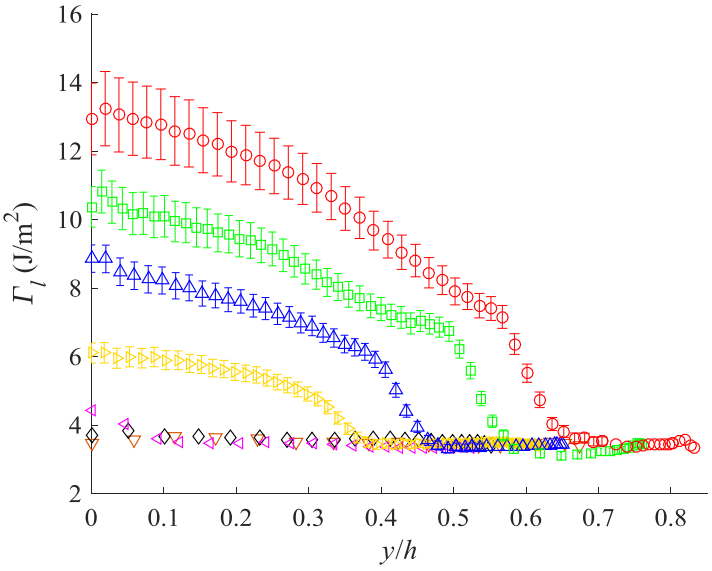

(b)

FIGURE 4.5: (a), G_l along the crack front as a function of normalized vertical position y/h for seven experiments with different v_s. (b), Local fracture energy as a function of the normalized local crack front velocity for the same seven experiments (with the same marks as presented in (a)).

fracture toughness for (110)[2-21] direction at around $v_c = 0.58c_R$ is also shown in Fig. 4.6(b), and the whole anisotropic aspect of the $\Gamma(v)$ evolution on the (110) plane shown in Fig. 4.6(a) is for the first time highlighted in the present work. In conclusion, the fracture

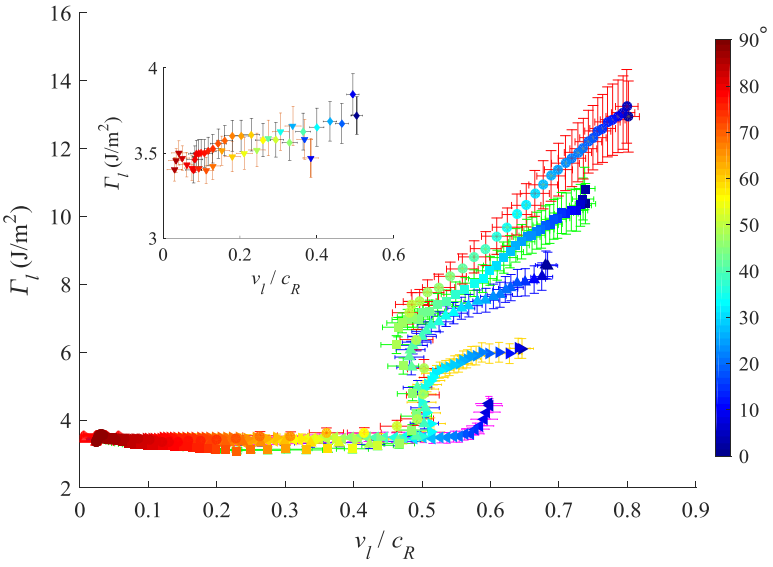

(a)

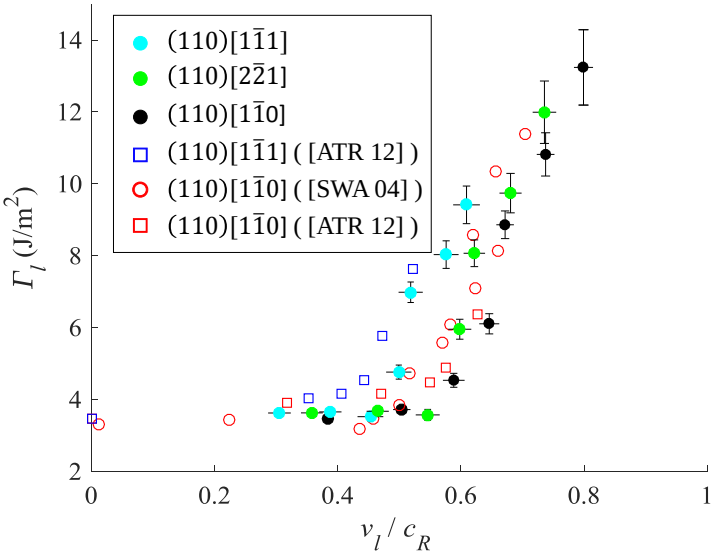

(b)

FIGURE 4.6: (a), Dynamic fracture toughness as a function of the normalized local crack front velocity for the same seven experiments (with the same marks as presented in Fig. 4.5(a)). (b), Dynamic fracture toughness Γ_l as a function of the normalized local crack front velocity v_l/c_R for the (110)[1-11], (110)[2-21] and (110)[1-10] direction. Comparison with molecular dynamics (MD) simulations [SWA 04, ATR 12] represented by blue squares, red squares and red circles, respectively

energy jump is generated by the shape increase of the dynamic fracture toughness above the critical speed v_c that depends on the crystallographic directions. Hence, the generation of the local crack front kink, as well as the the local crack speed fluctuation, are induced by the sharp increase in local dynamic fracture toughness, as the dynamics of the crack front is governed by the ensemble of local energy balances of every point on the crack front $\Gamma_l(v_l) = G_l$.

4 Fracture surface corrugations

As mentioned in the introduction, [MOR 98, MOR 00] numerically showed that the crack front waves are generated in response to a localized heterogeneity of fracture energy. [SHA 01, SHA 02] generated front waves by artificial material asperities, which leave typical surface markings on the fracture surface. In our tests, the local dynamic fracture energy jumps along the crack front provide a generation condition of the crack front waves. Besides, it has been reported in [SHA 02] that microbranches yield an increase of the fracture energy proportional to fracture surface creation, which is accompanied by velocity oscillations [SHA 96b, SHA 96a], and can also trigger the crack front waves. Indeed, from the crack front kink spots where the dynamic fracture toughness jumps, we observed wave-like surface markings, as highlighted by the green lines in Fig. 4.1. In order to validate the front wave assumption, we characterize carefully these special surface markings.

4.1 Surface corrugations at the crack initiation

In this part, we highlight the correlation of the occurrence of the special surface markings with the crack front kink. Under the four-line bending load, the crack acceleration at crack initiation is the same as under three-line bending tests (see Figs. 3.19). The crack is found to rapidly accelerate to the steady-state regime, as also reported in [ZHA 17]. Figs. 4.7(a) - 4.7(c) show the fracture surface morphologies at the crack initiation in the as-sawn silicon samples. Based on the velocity-dependent local kink position of the Wallner lines (see section 2.2.1 of Chapter 3), it can be noticed that, as shown in Fig. 4.7(b), the crack accelerates to a velocity of approximating 3000 m/s after propagating about 130 μm and reaches the steady-state regime after about 550 μm.

Focusing on Fig. 4.7(b), besides the Wallner lines, surface corrugation traces are also observed, as marked in the white rectangle. It can be noticed that these traces do not appear at low crack velocity (see Fig. 4.7(a) for example). The correlation of the occurrence of corrugation traces with the crack velocity can be clearly revealed by the acceleration phase of the crack : no corrugation traces appear within the distance of 100 μm when the crack velocity is lower than 2700 m/s, while the corrugation traces occur at the crack velocity $>$ 2700 m/s. Moreover, it can be noticed that the initiation spot of the corrugation traces rises with the increase of the crack velocity, as shown by the red dotted line in Fig. 4.7. The occurrence of the corrugation traces has no dependence on the seed-crack since the same

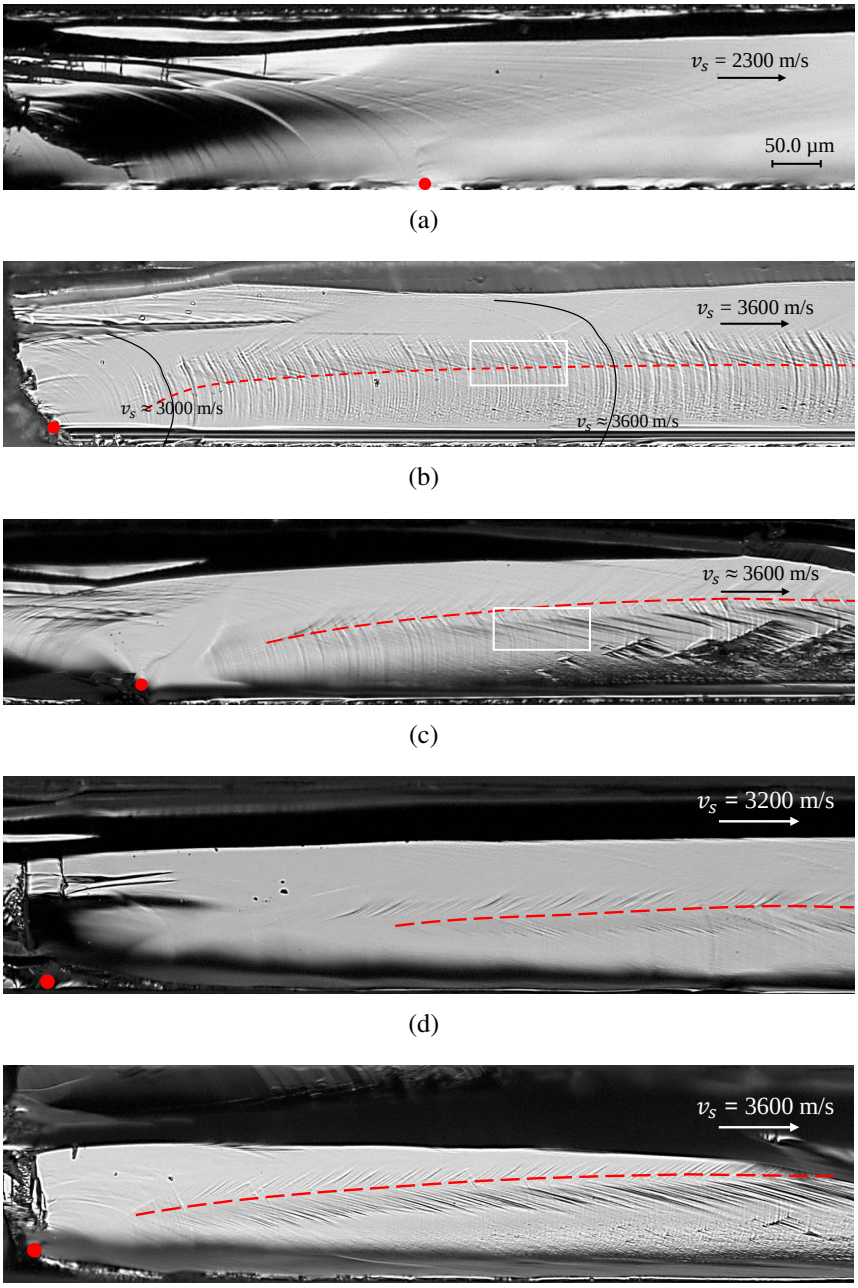

FIGURE 4.7: Fracture surface morphology at the crack initiation. (a) and (b), Crack initiation in as-sawn sample from the seed crack with v_s = 2300 m/s and v_s = 3600 m/s, respectively. (c), Crack initiation in as-sawn sample from the subsurface micro-defect with v_s of about 3600 m/s. (d) and (e), Crack initiation in surface polished sample from the seed crack with v_s = 3200 m/s and v_s = 3600 m/s, respectively. Crack initiation spot is marked by the red dot and surface corrugations are highlighted by the white rectangle.

phenomena can be observed in the case where the crack initiates from the wire sawing induced subsurface micro-defects, as shown in Fig. 4.7(c). Besides, the corrugation traces continuously emit and cover the rest of the fracture surface.

Figs. 4.7(d) and 4.7(e) present the fracture surface morphologies at the crack initiation in surface polished samples. With the surface defect elimination,, the primary Wallner lines are barely generated on the fracture surface. The surface corrugations still occur on the fracture surface and their dependence on the crack velocity can also be observed. Hence, it is noteworthy that, the surface corrugations, especially their source, have no relation with the Wallner lines.

4.2 Surface corrugations at the steady-state crack propagation

The surface corrugations are presented on the whole fracture surface involved in the steady-state regimes of high speed cracks. Fig. 4.8 show the surface corrugations at different crack steady-state velocity varying from 2950 m/s to 3600 m/s for both the as-sawn silicon specimens (left) and the surface polished silicon specimens (right). The fracture surface morphologies are almost identical for cracks with similar steady-state velocity, indicating the reproducibility of the fracture results. Several qualitative behaviors correlating with the crack velocity can be extracted from Fig. 4.8 :

- The corrugation traces nucleate at the same position as the local kink of the Wallner lines, which rises with the increase of the crack velocity, as highlighted by the green circle in Fig. 4.8.
- With the crack advancing, the corrugation traces extend to the lower portion of the fracture surface. They manifest as an approximately straight line in the middle of the fracture surface incorporating a tilt angle relative to the crack advancing direction that decreases with the increase of the crack velocity as highlighted by the red lines. No corrugation traces extending to the upper portion of the fracture surface has been observed.
- After initiation, the undulation amplitude of surface corrugations gradually increases then decreases. They are more remarkable at higher crack velocity. This suggests that the maximum amplitude of the surface corrugation increase with the crack propagation velocity.
- With the emergence of the local microbranches, new and more visible corrugation traces are triggered as can be seen on the fracture surface with V_s = 3600 m/s. These traces form a higher tilt angle.

The corrugations traces show similar characteristics in the fracture of as-sawn silicon sample and the surface polished silicon sample, regardless of the occurrence of the Wallner lines, which confirms the independence of the surface corrugations on the Wallner lines. Here, we show the characteristics of surface corrugations traces involving a qualitative dependence on the crack velocityat the macro-scale. The quantitative analysis of the surface corrugations at the nano-scale will be presented in the next section.

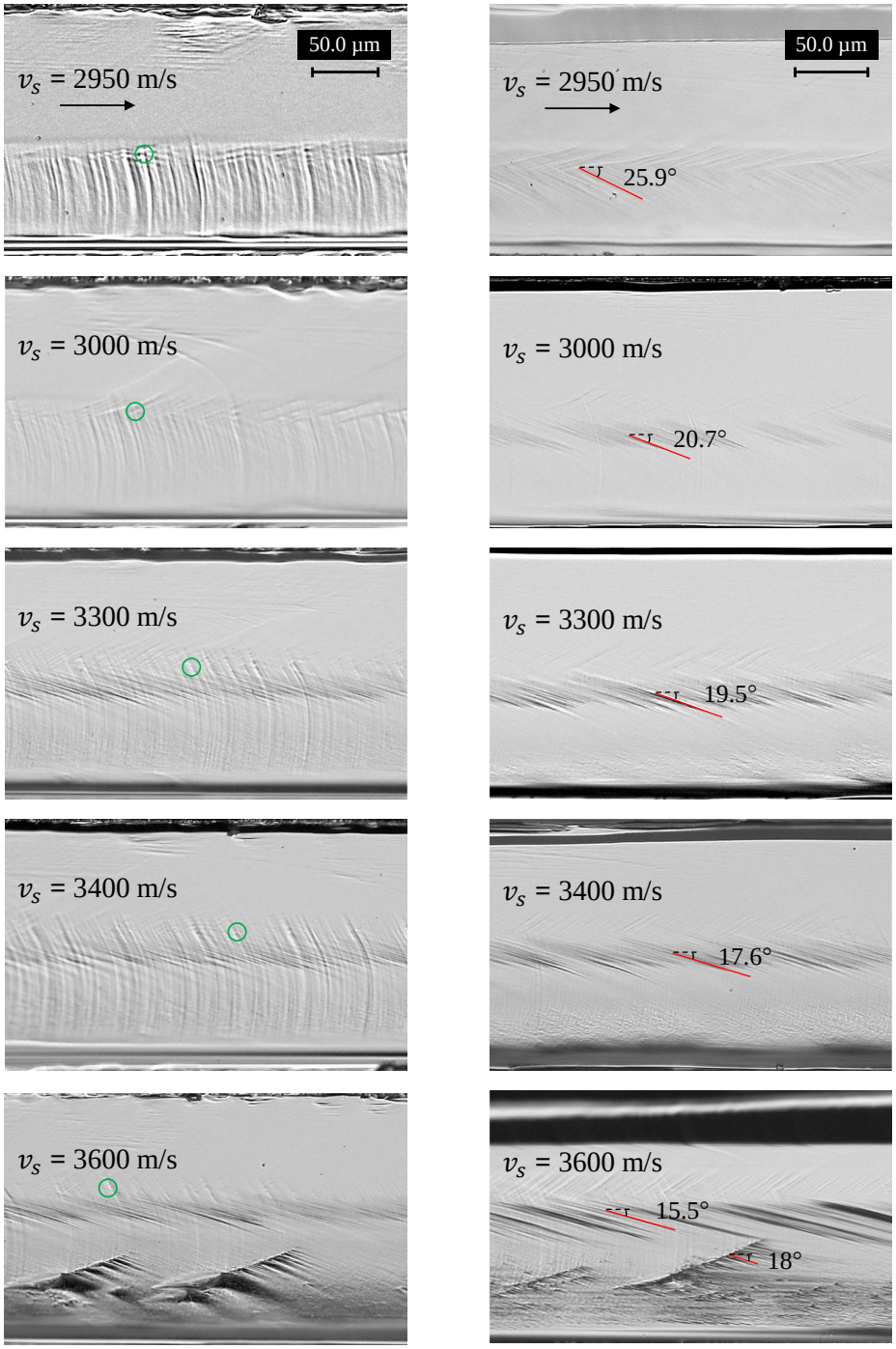

FIGURE 4.8: Comparison of the surface corrugations between the as-sawn silicon specimens (left) and surface polished silicon specimens (right), at the steady-state crack propagation velocity of 2950 m/s, 3000 m/s, 3300 m/s, 3400 m/s and 3600 m/s. The tilt angle corresponding to the maximum amplitude of the corrugation traces is highlighted by the red line.

4.3 Topography of surface corrugations

Following fracture surface observations through the optical microscope, 3D topographies of fracture surfaces of polished silicon sample were measured with AFM (Bruker Dimension 3100 Nanoscope V with AFM probes Nanosensors PPP-NCH working at tapping mode), in order to study these surface corrugations, including their nucleation and dynamic behavior. The out-of-plane resolution of the measurement is in the order of 0.1 nm. The measurements were carried out in a square field of 1024 x 1024 pixels, hence the in-plane resolutions are in the order of 5 nm, 10 nm and 20 nm for the image sizes of 5 x 5 μm, 10 x 10 μm and 20 x 20 μm, respectively. Each direction is scanned back and forth to ensure that there is no bias due to the scanning direction and the speed of AFM tips. The analysis of AFM measurements were performed through the Gwyddion software [NEČ 12].

Nanoscale topography is constructed from the fracture surface of polished sample (without Wallner lines), as presented in Fig. 4.9(a). The fracture surface at v_s = 2760 m/s ($0.62c_R$) presents the mirror fracture surface without surface corrugations, and fracture surface at $v_s = 0.74c_R$ presents substantial surface corrugations. Fig. 4.9(b) shows five typical topographies at different heights. At y = 0.6h, where the corrugation traces have not emerged yet, the fracture surface is smooth but not perfectly plat, since sub-nano instabilities pointing to the upper side of the crack front can be observed. They are considered as local crack debonding instabilities. At about y = 0.51h $\pm$ 0.03h, the corrugation traces nucleate from angstroms undulation amplitude (see Fig. 4.9(b) , y = 0.51h) and gradually grow to the maximum amplitude of few hundreds of nanometers (see Fig. 4.9(b) , y = 0.42h). Then, they rapidly decay at the height of about 0.39h (see Fig. 4.9(b) , y = 0.39h). It can be seen that sparser corrugation traces decay to the denser ones and then continue extending with the undulation amplitude of about 10 nm, shown in Fig. 4.9(b) , y = 0.35h). Although the width of corrugation traces decreases upon decay, no gap between these traces are observed. The lower portion of the fracture surface are dominated by the periodic corrugation traces.

Particularly, Fig. 4.10 highlights the occurrence of micro-branching instabilities [SHA 02, SHA 96a] at high v_s , which perform as the daughter cracks branching into the material. In this region, previous corrugation markings collapse and new single or multiple corrugation markings arise along the micro-branching lines. The single corrugation markings manifest as solitary entities on the fracture surface.

Fig. 4.11 shows seven profiles of the surface corrugations measured along the [1-10] direction in Fig. 4.9(b). The surface corrugations are found to exhibit wave-like feature in the crack propagation direction. The corrugation traces present similar shape between the ones extend to the middle of the fracture surface and the ones generated by micro-branches. Localized and well-defined structures of surface corrugations indicate that they are generated by a out-of-plane propagating motion of the crack front. Otherwise, the out-of-plane shape will strongly depend on the position along the fracture surface, like the Wallner lines, as it will be shown later in section 4.4. Besides, it is noteworthy that sparser surface corrugations exhibit larger amplitude.

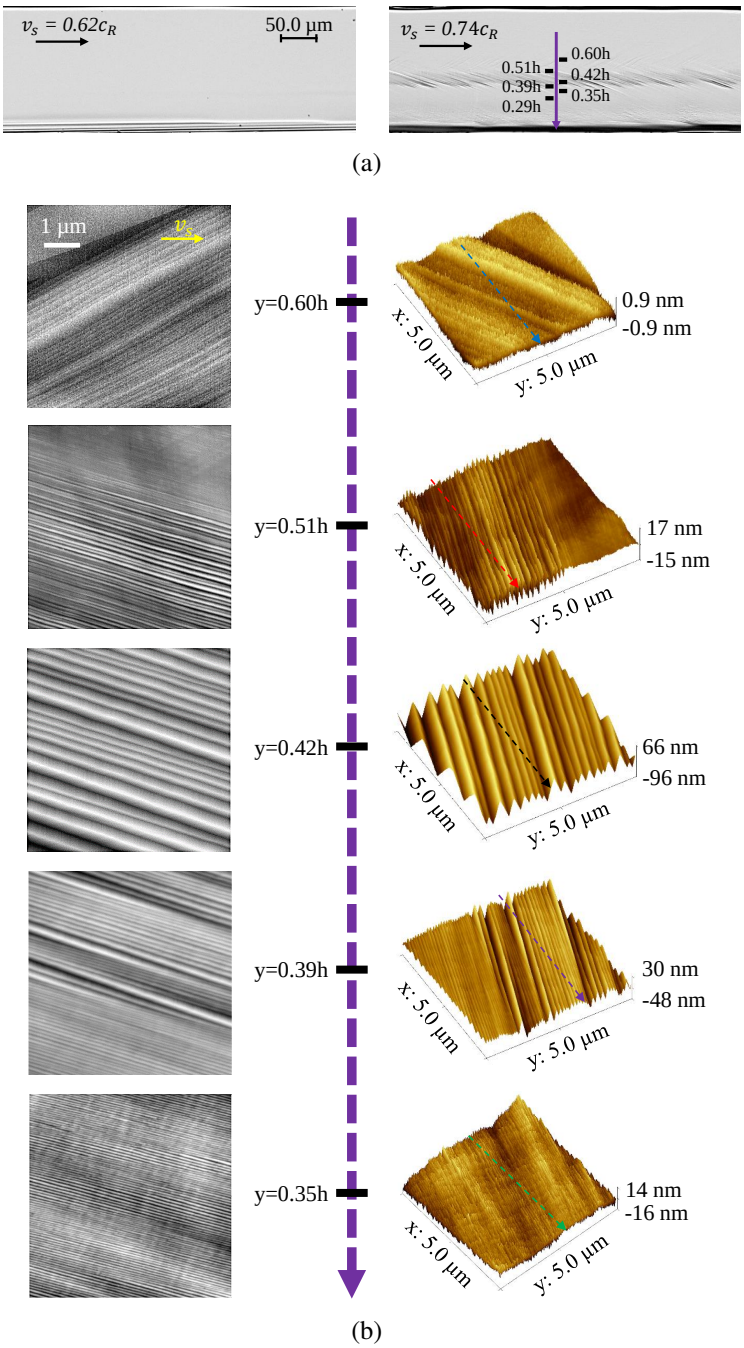

FIGURE 4.9: Fracture surface corrugation in polished single crystalline silicon wafers. (a), Mirror-like fracture surface at $v_{cw} = 0.62c_R$ and surface corrugations at $v_{cw} = 0.74c_R$. (b), A sequence of AFM measurements of the fracture surface corrugations at $v_{cw} = 0.74c_R$ along the vertical direction. The corresponding positions on the fracture surface are highlighted by black marks in (a).

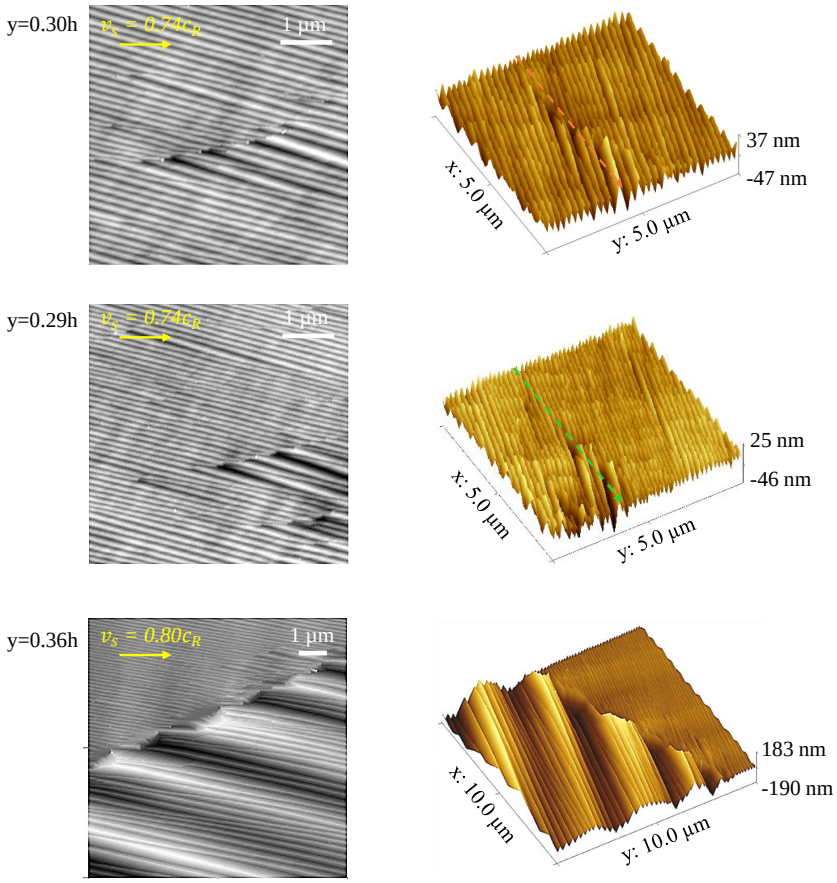

FIGURE 4.10: AFM measurements of the fracture surface corrugations at $v_s = 0.74c_R$ and $0.80c_R$ generated by the crack microbranching instabilities.

4.3.1 Amplitude evolution of surface corrugations

In order to study the amplitude evolution of corrugation traces relative to the extending distance r , the variation of the surface corrugation amplitude was analysed via the roughness R_q (root mean square) variation within a zone of 20 x 1 μm^2 parallel to the surface corrugation traces, as shown in Fig. 4.12, as it's difficult to track the amplitude evolution of a single corrugation trace. The topographies of surface corrugations with a dimension of 20 x 20 μm^2 are shown in Fig. 4.12(a). The roughness profile was obtained along a short edge while the variation was assessed along the long edge of the rectangular zone in Fig. 4.12(a). The R_q as a function of the extending distance r are presented in Fig. 4.12(b).

The occurrence and the growth of the surface corrugations are shown in the blue rectangular in Fig. 4.12(a) and $R_q(r)$ is presented by the blue marks in Fig. 4.12(b). The corrugations emerge from the fracture surface with R_q of about 1 nm which corresponds to the height of crack debonding instabilities (see Fig. 4.9(b), y = 0.6h) and then reach to the maximum amplitude, where the corrugation traces involves a R_q of about 30 nm, as shown by the red marks. The purple rectangular highlights the decay zone of surface cor-

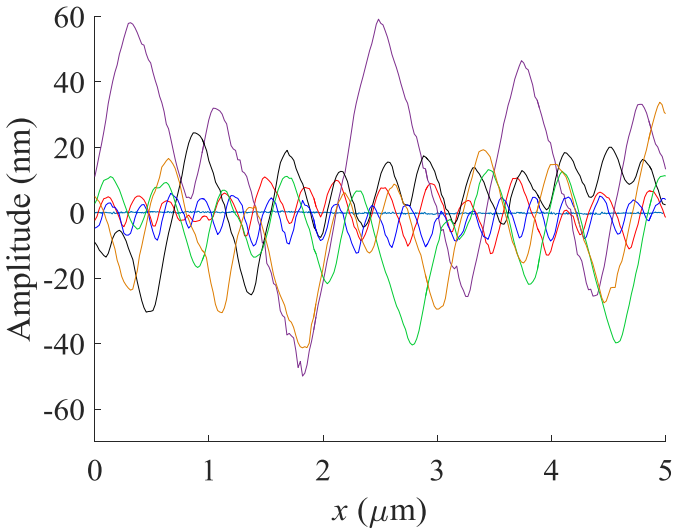

FIGURE 4.11: Profiles of the surface corrugations along the x direction at different heights via AFM measurements. The profiles are measured along the dashed arrows as presented in Figs. 4.9(b) and 4.10 with the corresponding colors.

rugations, where the corrugation traces decay in a complicated manner : upon interaction between the sparser traces located at the upper side and the denser traces located at the lower side, the sparser traces rapidly decay in both amplitude and width till the stabilized propagation as the denser traces, which present a R_q of about 3 nm. This complicated interaction reflects the nonlinear character of surface corrugations and will be discussed in section 5.4. The corrugations finally stably extending til the bottom of the fracture surface with little loss of amplitude. Moreover, when new surface corrugations generated by microbranches occur, R_q eventually increases as highlighted by the green arrow and the insert figure of local surface morphology in Fig. 4.12(b). Note that the amplitude of corrugation traces generated by microbranches attain maximum amplitude upon emergence, which differs from that generated from the local kink of the crack front.

4.4 Comparison between the corrugation traces and the Wallner lines

In this section, we show the differences between the corrugation traces and the Wallner lines via the undulation profile on the fracture surface, the amplitude evolution, as well as the generation mechanism.

Firstly, it has been shown in the previous chapter that the Wallner lines are generated by the interaction between the moving crack front and shear waves induced by an external perturbation which can be surface defects, ultrasonic traducer, and even the sudden release of concentrated stress. Since the propagation of the crack front and the shear waves are independent, the shape of the Wallner lines would not be well-defined, but depends on

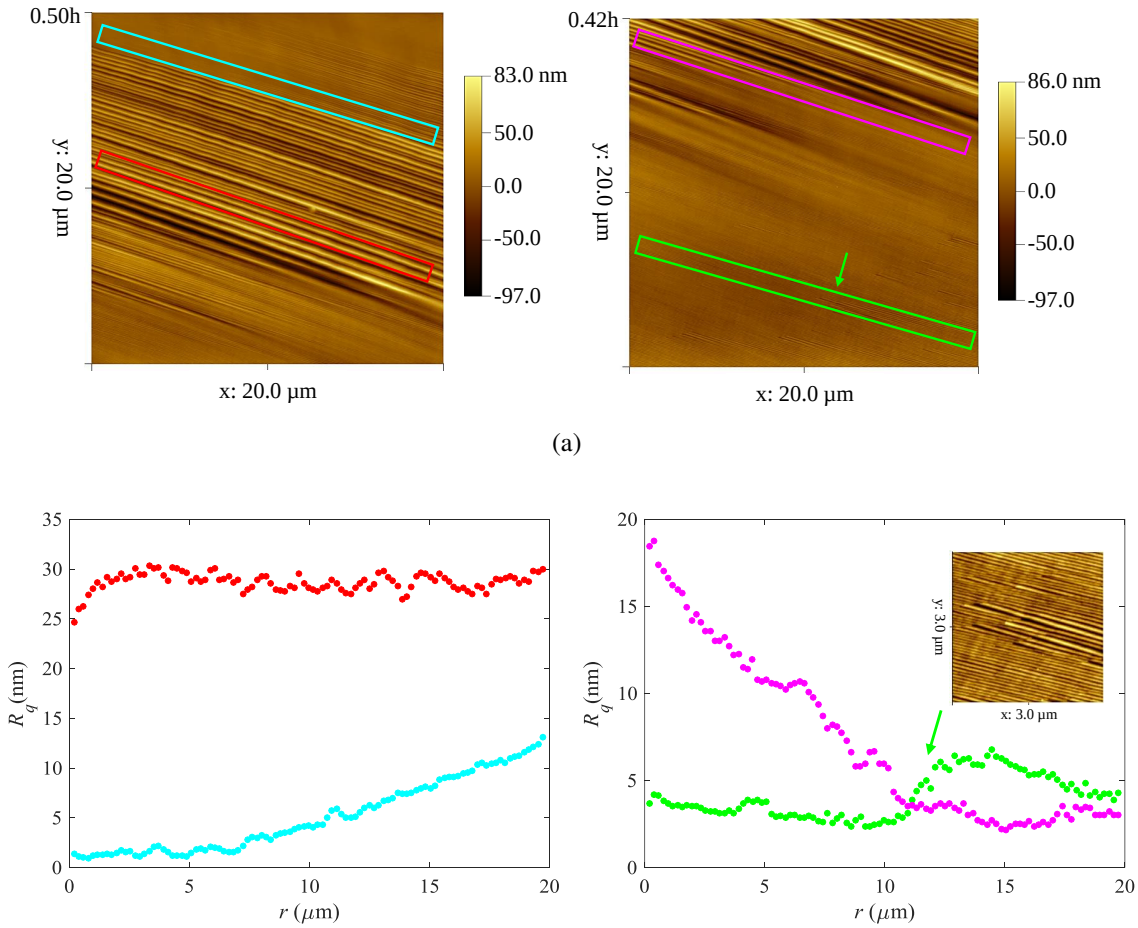

FIGURE 4.12: Roughness variation as a function of extending distance ***r*** of surface corrugations with $v_s = 0.74\, C_R$. (a), Morphology of surface corrugations within the growth zone (blue rectangular), the maximum amplitude zone (red rectangular), the decay zone (pink rectangular) as well as the persistent propagation zone (green rectangular). (b), Roughness R_q (root mean squared) as a function of r within four different zones in **a** and **c**, presented with corresponding colors. Local increase of amplitude when microbranches occur is highlighted by the green arrow and the insert figure of local surface morphology.

the crack front behavior and the origin of the shear waves. For instance, Figs. 4.13(a) and 4.13(b) show the undulation profiles of the primary Wallner lines generated from the surface defects and the profiles of the secondary Wallner lines generated from the sudden release of the contact stress. The primary Wallner lines, highlighted by the black curve in Fig. 4.13(a), present different profiles at different heights, which depends on the front-waves interaction position relative to the source of the shear waves. Besides, the geometry of the surface defects that generate the shear waves will also play a role in determining the shape of the Wallner lines, as presented in Fig. 4.13(b), since the strength of the

shear waves (amplitude, wavelength) depend on the source that creates them [FIN 03]. In contrast, it has been shown in Fig. 4.11 that the corrugation traces display well-defined wave-like shape, which is independent on both their location on the fracture surface and the source that generates them.

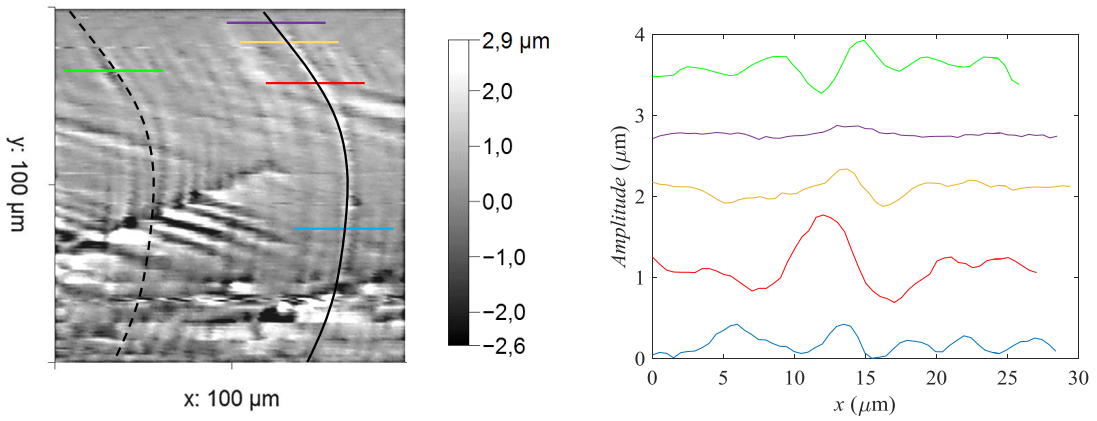

(a)

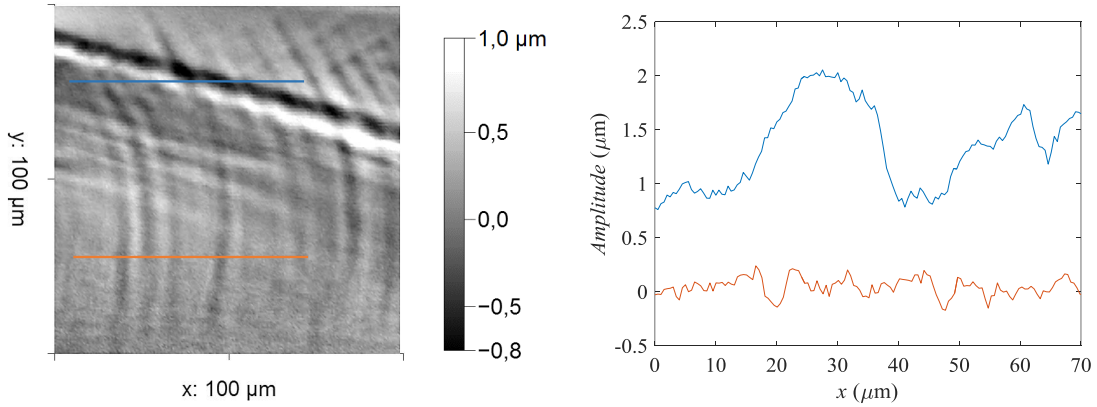

(b)

FIGURE 4.13: Profiles of the Wallner lines along the x direction measured by the laser scanning profilometry. (a), Profiles of the primary Wallner lines at different positions on the fracture surface with v_s = 3300 m/s. (b), Profiles of the primary and secondary Wallner lines in the case of v_s = 3100 m/s (red curve) and v_s = 3300 m/s (blue curve). The profile measurements are carried out along the straight lines highlighted on the topographies with the corresponding colors. Profiles have been shifted vertically for sake of clarity.

Secondly, the amplitude evolution implies a key difference between the Wallner lines and corrugations traces. As shown in Figs. 3.14, the amplitude evolution of the Wallner lines during their extension is determined by the decay of the shear waves, which obeys the $1/r^2$ decay. The amplitude of corrugation traces presents rather a complicated decay manner than a continuous decay and stabilizes at the nanoscale. The corrugation traces finally extend for large distances with nearly constant amplitude, as shown in Fig. 4.12.

Moreover, upon the occurrence of microbranches, if shear waves burst, they would radially spread from the source spot, and the interaction of the diffusive waves with the crack front would generate a pair of Wallner lines extending to opposite directions relative to the wave source. However, regarding the microbranch-induced corrugation traces, they extend solely along one direction. This confirms that they are generated by localized waves along crack front emitted from the microbranching event.

As mentioned in section 3.2, the crack front waves are generated when the moving crack front encounters the local heterogeneity of fracture energy, such as material inhomogeneities (asperities). Both the wavelength and the amplitude of the front waves are set by the dimension of the original pertubation [SHA 01, FEK 20]. However, our solar grade silicon specimens have a high purity which is in the order of 99.9999% [ZHA 16a]. Even though the specimens are doped with boron atoms, which are distributed in the silicon crystal lattice by replacing the silicon atoms. The doping atoms are not supposed to trigger front waves as they are too discrete, local and small to be able to impact the fracture energy during the crack propagation. However, the doping atoms may generate debonding instabilities which do not present wave-like shape [KER 13], as shown in Fig. 1.15(c) in Chapter 1.

Given the distinguished properties compared to the Wallner lines, i.e., the corrugations traces present a well defined shape, a localized character and a long lifetime (which extend over four decades and keep an nearly invariant shape with an amplitude of one decade), we may conclude that the corrugation markings are generated by a propagating mode of the crack front. We also name them corrugation waves since they incorporate periodic out-of-plane component. We conjecture that the corrugation waves are generated by the intrinsic fracture toughness jump or the crack micro-branching instabilities, as highlighted in Figs. 4.5, 4.6 and 4.10. Indeed, the inherent fracture energy jump can be analogous to a virtual material asperity perturbing the material fracture energy balance at the crack front. The corrugation waves are not the front waves but shares certain soliton-like characteristics with the crack front waves [WIL 97, ADD 13, SHA 01, SHA 02]. The nonlinear attributes of the corrugation waves will be shown in the next section.

5 Corrugation waves

According to the analytical and numerical works [RAM 97b, MOR 98, MOR 00, WIL 97, ADD 13], crack front waves persistently propagate along the crack front at a speed slightly lower than the Rayleigh waves speed. First experimental investigation of front waves involved intentional material asperities [SHA 01], where front waves have been shown to present solitary wave characters, which have not been demonstrated by numerical works. In the present work, we will enrich the characteristics of the nonlinear propagating mode of the crack front through unveiling nonlinear attributes as well as nonlinear interaction behavior of the corrugation waves.

5.1 Extracting front wave shapes from surface corrugations

Fig. 4.14(a) schematically illustrates the formation scenario of surface corrugations. Corrugation waves of amplitude A_{cw} and wavelength λ_{cw} are localized along the crack front, propagate at v_{cw}, twist the crack front (red curve) moving at v_s along x direction and leave surface corrugations orientated with an angle α relative to v_s. Hence, the profile of the corrugation traces along the crack front provides the shape of the corrugation waves (λ_{cw} and A_{cw}). The crack front shape was reconstructed from the retroactive decomposition (see section 2.2.2 of Chapter 3) of Wallner lines generated from the surface defects that were not completely eliminated, as shown in Fig. 4.14(b). The crack front shape was superposed with the surface corrugations according to the coordinate along the y direction.

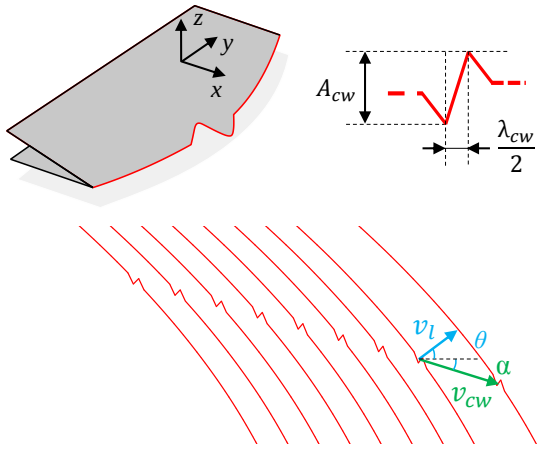

(a)

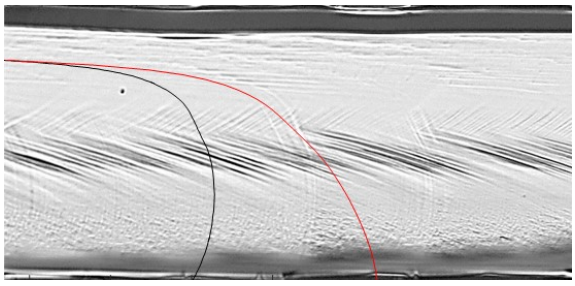

(b)

FIGURE 4.14: (a), Formation mechanism of surface corrugation. (b), Fracture surface morphologies of surface-polished sample. The crack front shape (red curve) is reconstructed from the Wallner lines (black curves) generated from uneliminated surface defects.

Moreover, the propagation speed of the corrugation waves v_{cw} can be calculated from the relation between the orientation of the surface traces α, the local crack velocity v_l and its direction θ, given by $v_{cw} = v_l/\cos(\alpha+\theta)$, and the frequency of the corrugation waves ω_{cw} can be determined with their shape and speed, given by $\omega_{cw} = 2\pi\, v_{cw}\, /\lambda_{cw}$. Obviously,

at a given height of the crack front, where v_l and θ are constant, α increases when v_{cw} increases.

5.2 Linear correlation between the amplitude and the wavelength

Figs. 4.15 present the AFM measurements of the corrugation traces at different v_s and y positions. Firstly, the AFM measurements show that sparser corrugation traces exhibit larger amplitude. The shapes of the corrugation waves are extracted from the AFM measurements along the crack front, where the wavelength λ_{cw} is defined as twice the distance between the peak and the valley of corrugation waves. The wave shapes extracted from the AFM measurements for three steady-state crack propagation with $v_s = 0.68c_R$, $0.74c_R$ and $0.80c_R$ are presented on the right side of Fig. 4.16. The corrugation waves are found to involve a linear correlation between the wave amplitude A_{cw} and the wavelength λ_{cw} for each v_s case. Interestingly,, a scale-independent characteristic profile has been obtained, as shown on the left side of Figs. 4.16. The unique characteristic profile was obtained by normalization over λ_{cw} and A_{cw} of the measured shapes. For each shape, the wave amplitude A_{cw} was normalized to ± 0.5 and the half-wavelength $\lambda_{cw}/2$ was normalized to 0.5, i.e., the peak and the valley of the normalized shape stand on 0.25 and 0.75, respectively.

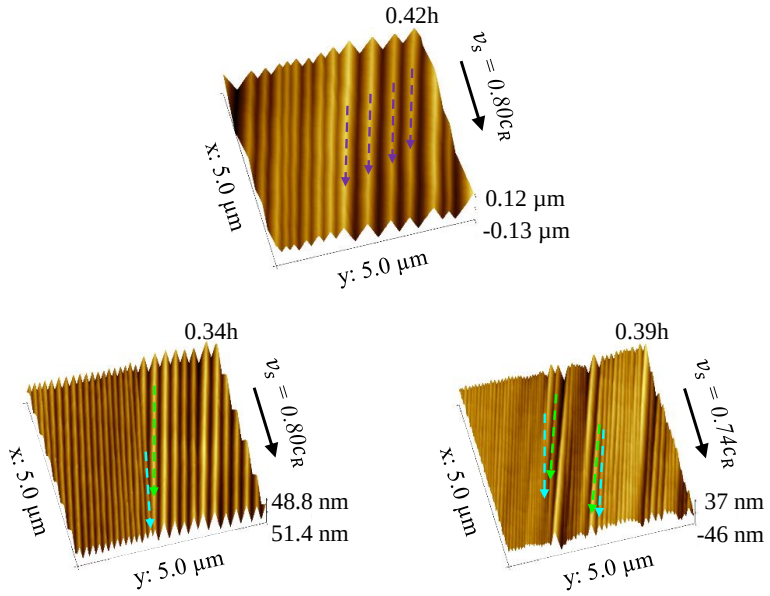

FIGURE 4.15: Three AFM measurements of corrugation traces at different v_s and y positions.

It is noteworthy that the characteristic profile is independent on the lattice structure of silicon crystal, given that the corrugation waves travel on the (110) plane along various directions. The correlation between A_{cw} and λ_{cw} reveals an intrinsic nonlinear feature of the corrugation waves. This is well distinguished from linear elastic waves, for which the wavelength is independent of the amplitude. The unique characteristic profile of the

corrugation waves coincides well with the soliton-like character of front waves reported in[SHA 01].

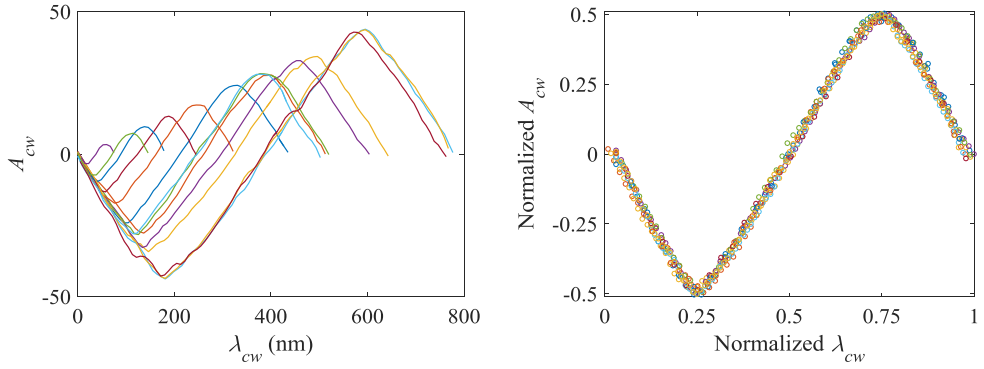

(a)

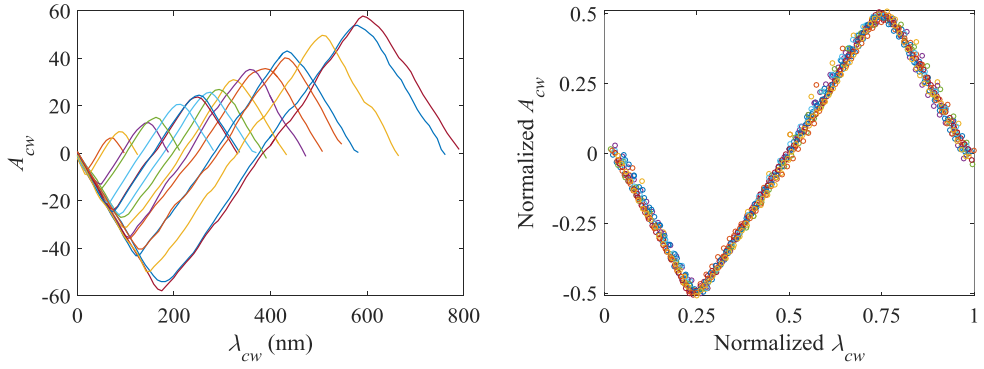

(b)

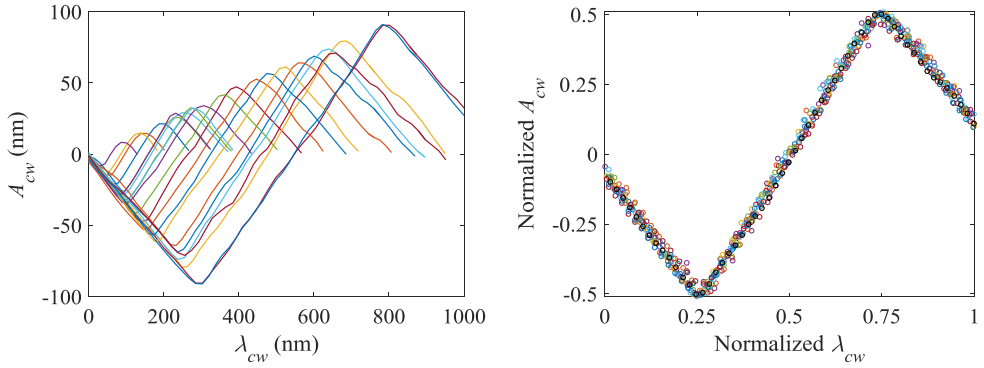

(c)

FIGURE 4.16: Corrugation waves shape in three steady-state cases with v_s = (a) $0.68c_R$, (b) $0.74c_R$ and (c) $0.80c_R$. The original wave shapes are shown on the left and the normalized wave shapes are shown on the right.

Furthermore, it is found that the linear relationship the corrugation waves amplitude

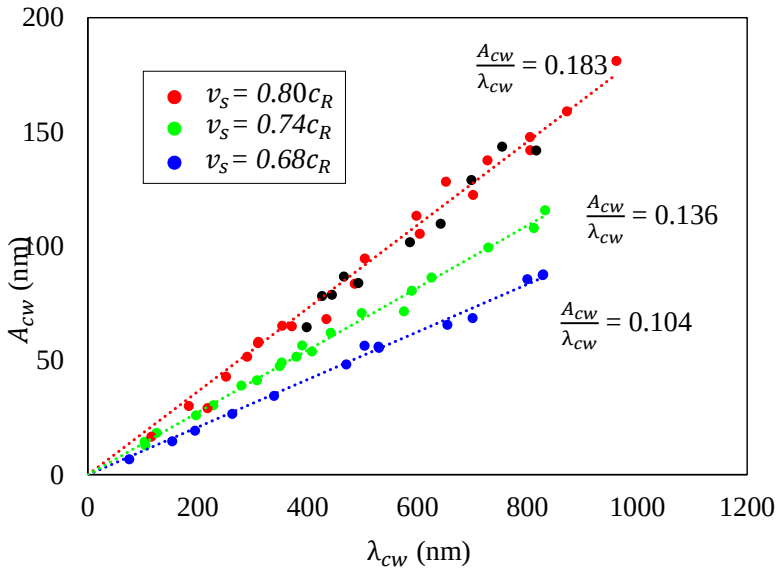

FIGURE 4.17: Linear relationship between the amplitude A_{cw} and the wavelength λ_{cw} of corrugation waves extracted from the AFM measurement along the crack front for v_s = $0.68c_R$, $0.74c_R$ and $0.80c_R$. Linear regressions are highlighted by the blue, green and red dashed line presenting a proportionality coefficient of 0.104, 0.136 and 0.183. The black points correspond to then corrugation wave shapes during the collision phenomenon with $v_s = 0.80c_R$ presented in section 5.4 (Fig. 4.19(b)).

and the wavelength varies at different steady-state crack propagation velocities, as shown in Fig. 4.17 incorporating $0.68c_R$, $0.74c_R$ and $0.80c_R$. Noting that the linear regression coefficient A_{cw}/λ_{cw} increases when v_s increases, hence for the corrugation waves with the same λ_{cw}, A_{cw} increases when v_s increases. This may explain why the surface corrugations are more remarkable at higher v_s shown in Fig. 4.8.

5.3 Nonlinear dispersion relation

Furthermore, we find that the orientation of the corrugation traces α changes with the corrugation wavelength λ_{cw}. As presented in Fig. 4.15, the purple dashed arrows in the top inset highlight that the corrugation traces with nearly identical width present the same orientation α. Green and blue dashed arrows in bottom insets highlight the difference of the orientation α for corrugation traces with different widths. It can be seen that the sparse corrugation traces exhibit a larger tilt angle than the dense ones. In the light of the formation mechanism of the surface corrugations, the propagation speed of the corrugation waves v_{cw} can be calculated based on the orientation of the corrugation traces α, the local crack velocity v_l and its direction θ, through $v_{cw} = v_l/\cos(\alpha+\theta)$. At a given height of the crack front, where v_l and θ are constant, the dependency of α on λ_{cw} reveals that v_{cw} depends on λ_{cw}.

The variation of the corrugation wave speed versus the wavelength λ_{cw} is shown

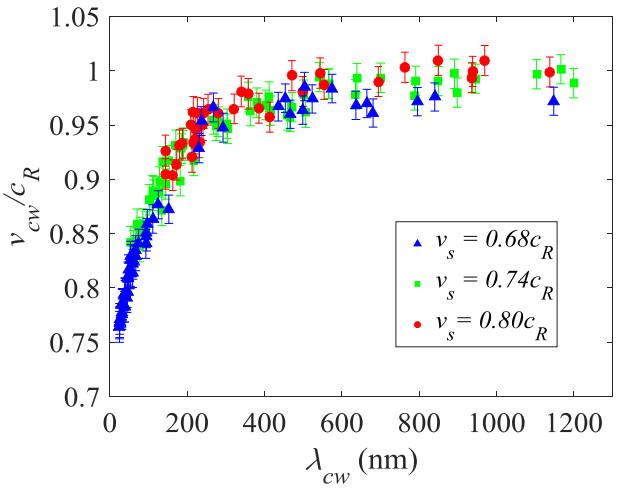

(a)

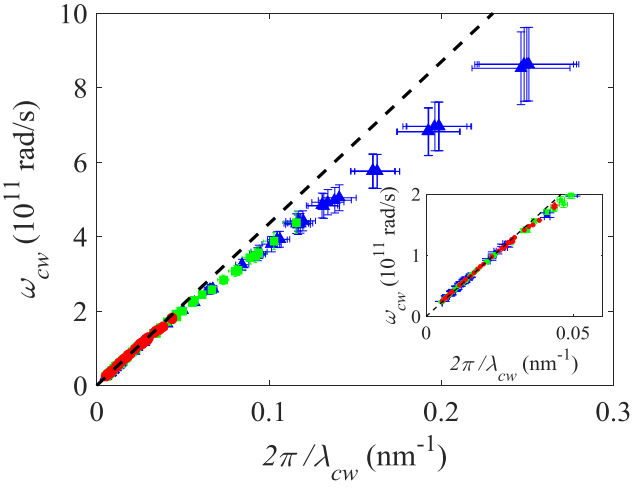

(b)

FIGURE 4.18: Dispersion of the corrugation waves. (a), The normalized corrugation waves speed v_{cw}/c_R is given as a function of the wavelength λ_{cw}. (b), The dispersion relation of corrugation waves between the frequency ω_{cw} and the wavenumber $2\pi/\lambda_{cw}$. The linear relation for $\omega_{cw} < 1.2 \times 10^{11}$ rad/s (the inset) is highlighted by the dashed line. The error bars on v_{cw} are due to camera uncertainties on v_s and the error bars on ω_{cw} are due to the AFM measurement precision on λ_{cw}.

in Fig. 4.18(a). For $\lambda_{cw} >$ about 235 nm, v_{cw} is approximately equal to the Rayleigh wave speed, which agrees well with the predicted propagation speed of the front waves [RAM 97b, MOR 98, SHA 01]. However, for $\lambda_{cw} <$ about 235 nm, v_{cw} decreases significantly when λ_{cw} decreases. Fig. 4.18(b) highlights the dispersion relation (relationship between the frequency ω_{cw} and the wavenumber $2\pi/\lambda_{cw}$) of the corrugation waves). The frequency is calculated by $\omega_{cw} = 2\pi v_{cw}/\lambda_{cw}$, hence the slope of the dispersion relation corresponds the wave speed v_{cw}. It can be seen that the dispersion relation is linear for $\omega_{cw} <$ about 1.2×10^{11} rad/s as highlighted in the inset of Fig. 4.18(a) by the black dashed line, while it becomes nonlinear at around $\omega_{cw} = 1.2 \times 10^{11}$ rad/s.

5.4 Particle-like collision

Additionally, we bring to light another nonlinear characteristic of the corrugation waves, which concerns particle-like interaction behavior. As can be appreciated in Fig. 4.19(a), the AFM measurements of fracture surface at $v_s = 0.80\ c_R$ show the corrugation traces (highlighted by the blue and green dashed lines) generated by the interaction of two corrugation waves. Five sequences of shape evolution of the corrugation waves during the collision are presented in Fig. 4.19(b). When fast waves (long λ_{cw}, $v_{cw} = 0.965 c_R$) meet slow waves (short λ_{cw}, $v_{cw} = 0.935 c_R$), unlike the linear elastic waves which display simple linear superposition, they exhibit nonlinear collision : the fast waves decay and decelerate while the slow waves grow and accelerate. It is noteworthy that the linear correlation between λ_{cw} and A_{cw} remains unchanged during the collision, as highlighted by the black points, corresponding to ten shape variations, in Fig. 4.17. As a result, both the shape and speed of the corrugation waves exchange and an orientation shift of corrugation traces occurs after the collision. Since the nonlinear dispersion is more significant for corrugations waves with shorter λ_{cw}, the collision events are more frequent in regions traveled by the denser corrugation waves, in which successive collisions between the corrugation waves can be observed, as shown in Fig. 4.20. This behavior is therefore different from linear elastic waves, but similar to soliton collision during which fast pulse decays and slow pulse advances resulting in a discontinuous jump and a phase shift [SHA 01, ECK 98, BEN 06, ANC 11, VER 19].

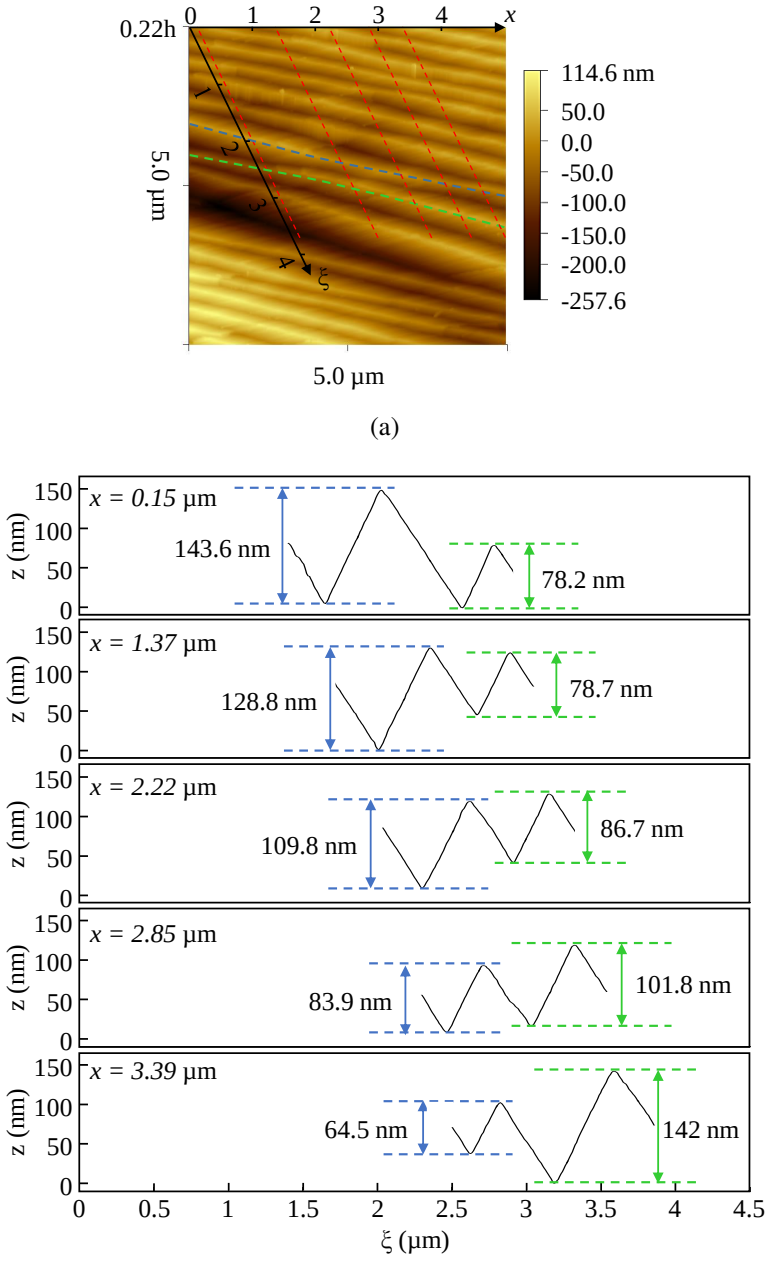

FIGURE 4.19: (a) Close-up AFM measurements of surface corrugations at $v_s = 0.80\ c_R$, where the ξ axis is the tangent direction of the crack front. The collision of two corrugation waves is highlighted by the blue and green dashed lines. The corrugation traces exchange their orientation α after the collision. (b), Sequences of shape evolution of the corrugation waves during the collision (in (a)). The five sequences are highlighted in (a) by the red dashed line varying along the x direction.

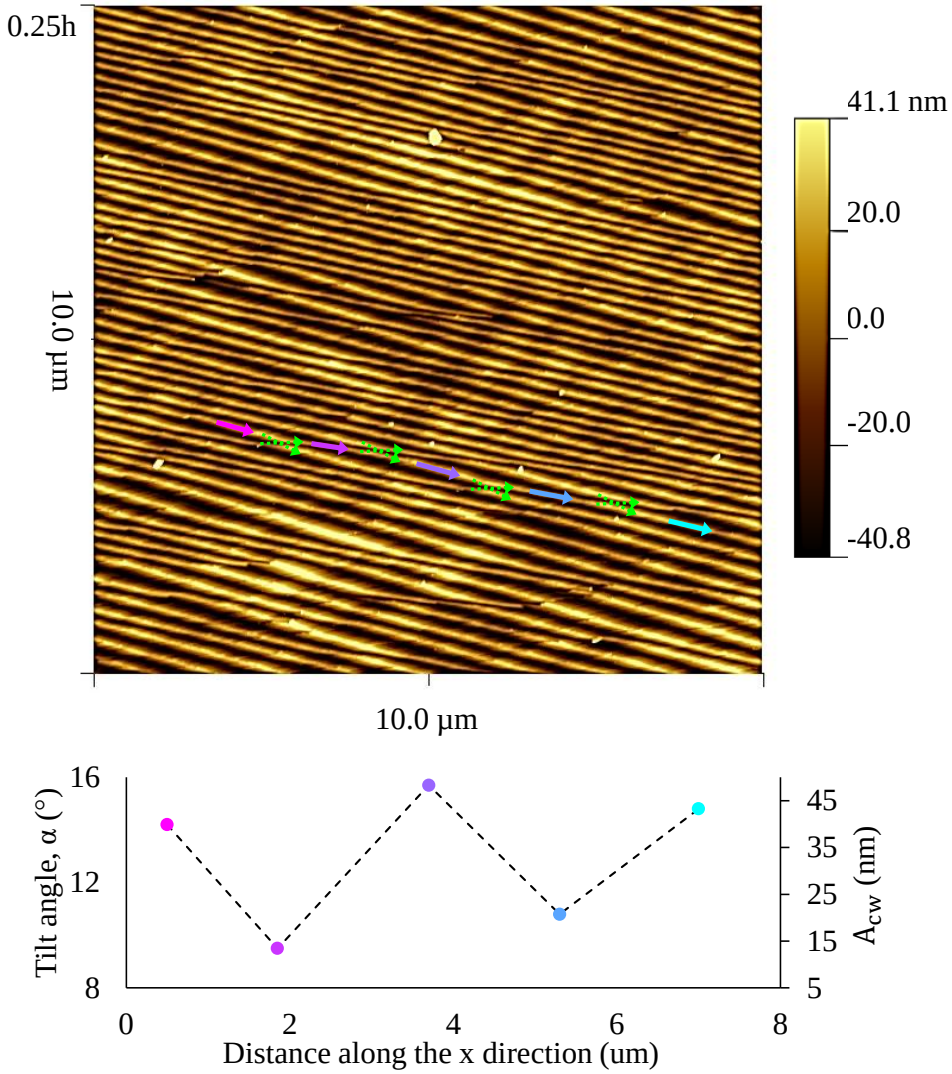

FIGURE 4.20: Topographies of the surface corrugations (top insert) at $v_s = 0.74\ c_R$ incorporating successive collisions that result in successive phase shifts, as highlighted by the green dashed arrows, and simultaneous variation of α and A_{cw} of the corrugation marking (bottom insert) generated by successive collisions of corrugation waves, measured from the arrows with the corresponding colors.

6 Discussion

LEFM describes the dynamic of the crack front governed by the local energy balance at each point of the front. The local fracture toughness jump reported here is supposed to induce only an in-plane fluctuation of local crack velocity and consequently alter the planar crack front dynamics. Nevertheless, it breaks down the translational invariance of the moving front and induces the abnormal gradient of the energy flux dG_l/dz at the

front kink site. Besides, the crack micro-branches that cause v_l oscillations and Γ_l jumps [SHA 02, FIN 91, SHA 96a] also produce the corrugation waves.

As suggested by theoretical predictions and experimental observations, the abnormal $d\mathcal{G}_l/dy$ fulfills the nucleation condition of the front waves [RAM 97b, MOR 98, MOR 00, SHA 02, FIN 03]. Therefore, we suggest that the corrugation waves share the necessary generation condition with the front waves, i.e., local fracture toughness heterogeneities ahead of the crack front. Meanwhile, we conjecture that, like the out-of-plane corrugations [ADD 13] and the front waves [WIL 97], any slight out-of-plane perturbation (for instance the debonding instabilities, see Fig. 4.9) could trigger the out-of-plane component of the corrugation waves that sprouts from the atomic scale. Note here that the corrugated topographies on the opposing fracture surface involve peak-to-valley match. This can be distinguished from the other nanoscale corrugations of the fracture surface, which present peak-to-peak match, generated by the local plasticity ahead of the crack tip [WAN 07, SIN 16].

The corrugation waves deform the crack front and lead to an increase of the fracture surface. They create extra energy dissipations and hence can propagate only in the region when $\mathcal{G}_l > 2\gamma$. On the upper side of the nucleation site of the corrugation waves, $\mathcal{G}_l = 2\gamma$ (see Fig. 4.3(b)). Therefore, no additional energy can support the corrugation waves to extend to the upper side. This explains why the corrugation waves extend solely to the lower side where $\mathcal{G}_l > 2\gamma$.

The most distinguishable feature of the corrugation waves reported here is that they are continuously self-emitted from the moving crack front, sprouting from atomic-scale amplitude, continuously growing to the submicron amplitude and propagating in a soliton-manner with long lifetime. Hence, periodic corrugation traces are created and cover the whole fracture surface. The continuous nucleation of corrugation waves in response to intrinsic fracture toughness jump could be analogous to the consequence of a crack front traveling through substantial heterogeneities, which continually twist the crack front [MOR 00, PER 94, RIC 94] and lead to periodic fracture surface markings. In addition to the intrinsic fracture energy jump that triggers the corrugation waves, we show that the microbranches locally disturbing the fracture energy can also produce the corrugation waves. This pheonomon is similar to the occurence of the front waves reported in [SHA 01, SHA 02, LIV 05]. The initial state of the corrugation waves depends on the source that creates them. The growth of corrugation waves at the front kink zone could be explained by the continuous increase in the fracture energy (see Fig. 4.3(b)), while the corrugation waves initiate with the maximum amplitude once triggered by the microbranching events (see Figs. 4.10 and 4.12), which generate an abrupt jump of the fracture energy. Furthermore, we suggest that the nonlinear dispersion relation could be a result of the frequency-dependent phonon scattering at the moving crack front and the anisotropic elasticity of silicon single crystal [ADD 13, WIL 01, NOR 07].

The unique characteristic profile of the crack front waves has been previously reported in [SHA 01], in which it was obtained through scaling the front waves in steady-state motion (after the exponential decay) by the initial pulse width (defined as the distance between the first minimum and first maximum of the fracture surface amplitudes). The

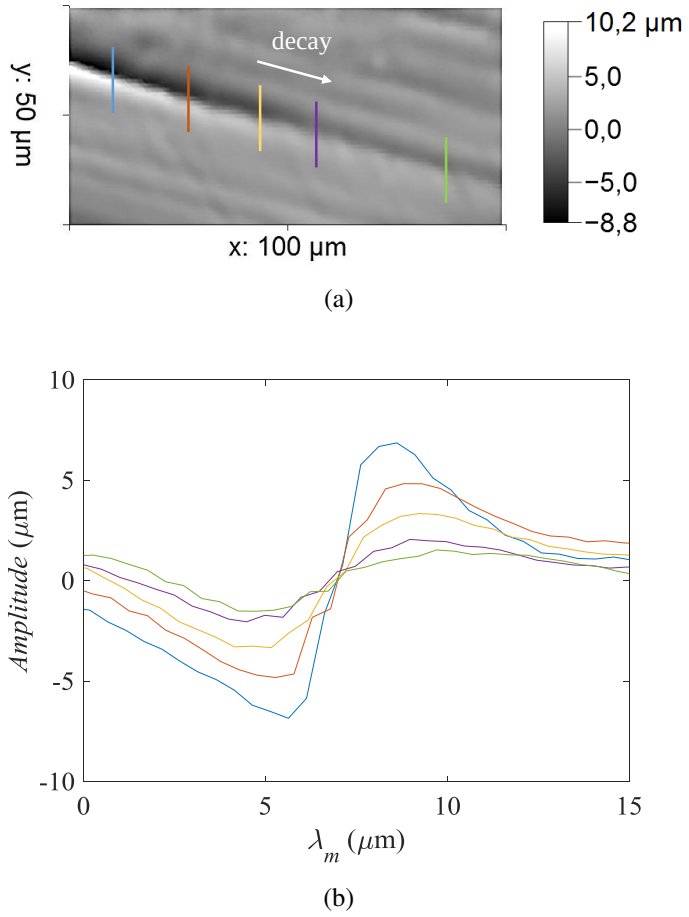

FIGURE 4.21: (a) Profilometer measurement of the secondary Wallner line at $v_s = 0.74$ c_R of as-sawn sample in three-line bending tests, and (b) evolution of surface undulations along the Wallner line at different position. Sketch of the Wallner lines generation at five successive time steps is shown in inset. The crack front and wave front are presented by the full lines and dashed lines, respectively.

authors propose that this behavior, which could be analogous to the classical soliton formation, may be the consequence of the compensation between the dispersion and nonlinear effects in the wave process [LOM 99, REM 13]. In our work, regardless of the corrugation wave motion, the characteristic profile is obtained thanks to the linear relationship between the wave amplitude and the wavelength, which reveal that the corrugation waves is scale-independent. Meanwhile, it has been shown that the linear relationship depends on the crack steady-state velocity, which determines the initial state of the corrugation waves.

The correlation between amplitude and wavelength of the corrugation waves is different from the linear elastic waves. For example, Fig. 4.21 presents the profilometer measurement of a secondary Wallner line in the as-sawn sample generated by the interaction between the linear elastic waves and the crack front. The surface undulations

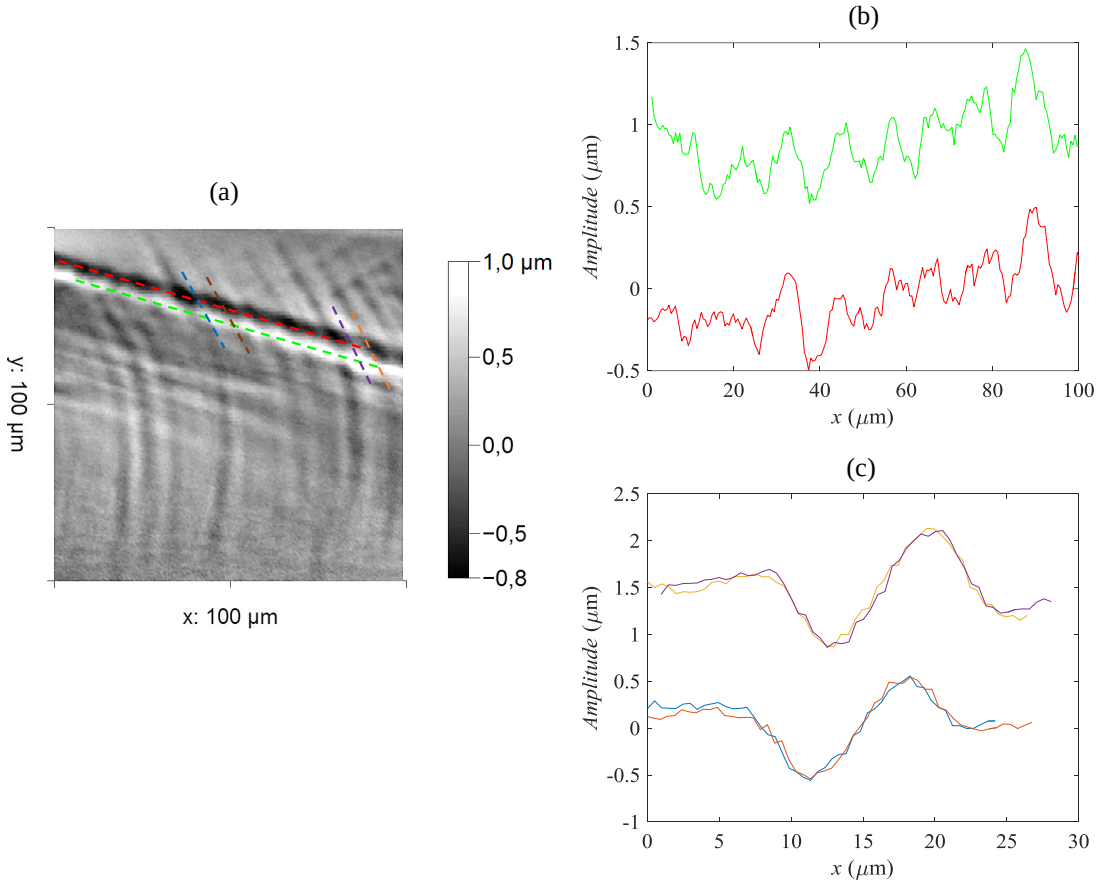

FIGURE 4.22: (a), Profilometer measurement of the interaction between the primary and secondary Wallner lines at v_s = 0.69 c_R of as-sawn sample in three-line bending tests. (b), Profile undulations along the peak (green) and valley (red) of the secondary Wallner line. (c) Profile undulations along the peak (green) and valley (red) of the primary Wallner lines. The measurement positions are highlighted by the dashed lines in (a) with corresponding colors.

measured along the vertical direction at five different positions along the Wallner line are shown in Figs. 4.21(b). It can be noticed that the undulation amplitude decreases when the Wallner line extends, while the width of Wallner line, λ_m, remains invariant, indicating the independence on the undulation amplitude. Furthermore, we characterize the fracture surfaces at small scale involving the Wallner lines and the corrugation traces by the 1D height-height correlation function. The fracture surfaces were found to exhibit an isotropic self-affinity with a roughness exponent $\zeta = 0.79$ and $\zeta = 0.95 \pm 0.03$ for the surface with the Wallner lines and with corrugation traces, respectively. The detail can be found in Appendix A.

We experimentally demonstrate, for the first time, the nonlinear dispersion of the corrugation waves when the wave frequency is higher than about 0.12×10^{11} rad/s. Below this value, the corrugation waves respect the linear dispersion relation. We suggest that the

nonlinear dispersion relation could be a result of the frequency dependent phonon scattering at the moving crack front and the anisotropic elastic modulus of silicon. Moreover, thanks to the different speeds of corrugation waves, their interactions can be observed. The collision phenomenon reported in our work is the most important evidence of the nonlinear character of the corrugation waves. In the case of linear elastic waves, the waves are expected to cross each other through simple linear superposition upon interaction. Indeed, Fig. 4.22 show the profilometer measurement of the fracture surface region incorporating the interactions between the primary and secondary Wallner lines. The superposition between them are observed. Two profiles of the surface undulations measured along the peak (green dotted line) and valley (red dotted line) of the secondary Wallner line are shown in Fig. 4.22(b). The undulations of two profiles, generated by the primary Wallner lines, exhibit similar height variation. This implies the linear superposition of the primary Waller lines on the secondary Wallner lines. Besides, the same phenomenon can be observed on the the peak and valley lines of the primary Wallner line, which are generated by the linear superposition of the secondary Wallner lines, as shown in Fig. 4.22(c).

7 Conclusion

In the light of abundant fractographic analysis jointly with the crack velocity measurements, we have investigated the crack front dynamics and the special fracture surface corrugations at the high-speed crack propagation under pure bending. Based on LEFM, the sharp increase of the dynamic fracture toughness along the (110) cleavage plane, which depends on the crystallographic direction, has been revealed. We show that the crack front develops a local kink due to the local fracture energy fluctuation. Besides, we highlight the occurrence of corrugation waves (out-of-plane elastic waves) that leave special surface markings in the absence of the material asperities. We demonstrate that these waves are generated by the local fluctuation of fracture energy due to the intrinsic dynamic fracture toughness jump or the nucleation of the microbranches. Comparing with linear elastic waves (shear waves), the nonlinear characters of the corrugation waves have been brought to light. We point out that the nonlinear attributes of the corrugation waves reported here, such as the scale-independent characteristic shape, the nonlinear dispersion and the particle-like collision outline a more complete picture of the corrugation waves than what has been described for the front waves with the numerical modeling and experiments incorporating individual material asperities. Our results may give new insights on soliton-like crack front dynamics, as well as roughness formation on fracture surface of asperity-free materials.

General conclusions and prospects

Conclusions

In this thesis, we studied the dynamic crack front behavior in single crystalline silicon wafer under bending conditions, covering a large range of crack propagation speeds. We presented different crack front behavior under different local perturbations that create typical surface structures and can lead to the crack deflection. Our work was mainly based on experimental methods and auxiliary finite element simulations were carried out as well. We conducted a total of 75 three-line bending tests on as-sawn specimens, 70 four-line bending tests on as-sawn specimens and 30 four-line bending tests on surface-polished specimens, to ensure the reliability and abundant analysis on the experimental results.

In-situ observation of the high-speed propagating crack front in silicon crystal is challenging. Therefore, post-mortem fractography provides an appealing method to analyze the dynamic crack front behavior. We use a fractography-based retroactive kinetics method to determine the crack propagating velocity, the crack front shape, as well as the elastic wave speed relating to specific surface markings.

We found that the shear wave perturbations on the crack front lead to out-of-plane wave-like deformation of the crack front. The mode III load due to the shear component can eventually cause a partial crack front deviation from the original (110) plane, and hence is the main reason for the (110)-(111) crack deflection. This can explain the puzzle in [ZHA 18a] about the occurrence of (111) cleavage underneath the line-contact. Besides, we highlighted that the crack always tends to follow the lowest fracture energy plane in crystalline silicon.

We characterized crack front shape evolution with crack speed varying from $0.22c_R$ to $0.82c_R$ (c_R represents the Rayleigh wave speed) under pure bending condition, which involves gradient of elastic energy release rate. We showed that the local dynamic fracture toughness (Γ_l) is dependent on crystallographic orientations, and exhibits a jump at high crack speed (between $0.47c_R$ and $0.64c_R$ for different directions) which results in a local kink of the crack front.

Different from the previous studies in which corrugation waves were generated from material asperities [SHA 01], we showed that corrugation waves can also nucleate in asperity-free material in response to intrinsic local Γ_l jump of a bending crack front. The corrugation waves are continuously self-emitted and propagate as solitary waves along the crack front, leaving typical surface markings that dominate the corrugated fracture

surface morphology. Moreover, the corrugation waves generated from micro-branches have also been studied. We provided the quantitative characterization of these waves and highlighted the scale-independent characteristic shape, nonlinear dispersion of the corrugation waves, and their soliton-like collision behaviors. Our results confirm the existence of the corrugation waves as well as their intrinsically nonlinear attributes.

Prospects

For the fracture initiation of the as-sawn silicon wafer, both crack initiation on the (110) plane and on the (111) plane involving mode I and mode III failures are observed (see Figs. 3.3). The difference of the effective fracture energy to initiate the micro-crack reveals that the fracture stress would be different depending on the location of the micro-crack. For instance, [SEK 18] studied the effect of the saw mark direction on the fracture strength of silicon wafers under four-line bending tests. They found that the strength is lower under a loading parallel to the sawing induced crack surface compared to that under loading perpendicular to the crack surface. [WU 12] reports that the edge pre-crack oriented at an angle of 0° - 45° relative to tensile loading results in much lower fracture strength than that oriented at an angle $> 45^\circ$. Besides, based on stress intensity factor calculation using FE method, [AZA 16] found that the subsurface micro-crack oriented at 20° and 60° relative to the wafer's surface are the most and least vulnerable defects subjected to the bending loading. However, the anisotropy of the fracture toughness for different locating planes of the micro-crack was not taken into account. Hence, to improve the fracture strength of the silicon wafer via the wire sawing technique, there is a need to further understand the relationship between the sawing technique and the induced subsurface defects, including their depth, orientation, morphology, etc., then optimize the micro-crack morphology and improve the wire sawing technique.

For the crack velocity measurement, we showed that the frame rate of the high-speed camera restricts the resolution of velocity measurement. Albeit the fractographic analysis provides a more precise resolution, we do not have exact information of the crack velocity. For instance, the small velocity variation can not be captured. Hence, a velocity measurement method with finer resolution could be developed. It has been shown that a continuous variation of the crack velocity can be well measured by the potential drop method [HAU 98]. The application of this method on silicon wafer has been reported in [BEE 03, SHA 18]. Noting that the sample surface need to be strictly smooth while using such method, how to apply this method on our silicon sample need to be further investigated.

We have shown the occurrence of microbranching instabilities along the (110) cleavage plane at the crack velocity higher than about $0.6c_R$. They appear as highly localized entities on the crack front. The bi-stable state of the micobranching instabilities and the stable crack front propagation are co-existing, which leave line-like markings on the frac-

ture surface. However, the formation mechanism of these microbranching instabilities remains unclear. How they affect the fracture energy and disturb the crack front remain to be explored. Besides, the specific surface instabilities along the (111) cleavage plane have been shown. The crack propagation along the (111) plane in our tests involves a mixed mode I + mode III loading. However, these instabilities seem to be different from the helical crack-front instabilities in amorphous materials, and thus need to be further studied.

We have experimentally characterized the nucleation and nonlinear attributes of the corrugation waves in silicon single crystal. It will be interesting to investigate such phenomena in other crystalline materials, as well as the effect of dopants. Besides, a fundamental theory of how corrugation waves emerge from the local kink of bending crack front will be valuable. The theoretical studies and computational simulations of any nonlinear attributes of corrugation waves will be valuable.

Appendix A

Self-affine properties of fracture surfaces

Since the pioneering study on the fractal character of the fracture surface of the steel in 1984 [MAN 84], the self-affinity of fracture surface has been widely investigated. The self-affine property of fracture surface is generally considered to be isotropic and can be characterized by a roughness exponent ζ, deduced via the surface height deviation Δh as a function of the scale of observation within the surface r , where $\Delta h \propto r^{\zeta}$. In the 90s, extensive experimental investigations during the first decade including all failure mode on a variety of materials conjectured that the roughness exponent $\zeta \simeq 0.8$ is a universal exponent [BOU 90, BOU 93, BOU 97, MÅL 92]. However, the presence of this universal exponent remains somewhat controversial [MIL 93, MIL 94, BOU 97, ALA 06]. [MIL 94] reviewed the roughness exponent ζ for both brittle and ductile fracture surfaces of various materials spanning from 0.6 to 1 and indicated the nonuniversal value of ζ. Later, [DAG 96, DAG 97] pointed out that there is a material and crack velocity-dependent length scale, ξ_c. For $r > \xi_c$, the roughness exponent ζ corresponds to the universal value of about 0.8, while for $r < \xi_c$, a smaller exponent $\zeta \sim 0.5$ was observed. This phenomenon was explained as a dynamic effect, where the short and large length scales correspond to quasi-static and dynamic regime, respectively [BOU 95, BOU 97]. Most recently, [PON 06b, PON 06a] reported the anisotropic self-affine properties of the fracture surface, for which the roughness exponents measured along the crack front direction and along the crack propagation direction are different.

Regardless of the universality or not of the roughness exponent, one can discover roughness formation mechanism from the scaling properties of the fracture surface, and further understand the underlying reason of the self-affine fracture surface. For instance, [BOU 02] suggested that the formation and coalescence of damage cavities ahead of the crack front could lead to the fracture surface with a roughness exponent $\zeta \simeq 0.8$. Meanwhile, the authors proposed that the corrugation waves propagating along the moving crack front may generate the fracture surface roughness with a exponent $\zeta \simeq 0.5$. However, no experimental measurements of the fracture surface roughness generated by the corrugation waves have been carried out to validate this conjecture. Moreover, it has been shown

that the fracture roughness increases within the 'mist' and 'hackle' zones of the fracture surface in various materials [JOH 66, FIN 91, SHA 96a, CRA 00]. Whether the roughness exponent is constant in these regions remain to be investigated.

Here, we characterize at small scale the fracture surface of the (110) cleavage plane of silicon single crystal, generated by the interaction of the crack front with the shear waves (Wallner lines) and the corrugation waves (corrugation markings), to study the roughness exponent ζ at these zones. As mentioned in section. 1.3 of Chapiter 2, the fracture surface of as-sawn sample involving the Wallner lines was scanned by laser scanning profilometer (Altisurf-500) with a fixed in-plane resolution of 0.5 μm and an out-of-plane resolution up to 0.5 nm. As mentioned in section. 4.3 of Chapiter 4, the fracture surface of surface-polished sample involving corrugation markings was scanning by AFM (Bruker Dimension 3100 Nanoscope V) with an out-of-plane (along z direction) resolution of 0.1 nm. The measurements were carried out in a square region of 5×5 μm^2 or 10×10 μm^2, corresponding to an in-plane resolution of 5 nm or 10 nm, respectively.

We characterized the fracture surfaces using the 1D height-height correlation function [BOU 97, ALA 06] expressed as :

$$\Delta h(\Delta \mathbf{r}) = < [h(r+\Delta \mathbf{r}) - h(r)]^2 >_r^{1/2} \tag{A.1}$$

where, the brackets denote the average over r. The quantity Δh can be interpreted as the surface height deviation observed by a scaling length Δr along the mean fracture surface. The roughness exponent ζ, lying between 0 and 1, is then obtained by the power law behavior of the correlation function $\Delta h \propto \Delta r^{\zeta}$, where $\zeta = 1$ corresponds to a regular surface, and decreases when the surface is rougher. Besides, the exponent ζ may vary with the direction of $\Delta \mathbf{r}$, which shows an anisotropy of the self-affine fracture surface [PON 06b, PON 06a].

Fig. A.1(a) shows the evolution of the height-height correlation function computed on a fracture surface involving the Waller lines at $v_s = 0.74 c_R$. Only a region (left inset) of 100 $\times$ 50 μm^2 higher than the nucleation of the corrugation markings was taken into account. The computations were carried out along the global crack propagation direction (0°) - the [1-10] direction, the sample thickness direction (90°) - the [001] direction, as well as the intermediate (45°). It can be seen that Δh is a power-law function with Δr in a range between 0.5 and 7 μm (linear part in the logarithmic scale). The roughness exponent was then calculated by the slope of the power-law fit of the evolution. The exponent is found to be ζ = 0.79, and identical for all directions, revealing the isotropy of the self-affine fracture surface. This value is in good agreement with the 'universal' exponent $\zeta \simeq 0.8$ [BOU 97, ALA 06].

The same computation was carried out for the fracture surface zone of corrugation markings with $v_s = 0.80 c_R$ (Fig. A.1(b), left inset). The evolution of Δh as a function of Δr along three directions are shown in Fig. A.1(b) (right inset), which obey a power-law for Δr ranging from 10 to 130 nm. The self-affinity of the fracture surface is isotropic as well. However, the roughness exponent is found to be ζ = 0.95. Furthermore, Fig. A.2 shows the evolution of the height-height correlation function computed along the global crack propagation direction (x) at different crack speed $v_s = 0.67 c_R$ (blue), $v_s = 0.74 c_R$

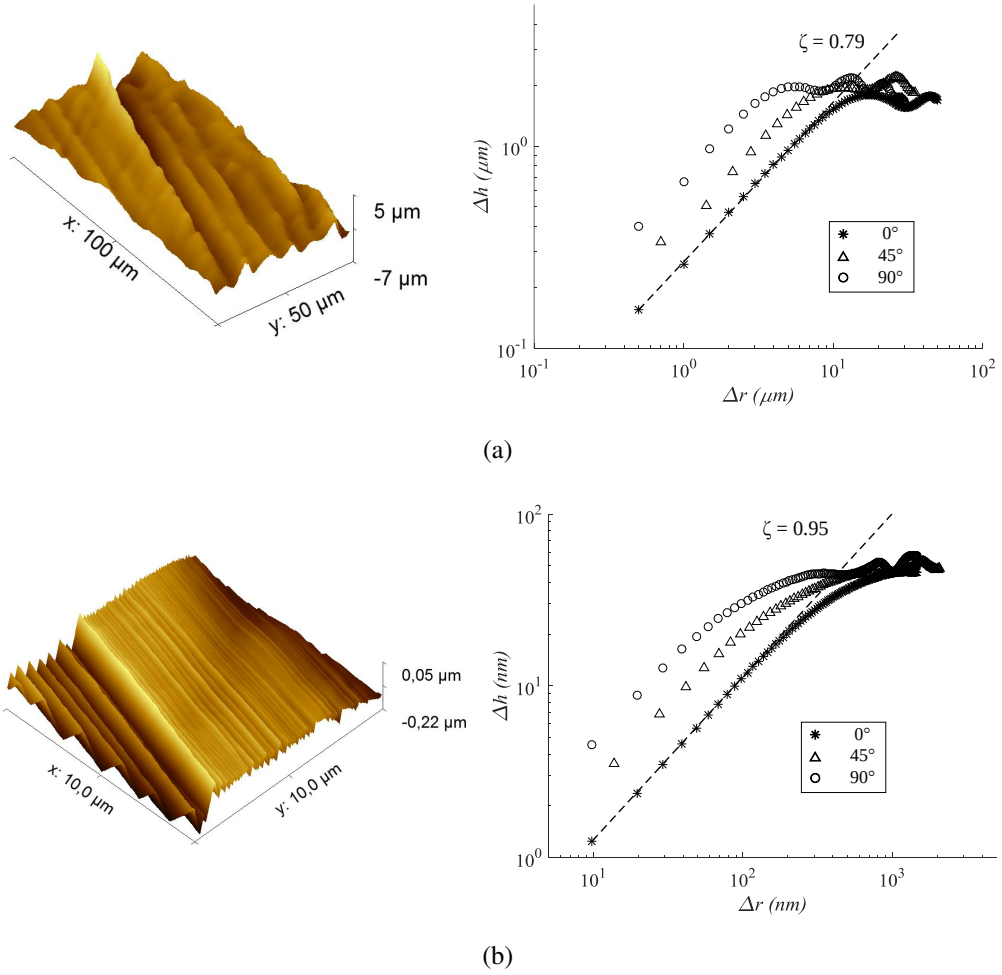

FIGURE A.1: Height-height correlation function calculated along the global crack propagation direction (0°), the sample thickness direction (90°) and the intermediate direction (45°) on the surface zones of (a) Wallner lines at $v_s = 0.74c_R$ and (b) corrugation markings at $v_s = 0.80c_R$. The dotted lines are power-law fits.

(red) and $v_s = 0.80c_R$ (black). For each case, two zones of different heights along the fracture surface, corresponding to different local crack velocities, were characterized. The roughness exponent is nearly invariant for all calculations and is found to be $\zeta = 0.95 \pm 0.03$. This value is different from the roughness exponent of the fracture surface generated by the Wallner lines and is significantly different from the predicted one. In [BOU 02], the authors predicted a roughness exponent $\zeta \simeq 0.5$ for the fracture surface exhibiting corrugation markings, but nonlinear attributes of corrugation waves were not taken into account. The value of $\zeta = 0.95 \pm 0.03$ could be explained by the scale-independent characteristic shape of the corrugation waves. Since the undulation amplitude of the corrugation markings varies linearly with the wavelength, the increase of the surface height deviation Δh is nearly proportional to the scaling length Δr, As a result, the roughness exponent ζ

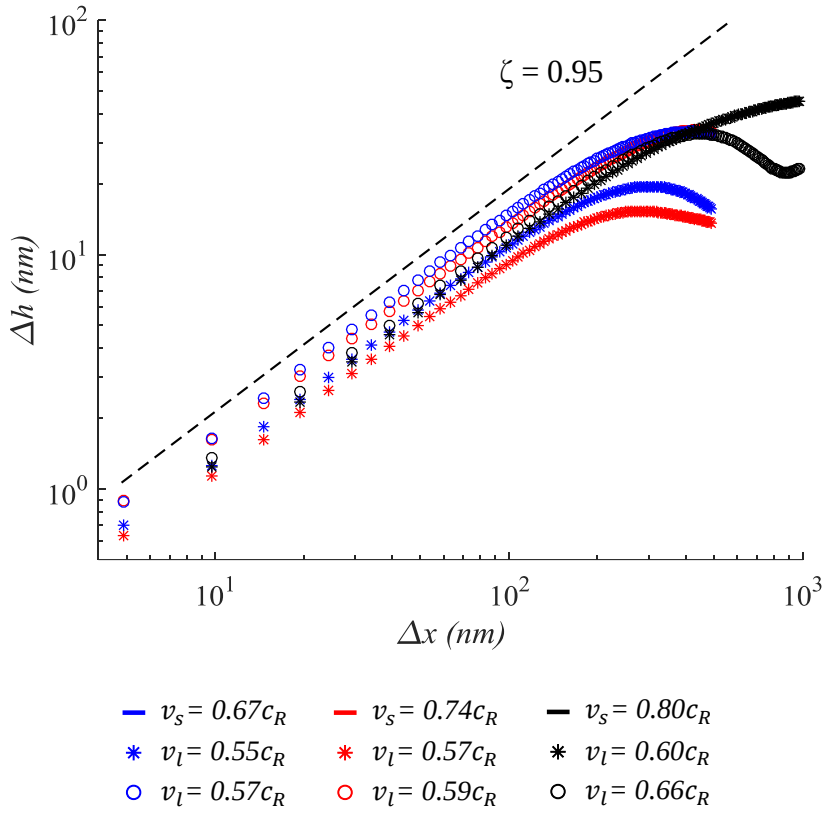

FIGURE A.2: Height-height correlation function calculated along the global crack propagation direction (x) for $v_s = 0.67c_R$ (blue), $v_s = 0.74c_R$ (red) and $v_s = 0.80c_R$ (black) for different height along the sample thickness corresponding to different local crack velocities, presented by different marks.

is close to 1. Besides, since the Wallner lines exhibit no correlation between the amplitude and wavelength, the extension of the Wallner line generates rougher fracture surfaces than the ones generated by the corrugation waves. Hence, the roughness exponent of the surface with Wallner lines is smaller.

Moreover, we indicate that the roughness exponent of the fracture surface generated by corrugation markings $\zeta = 0.95 \pm 0.03$ may break down in the 'hackle' zone. Fig. A.3 show the fracture surface morphologies and the height-height correlation functions of two different zones with $v_s = 0.80c_R$. One can see that the surface zone with $v_l = 0.78c_R$, located near the bottom of the fracture surface, is involved in the 'hackle' region. Although the corrugation markings remain scale-independent, it is conceivable that the fracture surface is rougher in this zone. The corrugation markings collapse with the occurrence of microbranching instabilities and the crack debonding instabilities are more significant. As shown in Fig. A.3 (right inset), the roughness exponent is found to be $\zeta = 0.8$.

As a conclusion, the (110) cleavage surface of silicon single crystal formed during the high speed crack propagation exhibit an isotropic self-affinity. However, the value of the

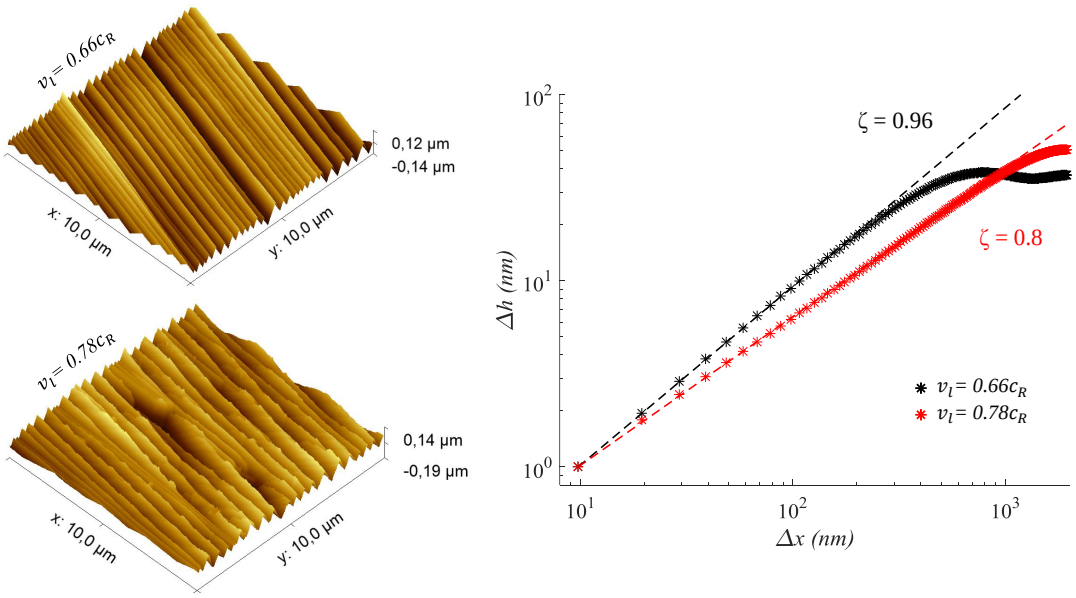

FIGURE A.3: Height-height correlation function calculated along the global crack propagation direction (x) with $v_s = 0.80c_R$ (black) for a surface zone generated by only corrugation markings ($v_l = 0.66c_R$) and a hackle zone ($v_l = 0.78c_R$).

roughness exponent depends on the origin of the surface roughness. In particular, owing to the scale-independent characteristic shape of the corrugation waves, the exponent is found to be 0.95 ± 0.03 for the fracture surface involving corrugation markings. Besides, we show that in the 'hackle' zone of the fracture surface, the occurrence of multiple dynamic fracture instabilities induce a rougher surface and lead to a smaller roughness exponent. These studies bring complementary experimental observations that could help to explain the multi-fractal property of the fracture surface of silicon crystal [TSA 91].

Biblography

[ADD 13] ADDA-BEDIA M., ARIAS R. E., BOUCHBINDER E., KATZAV E.
Dynamic stability of crack fronts : out-of-plane corrugations. *Physical review letters*, vol. 110, n° 1, 2013, page 014302, APS.

[ALA 06] ALAVA M. J., NUKALA P. K., ZAPPERI S.
Statistical models of fracture. *Advances in Physics*, vol. 55, n° 3-4, 2006, p. 349–476, Taylor & Francis.

[ANC 11] ANCO S. C., NGATAT N. T., WILLOUGHBY M.
Interaction properties of complex modified Korteweg–de Vries (mKdV) solitons. *Physica D : Nonlinear Phenomena*, vol. 240, n° 17, 2011, p. 1378–1394, Elsevier.

[AND 17] ANDERSON T. L.
Fracture mechanics : fundamentals and applications. CRC press, 2017.

[ANS 81] ANSTIS G., CHANTIKUL P., LAWN B. R., MARSHALL D.
A critical evaluation of indentation techniques for measuring fracture toughness : I, direct crack measurements. *Journal of the American Ceramic Society*, vol. 64, n° 9, 1981, p. 533–538, Wiley Online Library.

[ANT 70] ANTHONY S., CHUBB J., CONGLETON J.
The crack-branching velocity. *Philosophical Magazine*, vol. 22, n° 180, 1970, p. 1201–1216, Taylor & Francis.

[ARA 91] ARAKAWA K., TAKAHASHI K.
Branching of a fast crack in polymers. *International Journal of fracture*, vol. 48, n° 4, 1991, p. 245–254, Springer.

[ATR 11a] ATRASH F., HASHIBON A., GUMBSCH P., SHERMAN D.
Phonon emission induced dynamic fracture phenomena. *Physical review letters*, vol. 106, n° 8, 2011, page 085502, APS.

[ATR 11b] ATRASH F., SHERMAN D.
Evaluation of the thermal phonon emission in dynamic fracture of brittle crystals. *Physical Review B*, vol. 84, n° 22, 2011, page 224307, APS.

[ATR 12] ATRASH F., SHERMAN D.
Dynamic fracture instabilities in brittle crystals generated by thermal phonon emission : Experiments and atomistic calculations. *Journal of the Mechanics and Physics of Solids*, vol. 60, n° 5, 2012, p. 844–856, Elsevier.

[AUD 05a] AUDOLY B., NEUKIRCH S.
Fragmentation of rods by cascading cracks : why spaghetti does not break in half. *Physical review letters*, vol. 95, n° 9, 2005, page 095505, APS.

[AUD 05b] AUDOLY B., NEUKIRCH S.
Fragmentation of rods by cascading cracks : why spaghetti does not break in half. *Physical Review Letters*, vol. 95, n° 9, 2005, page 095505, APS.

[AZA 16] AZAR A. S., HOLME B., NIELSEN Ø.
Effect of sawing induced micro-crack orientations on fracture properties of silicon wafers. *Engineering Fracture Mechanics*, vol. 154, 2016, p. 262–271, Elsevier.

[BAI 91] BAILEY D., SAYLES R.
Effect of roughness and sliding friction on contact stresses. *Journal of tribology*, vol. 113, n° 4, 1991, p. 729–738, American Society of Mechanical Engineers.

[BEE 03] BEERY I., LEV U., SHERMAN D.
On the lower limiting velocity of a dynamic crack in brittle solids. *Journal of Applied Physics*, vol. 93, n° 5, 2003, p. 2429–2434, AIP.

[BEN 06] BENES N., KASMAN A., YOUNG K.
On decompositions of the KdV 2-Soliton. *Journal of Nonlinear Science*, vol. 16, n° 2, 2006, p. 179–200, Springer.

[BHA 86] BHADURI S. B., WANG F. F.
Fracture surface energy determination in $\{1\,1\,0\}$ planes in silicon by the double torsion method. *Journal of materials science*, vol. 21, n° 7, 1986, p. 2489–2492, Springer.

[BON 03] BONAMY D., RAVI-CHANDAR K.
Interaction of shear waves and propagating cracks. *Physical Review Letters*, vol. 91, n° 23, 2003, page 235502, APS.

[BON 04] BONAMY D., RAVI-CHANDAR K.
Reply on : interaction of shear waves and propagating cracks. *Physical Review Letter*, vol. 93, n° 099602, 2004, page 1.

[BON 05] BONAMY D., RAVI-CHANDAR K.
Dynamic crack response to a localized shear pulse perturbation in brittle amorphous materials : on crack surface roughening. *International Journal of Fracture*, vol. 134, n° 1, 2005, p. 1–22, Springer.

[BOU 90] BOUCHAUD E., LAPASSET G., PLANES J.
Fractal dimension of fractured surfaces : a universal value ? *EPL (Europhysics Letters)*, vol. 13, n° 1, 1990, page 73, IOP Publishing.

[BOU 93] BOUCHAUD E., LAPASSET G., PLANES J., NAVEOS S.
Statistics of branched fracture surfaces. *Physical Review B*, vol. 48, n° 5, 1993, page 2917, APS.

[BOU 95] BOUCHAUD E., NAVÉOS S.
From quasi-static to rapid fracture. *Journal de Physique I*, vol. 5, n° 5, 1995, p. 547–554, EDP Sciences.

[BOU 97] BOUCHAUD E.
Scaling properties of cracks. *Journal of Physics : Condensed Matter*, vol. 9, n° 21, 1997, page 4319, IOP Publishing.

[BOU 98] BOUDET J., CILIBERTO S.
Interaction of sound with fast crack propagation. *Physical review letters*, vol. 80, n° 2, 1998, page 341, APS.

[BOU 02] BOUCHAUD E., BOUCHAUD J., FISHER D., RAMANATHAN S., RICE J.
Can crack front waves explain the roughness of cracks ? *Journal of the Mechanics and Physics of Solids*, vol. 50, n° 8, 2002, p. 1703–1725, Elsevier.

[BOU 09a] BOUCHBINDER E.
Dynamic crack tip equation of motion : high-speed oscillatory instability. *Physical review letters*, vol. 103, n° 16, 2009, page 164301, APS.

[BOU 09b] BOUCHBINDER E., LIVNE A., FINEBERG J.
The 1/r singularity in weakly nonlinear fracture mechanics. *Journal of the Mechanics and Physics of Solids*, vol. 57, n° 9, 2009, p. 1568–1577, Elsevier.

[BOU 14] BOUCHBINDER E., GOLDMAN T., FINEBERG J.
The dynamics of rapid fracture : instabilities, nonlinearities and length scales. *Reports on Progress in Physics*, vol. 77, n° 4, 2014, page 046501, IOP Publishing.

[BOU 15] BOUÉ T. G., COHEN G., FINEBERG J.
Origin of the microbranching instability in rapid cracks. *Physical review letters*, vol. 114, n° 5, 2015, page 054301, APS.

[BRO 66] BROWN W., SRAWLEY J.
Plane strain crack toughness testing of high strength metallic materials. *Plane Strain Crack Toughness Testing of High Strength Metallic Materials* ASTM International, 1966.

[BUE 07] BUEHLER M. J., TANG H., VAN DUIN A. C., GODDARD III W. A.
Threshold crack speed controls dynamical fracture of silicon single crystals. *Physical Review Letters*, vol. 99, n° 16, 2007, page 165502, APS.

[BUS 01] BUSCHOW K. J., CAHN R. W., FLEMINGS M. C., ILSCHNER B., KRAMER E. J., MAHAJAN S.
Encyclopedia of materials. *Science and technology*, vol. 1, 2001, page 11.

[CHE 80] CHEN C. P., LEIPOLD M. H.
Fracture toughness of silicon. *American Ceramic Society Bulletin*, vol. 59, 1980, p. 469–472.

[CHE 15] CHEN C.-H., CAMBONIE T., LAZARUS V., NICOLI M., PONS A. J., KARMA A.
Crack front segmentation and facet coarsening in mixed-mode fracture. *Physical review letters*, vol. 115, n° 26, 2015, page 265503, APS.

[CHE 17] CHEN C.-H., BOUCHBINDER E., KARMA A.
Instability in dynamic fracture and the failure of the classical theory of cracks. *Nature Physics*, vol. 13, n° 12, 2017, page 1186, Nature Publishing Group.

[COU 94] COUFAL H., MEYER K., GRYGIER R. K., HESS P., NEUBRAND A.
Precision measurement of the surface acoustic wave velocity on silicon single crystals using optical excitation and detection. *The Journal of the Acoustical Society of America*, vol. 95, n° 2, 1994, p. 1158–1160, ASA.

[CRA 00] CRAMER T., WANNER A., GUMBSCH P.
Energy dissipation and path instabilities in dynamic fracture of silicon single crystals. *Physical Review Letters*, vol. 85, n° 4, 2000, page 788, APS.

[CZO 18] CZOCHRALSKI J.
Ein neues verfahren zur messung der kristallisationsgeschwindigkeit der metalle. *Zeitschrift für physikalische Chemie*, vol. 92, n° 1, 1918, p. 219–221, De Gruyter Oldenbourg.

[DAG 96] DAGUIER P., HENAUX S., BOUCHAUD E., CREUZET F.
Quantitative analysis of a fracture surface by atomic force microscopy. *Physical Review E*, vol. 53, n° 6, 1996, page 5637, APS.

[DAG 97] DAGUIER P., NGHIEM B., BOUCHAUD E., CREUZET F.
Pinning and depinning of crack fronts in heterogeneous materials. *Physical Review Letters*, vol. 78, n° 6, 1997, page 1062, APS.

[ECK 98] ECKL C., MAYER A., KOVALEV A.
Do surface acoustic solitons exist ? *Physical Review Letters*, vol. 81, n° 5, 1998, page 983, APS.

[FEK 20] FEKAK F., BARRAS F., DUBOIS A., SPIELMANN D., BONAMY D., GEUBELLE P., MOLINARI J.
Crack front waves : A 3D dynamic response to a local perturbation of tensile and shear cracks. *Journal of the Mechanics and Physics of Solids*, vol. 135, 2020, page 103806, Elsevier.

[FIE 71] FIELD J.
Brittle fracture : its study and application. *Contemporary Physics*, vol. 12, n° 1, 1971, p. 1–31, Taylor & Francis.

[FIE 83] FIELD J.
High-speed photography. *Contemporary Physics*, vol. 24, n° 5, 1983, p. 439–459, Taylor & Francis.

[FIN 91] FINEBERG J., GROSS S. P., MARDER M., SWINNEY H. L.
Instability in dynamic fracture. *Physical Review Letters*, vol. 67, n° 4, 1991, page 457, APS.

[FIN 03] FINEBERG J., SHARON E., COHEN G.
Crack front waves in dynamic fracture. *International Journal of Fracture*, vol. 121, n° 1-2, 2003, p. 55–69, Springer.

[FRA 19] FRAUNHOFER I.
Photovoltaics report. *Fraunhofer ISE, Freiburg*, , 2019.

[FRE 98] FREUND L. B.
Dynamic fracture mechanics. Cambridge university press, 1998.

[GIL 60] GILMAN J. J.
Direct measurements of the surface energies of crystals. *Journal of Applied Physics*, vol. 31, n° 12, 1960, p. 2208–2218, AIP.

[GLE 14] GLEIZER A., PERALTA G., KERMODE J. R., DE VITA A., SHERMAN D.
Dissociative chemisorption of O 2 inducing stress corrosion cracking in silicon crystals. *Physical review letters*, vol. 112, n° 11, 2014, page 115501, APS.

[GOL 10a] GOLDMAN T., LIVNE A., FINEBERG J.
Acquisition of inertia by a moving crack. *Physical Review Letters*, vol. 104, n° 11, 2010, page 114301, APS.

[GOL 10b] GOLDMAN T., LIVNE A., FINEBERG J.
Acquisition of inertia by a moving crack. *Physical review letters*, vol. 104, n° 11, 2010, page 114301, APS.

[GOL 12] GOLDMAN T., HARPAZ R., BOUCHBINDER E., FINEBERG J.
Intrinsic nonlinear scale governs oscillations in rapid fracture. *Physical review letters*, vol. 108, n° 10, 2012, page 104303, APS.

[GON 18] GONZÁLEZ-VELÁZQUEZ J. L.
Fractography and Failure Analysis. Springer, 2018.

[GRE 04] GREEN M. A.
Third generation photovoltaics : advanced solar energy conversion. *Physics Today*, vol. 57, n° 12, 2004, p. 71–72.

[GRÉ 07] GRÉGOIRE D., MAIGRE H., RETHORE J., COMBESCURE A.
Dynamic crack propagation under mixed-mode loading–comparison between experiments and X-FEM simulations. *International journal of solids and structures*, vol. 44, n° 20, 2007, p. 6517–6534, Elsevier.

[GRI 21] GRIFFITH A. A.
The phenomena of rupture and flow in solids. *Philosophical transactions of the royal society of london. Series A, containing papers of a mathematical or physical character*, vol. 221, 1921, p. 163–198, JSTOR.

[GRO 93] GROSS S. P., FINEBERG J., MARDER M., MCCORMICK W., SWINNEY H. L.
Acoustic emissions from rapidly moving cracks. *Physical review letters*, vol. 71, n° 19, 1993, page 3162, APS.

[GUE 12] GUERRA C., SCHEIBERT J., BONAMY D., DALMAS D.
Understanding fast macroscale fracture from microcrack post mortem patterns. *Proceedings of the National Academy of Sciences*, vol. 109, n° 2, 2012, p. 390–394, National Acad Sciences.

[HAB 11] HABOUSSA D., GRÉGOIRE D., ELGUEDJ T., MAIGRE H., COMBESCURE A.
X-FEM analysis of the effects of holes or other cracks on dynamic crack propagations. *International Journal for Numerical Methods in Engineering*, vol. 86, n° 4-5, 2011, p. 618–636, Wiley Online Library.

[HAU 98] HAUCH J., MARDER M.
Energy balance in dynamic fracture, investigated by a potential drop technique. *International Journal of Fracture*, vol. 90, n° 1-2, 1998, p. 133–151, Springer.

[HAU 99] HAUCH J. A., HOLLAND D., MARDER M., SWINNEY H. L.
Dynamic fracture in single crystal silicon. *Physical Review Letters*, vol. 82, n° 19, 1999, page 3823, APS.

[HES 93] HESKETH P. J., JU C., GOWDA S., ZANORIA E., DANYLUK S.
Surface free energy model of silicon anisotropic etching. *Journal of The Electrochemical Society*, vol. 140, n° 4, 1993, p. 1080–1085, The Electrochemical Society.

[HIR 89] HIRSCH P., ROBERTS S., SAMUELS J.
The brittle-ductile transition in silicon. II. Interpretation. *Proceedings of the Royal Society of London A : Mathematical, Physical and Engineering Sciences*, vol. 421 The Royal Society, 1989, p. 25–53.

[HOP 10] HOPCROFT M. A., NIX W. D., KENNY T. W.
What is the Young's Modulus of Silicon ? *Journal of microelectromechanical systems*, vol. 19, n° 2, 2010, p. 229–238, IEEE.

[INF 14] INFUSO A., CORRADO M., PAGGI M.
Image analysis of polycrystalline solar cells and modelling of intergranular and transgranular cracking. *Journal of the European Ceramic Society*, vol. 34, n° 11, 2014, p. 2713–2722, Elsevier.

[ING 13] INGLIS C. E.
Stresses in a plate due to the presence of cracks and sharp corners. *Trans Inst Naval Archit*, vol. 55, 1913, p. 219–241.

[IRW 57] IRWIN G. R.
Analysis of stresses and strains near the end of a crack transversing a plate. *Trans. ASME, Ser. E, J. Appl. Mech.*, vol. 24, 1957, p. 361–364.

[ITR] ITRPV
International technology roadmap for photovoltaic results. *ITRPV*.

[JAC 63] JACCODINE R.
Surface energy of germanium and silicon. *Journal of The Electrochemical Society*, vol. 110, n° 6, 1963, p. 524–527, The Electrochemical Society.

[JOH 66] JOHNSON J., HOLLOWAY D.
On the shape and size of the fracture zones on glass fracture surfaces. *The Philosophical Magazine : A Journal of Theoretical Experimental and Applied Physics*, vol. 14, n° 130, 1966, p. 731–743, Taylor & Francis.

[JOH 87] JOHNSON K. L., JOHNSON K. L.
Contact mechanics. Cambridge university press, 1987.

[KAJ 11] KAJARI-SCHRÖDER S., KUNZE I., EITNER U., KÖNTGES M.
Spatial and orientational distribution of cracks in crystalline photovoltaic modules generated by mechanical load tests. *Solar Energy Materials and Solar Cells*, vol. 95, n° 11, 2011, p. 3054–3059, Elsevier.

[KER 08a] KERMODE J. R., ALBARET T., SHERMAN D., BERNSTEIN N., GUMBSCH P., PAYNE M. C., CSÁNYI G., DE VITA A.
Low-speed fracture instabilities in a brittle crystal. *Nature*, vol. 455, n° 7217, 2008, p. 1224–1227, Nature Publishing Group.

[KER 08b] KERMODE J. R., ALBARET T., SHERMAN D., BERNSTEIN N., GUMBSCH P., PAYNE M. C., CSÁNYI G., DE VITA A.
Low-speed fracture instabilities in a brittle crystal. *Nature*, vol. 455, n° 7217, 2008, p. 1224–1227, Nature Publishing Group.

[KER 13] KERMODE J. R., BEN-BASHAT L., ATRASH F., CILLIERS J., SHERMAN D., DE VITA A.
Macroscopic scattering of cracks initiated at single impurity atoms. *Nature communications*, vol. 4, 2013, page ncomms3441, Nature Publishing Group.

[KER 15] KERMODE J. R., GLEIZER A., KOVEL G., PASTEWKA L., CSÁNYI G., SHERMAN D., DE VITA A.
Low speed crack propagation via kink formation and advance on the silicon (110) cleavage plane. *Physical review letters*, vol. 115, n° 13, 2015, page 135501, APS.

[KNA 85] KNAUSS W., RAVI-CHANDAR K.
Some basic problems in stress wave dominated fracture. *Dynamic fracture*, p. 1–17 Springer, 1985.

[KOL 15] KOLVIN I., COHEN G., FINEBERG J.
Crack front dynamics : the interplay of singular geometry and crack instabilities. *Physical review letters*, vol. 114, n° 17, 2015, page 175501, APS.

[KOL 18] KOLVIN I., COHEN G., FINEBERG J.
Topological defects govern crack front motion and facet formation on broken surfaces. *Nature materials*, vol. 17, n° 2, 2018, page 140, Nature Publishing Group.

[KÖN 17] KÖNTGES M., ORESKI G., JAHN U., HERZ M., HACKE P., WEISS K.-A.
Assessment of photovoltaic module failures in the field : International Energy Agency Photovoltaic Power Systems Programme : IEA PVPS Task 13, Subtask 3 : report IEA-PVPS T13-09 : 2017. International Energy Agency, 2017.

[KUL 95] KULANDER B., DEAN S. L.
Observations on fractography with laboratory experiments for geologists. *Geological Society, London, Special Publications*, vol. 92, n° 1, 1995, p. 59–82, Geological Society of London.

[LAW 93] LAWN B.
Fracture of brittle solids. Cambridge university press, 1993.

[LEB 15] LEBLOND J.-B., LAZARUS V.
On the strong influence of imperfections upon the quick deviation of a mode I+ III crack from coplanarity. *Journal of Mechanics of Materials and Structures*, vol. 10, n° 3, 2015, p. 299–315, Mathematical Sciences Publishers.

[LEB 19] LEBLOND J.-B., KARMA A., PONSON L., VASUDEVAN A.
Configurational stability of a crack propagating in a material with mode-dependent fracture energy-Part I : Mixed-mode I+ III. *Journal of the Mechanics and Physics of Solids*, vol. 126, 2019, p. 187–203, Elsevier.

[LI 05] LI X., KASAI T., NAKAO S., ANDO T., SHIKIDA M., SATO K., TANAKA H.
Anisotropy in fracture of single crystal silicon film characterized under uniaxial tensile condition. *Sensors and Actuators A : Physical*, vol. 117, n° 1, 2005, p. 143–150, Elsevier.

[LIN 99] LIN X., SMITH R.
Finite element modelling of fatigue crack growth of surface cracked plates : Part I : The numerical technique. *Engineering Fracture Mechanics*, vol. 63, n° 5, 1999, p. 503–522, Elsevier.

[LIU 15] LIU M., GAN Y., HANAOR D. A., LIU B., CHEN C.
An improved semi-analytical solution for stress at round-tip notches. *Engineering fracture mechanics*, vol. 149, 2015, p. 134–143, Elsevier.

[LIV 05] LIVNE A., COHEN G., FINEBERG J.
Universality and hysteretic dynamics in rapid fracture. *Physical review letters*, vol. 94, n° 22, 2005, page 224301, APS.

[LIV 07] LIVNE A., BEN-DAVID O., FINEBERG J.
Oscillations in rapid fracture. *Physical review letters*, vol. 98, n° 12, 2007, page 124301, APS.

[LIV 10] LIVNE A., BOUCHBINDER E., SVETLIZKY I., FINEBERG J.
The near-tip fields of fast cracks. *Science*, vol. 327, n° 5971, 2010, p. 1359–1363, American Association for the Advancement of Science.

[LOM 99] LOMONOSOV A., HESS P.
Effects of nonlinear elastic surface pulses in anisotropic silicon crystals. *Physical review letters*, vol. 83, n° 19, 1999, page 3876, APS.

[MAD 02] MADELUNG O., RÖSSLER U., SCHULZ M.
Group IV Elements, IV-IV and III-V Compounds. Part b-Electronic, Transport, Optical and Other Properties. *Landolt-Börnstein–Group III Condensed Matter*, vol. 41, 2002, Springer.

[MÅL 92] MÅLØY K. J., HANSEN A., HINRICHSEN E. L., ROUX S.
Experimental measurements of the roughness of brittle cracks. *Physical Review Letters*, vol. 68, n° 2, 1992, page 213, APS.

[MAN 84] MANDELBROT B. B., PASSOJA D. E., PAULLAY A. J.
Fractal character of fracture surfaces of metals. *Nature*, vol. 308, n° 5961, 1984, page 721, Nature Publishing Group.

[MAR 91] MARDER M.
New dynamical equation for cracks. *Physical review letters*, vol. 66, n° 19, 1991, page 2484, APS.

[MAS 18] MASSY D., MAZEN F., LANDRU D., MOHAMED N. B., TARDIF S., REINHARDT A., MADEIRA F., KONONCHUK O., RIEUTORD F.
Crack Front Interaction with Self-Emitted Acoustic Waves. *Physical review letters*, vol. 121, n° 19, 2018, page 195501, APS.

[MIL 93] MILMAN V. Y., BLUMENFELD R., STELMASHENKO N., BALL R.
Comment on ŚŚExperimental measurements of the roughness of brittle cracksŠŠ. *Physical review letters*, vol. 71, n° 1, 1993, page 204, APS.

[MIL 94] MILMAN V. Y., STELMASHENKO N. A., BLUMENFELD R.
Fracture surfaces : a critical review of fractal studies and a novel morphological analysis of scanning tunneling microscopy measurements. *Progress in Materials Science*, vol. 38, 1994, p. 425–474, Pergamon.

[MOR 98] MORRISSEY J. W., RICE J. R.
Crack front waves. *Journal of the Mechanics and Physics of Solids*, vol. 46, n° 3, 1998, p. 467–487, Elsevier.

[MOR 00] MORRISSEY J. W., RICE J. R.
Perturbative simulations of crack front waves. *Journal of the Mechanics and Physics of Solids*, vol. 48, n° 6, 2000, p. 1229–1251, Elsevier.

[NAR 14] NARAYAN R., TANDAIYA P., NARASIMHAN R., RAMAMURTY U.
Wallner lines, crack velocity and mechanisms of crack nucleation and growth in a brittle bulk metallic glass. *Acta Materialia*, vol. 80, 2014, p. 407–420, Elsevier.

[NEČ 12] NEČAS D., KLAPETEK P.
Gwyddion : an open-source software for SPM data analysis. *Open Physics*, vol. 10, n° 1, 2012, p. 181–188, Versita.

[NEW] NEWMAN JR J., RAJU I.
Analysis of surface cracks in finite plates under tension or bending loads. *NATIONAL AERONAUTICS AND SPACE ADMINISTRATION HAMPTON VA LANGLEY RESEARCH CEN TER*, vol. 1579.

[NEW 81] NEWMAN J., RAJU I.
An empirical stress-intensity factor equation for the surface crack. *Engineering fracture mechanics*, vol. 15, n° 1-2, 1981, p. 185–192, Elsevier.

[NOG 97] NOGI T., KATO T.
Influence of a hard surface layer on the limit of elastic contact-Part I : Analysis using a real surface model. *Journal of tribology*, vol. 119, n° 3, 1997, p. 493–500, American Society of Mechanical Engineers.

[NOR 07] NORRIS A. N., ABRAHAMS I. D.
A multiple-scales approach to crack-front waves. *Journal of Engineering Mathematics*, vol. 59, n° 4, 2007, p. 399–417, Springer.

[ORO 49] OROWAN E.
Fracture and strength of solids. *Reports on progress in physics*, vol. 12, n° 1, 1949, page 185, IOP Publishing.

[PAG 18] PAGGI M., CORRADO M., REINOSO J.
Fracture of solar-grade anisotropic polycrystalline Silicon : A combined phase field–cohesive zone model approach. *Computer Methods in Applied Mechanics and Engineering*, vol. 330, 2018, p. 123–148, Elsevier.

[PAY 76] PAYNE B., BALL A.
The determination of crack velocities in anisotropic materials by the analysis of Wallner lines. *Philosophical Magazine*, vol. 34, n° 5, 1976, p. 917–922, Taylor & Francis.

[PER 94] PERRIN G., RICE J. R.
Disordering of a dynamic planar crack front in a model elastic medium of randomly variable toughness. *Journal of the Mechanics and Physics of Solids*, vol. 42, n° 6, 1994, p. 1047–1064, Elsevier.

[PÉR 00a] PÉREZ R., GUMBSCH P.
An ab initio study of the cleavage anisotropy in silicon. *Acta Materialia*, vol. 48, n° 18, 2000, p. 4517–4530, Elsevier.

[PÉR 00b] PÉREZ R., GUMBSCH P.
Directional anisotropy in the cleavage fracture of silicon. *Physical review letters*, vol. 84, n° 23, 2000, page 5347, APS.

[PÉR 00c] PÉREZ R., GUMBSCH P.
Directional anisotropy in the cleavage fracture of silicon. *Physical review letters*, vol. 84, n° 23, 2000, page 5347, APS.

[PON 06a] PONSON L., BONAMY D., AURADOU H., MOUROT G., MOREL S., BOUCHAUD E., GUILLOT C., HULIN J.-P.
Anisotropic self-affine properties of experimental fracture surfaces. *International Journal of fracture*, vol. 140, n° 1-4, 2006, p. 27–37, Springer.

[PON 06b] PONSON L., BONAMY D., BOUCHAUD E.
Two-dimensional scaling properties of experimental fracture surfaces. *Physical review letters*, vol. 96, n° 3, 2006, page 035506, APS.

[PON 10] PONS A. J., KARMA A.
Helical crack-front instability in mixed-mode fracture. *Nature*, vol. 464, n° 7285, 2010, page 85, Nature Publishing Group.

[PRA 69] PRATT R., LIM T.
Acoustic surface waves on silicon. *Applied Physics Letters*, vol. 15, n° 12, 1969, p. 403–405, AIP.

[RAB 06] RABINOVITCH A., FRID V., BAHAT D.
Wallner lines revisited. *Journal of Applied Physics*, vol. 99, 2006, page 076102, APS.

[RAC 16] RACK A., SCHEEL M., DANILEWSKY A. N.
Real-time direct and diffraction X-ray imaging of irregular silicon wafer breakage. *IUCrJ*, vol. 3, n° 2, 2016, p. 108–114, International Union of Crystallography.

[RAM 97a] RAMANATHAN S., ERTAŞ D., FISHER D. S.
Quasistatic crack propagation in heterogeneous media. *Physical review letters*, vol. 79, n° 5, 1997, page 873, APS.

[RAM 97b] RAMANATHAN S., FISHER D. S.
Dynamics and instabilities of planar tensile cracks in heterogeneous media. *Physical Review Letters*, vol. 79, n° 5, 1997, page 877, APS.

[RAV 84] RAVI-CHANDAR K., KNAUSS W.
An experimental investigation into dynamic fracture : IV. On the interaction of stress waves with propagating cracks. *International Journal of Fracture*, vol. 26, n° 3, 1984, p. 189–200, Springer.

[RAV 97] RAVI-CHANDAR K., YANG B.
On the role of microcracks in the dynamic fracture of brittle materials. *Journal of the Mechanics and Physics of Solids*, vol. 45, n° 4, 1997, p. 535–563, Elsevier.

[REM 13] REMOISSENET M.
Waves called solitons : concepts and experiments. Springer Science & Business Media, 2013.

[RIC 68] RICE J. R.
A path independent integral and the approximate analysis of strain concentration by notches and cracks. *Journal of applied mechanics*, vol. 35, n° 2, 1968, p. 379–386, American Society of Mechanical Engineers.

[RIC 94] RICE J. R., BEN-ZION Y., KLM K.-S.
Three-dimensional perturbation solution for a dynamic planar crack moving unsteadily in a model elastic solid. *Journal of the Mechanics and Physics of Solids*, vol. 42, n° 5, 1994, p. 813–843, Elsevier.

[RON 14] RONSIN O., CAROLI C., BAUMBERGER T.
Crack front echelon instability in mixed mode fracture of a strongly nonlinear elastic solid. *EPL (Europhysics Letters)*, vol. 105, n° 3, 2014, page 34001, IOP Publishing.

[ROS 84] ROSAKIS A., DUFFY J., FREUND L.
The determination of dynamic fracture toughness of AISI 4340 steel by the shadow spot method. *Journal of the Mechanics and Physics of Solids*, vol. 32, n° 6, 1984, p. 443–460, Elsevier.

[RUP 09] RUPNOWSKI P., SOPORI B.
Strength of silicon wafers : fracture mechanics approach. *International Journal of Fracture*, vol. 155, n° 1, 2009, p. 67–74, Springer.

[SAM 89] SAMUELS J., ROBERTS S.
The brittle-ductile transition in silicon. I. Experiments. *Proceedings of the royal society of London A : mathematical, physical and engineering sciences*, vol. 421 The Royal Society, 1989, p. 1–23.

[SCH 55] SCHARDIN H., MUCKE L., STRUTH W., RHEIN W.
Cracking velocity of glasses. *The Glass Industry*, vol. 36, n° 3, 1955, p. 133–138.

[SCH 10] SCHEIBERT J., GUERRA C., CÉLARIÉ F., DALMAS D., BONAMY D.
Brittle-quasibrittle transition in dynamic fracture : An energetic signature. *Physical Review Letters*, vol. 104, n° 4, 2010, page 045501, APS.

[SEK 18] SEKHAR H., FUKUDA T., TANAHASHI K., SHIRASAWA K., TAKATO H., OHKUBO K., ONO H., SAMPEI Y., KOBAYASHI T.
The impact of saw mark direction on the fracture strength of thin (120 μm) monocrystalline silicon wafers for photovoltaic cells. *Japanese Journal of Applied Physics*, vol. 57, n° 9, 2018, page 095501, IOP Publishing.

[SHA 96a] SHARON E., FINEBERG J.
Microbranching instability and the dynamic fracture of brittle materials. *Physical Review B*, vol. 54, n° 10, 1996, page 7128, APS.

[SHA 96b] SHARON E., GROSS S. P., FINEBERG J.
Energy dissipation in dynamic fracture. *Physical review letters*, vol. 76, n° 12, 1996, page 2117, APS.

[SHA 99] SHARON E., FINEBERG J.
Confirming the continuum theory of dynamic brittle fracture for fast cracks. *Nature*, vol. 397, n° 6717, 1999, page 333, Nature Publishing Group.

[SHA 01] SHARON E., COHEN G., FINEBERG J.
Propagating solitary waves along a rapidly moving crack front. *Nature*, vol. 410, n° 6824, 2001, p. 68–71, Nature Publishing Group.

[SHA 02] SHARON E., COHEN G., FINEBERG J.
Crack front waves and the dynamics of a rapidly moving crack. *Physical Review Letters*, vol. 88, n° 8, 2002, page 085503, APS.

[SHA 04] SHARON E., COHEN G., FINEBERG J.
Comment on "Interaction of shear waves and propagating cracks". *Physical Review Letters*, vol. 93, 2004, page 099601.

[SHA 18] SHAHEEN-MUALIM M., SHERMAN D.
The dynamic cleavage energy of brittle single crystals. *International Journal of Engineering Science*, vol. 129, 2018, p. 111–128, Elsevier.

[SHE 03a] SHERMAN D.
Hackle or textured mirror ? Analysis of surface perturbation in single crystal silicon. *Journal of materials science*, vol. 38, n° 4, 2003, p. 783–788, Springer.

[SHE 03b] SHERMAN D., BEŠERY I.
Velocity dependent crack deflection in single crystal silicon. *Scripta materialia*, vol. 49, n° 6, 2003, p. 551–555, Elsevier.

[SHE 04] SHERMAN D., BE'ERY I.
From crack deflection to lattice vibrationsŮmacro to atomistic examination of dynamic cleavage fracture. *Journal of the Mechanics and Physics of Solids*, vol. 52, n° 8, 2004, p. 1743–1761, Elsevier.

[SHE 05] SHERMAN D.
Macroscopic and microscopic examination of the relationship between crack velocity and path and Rayleigh surface wave speed in single crystal silicon. *Journal of the Mechanics and Physics of Solids*, vol. 53, n° 12, 2005, p. 2742–2757, Elsevier.

[SHE 08] SHERMAN D., MARKOVITZ M., BARKAI O.
Dynamic instabilities in $\{111\}$ silicon. *Journal of the Mechanics and Physics of Solids*, vol. 56, n° 2, 2008, p. 376–387, Elsevier.

[SHI 91] SHIOYA T., ISHIDA R.
Microscopic fracture modes of brittle polymers in dynamic crack propagation. *Dynamic Failure of Materials*, p. 351–361 Springer, 1991.

[SHI 04] SHIN C., CAI C.
Experimental and finite element analyses on stress intensity factors of an elliptical surface crack in a circular shaft under tension and bending. *International Journal of Fracture*, vol. 129, n° 3, 2004, p. 239–264, Springer.

[SIN 16] SINGH I., NARASIMHAN R., RAMAMURTY U.
Cavitation-induced fracture causes nanocorrugations in brittle metallic glasses. *Physical review letters*, vol. 117, n° 4, 2016, page 044302, APS.

[SOM 69] SOMMER E.
Formation of fracture lances in glass. *Engineering Fracture Mechanics*, vol. 1, n° 3, 1969, p. 539–546, Elsevier.

[STA 83] STALDER B., BÉGUELIN P., KAUSCH H.
A simple velocity gauge for measuring crack growth. *International Journal of Fracture*, vol. 22, n° 2, 1983, p. R47–R50, Springer.

[SWA 04] SWADENER J. G., BASKES M. I., NASTASI M. A.
Dynamic fracture toughness determined using molecular dynamics. rapport, 2004, Los Alamos National Laboratory.

[THE 84] THEOCARIS P., GEORGIADIS H.
Rayleigh waves emitted by a propagating crack in a strain-rate dependent elastic medium. *Journal of the Mechanics and Physics of Solids*, vol. 32, n° 6, 1984, p. 491–510, Elsevier.

[TSA 91] TSAI Y., MECHOLSKY J.
Fractal fracture of single crystal silicon. *Journal of Materials Research*, vol. 6, n° 6, 1991, p. 1248–1263, Cambridge University Press.

[VER 19] VERHEEST F., HEREMAN W. A.
Collisions of acoustic solitons and their electric fields in plasmas at critical compositions. *Journal of Plasma Physics*, vol. 85, n° 1, 2019, Cambridge University Press.

[WAL 39] WALLNER H.
Linienstrukturen an bruchflächen. *Zeitschrift für Physik A Hadrons and Nuclei*, vol. 114, n° 5, 1939, p. 368–378, Springer.

[WAN 07] WANG G., ZHAO D., BAI H., PAN M., XIA A., HAN B., XI X., WU Y., WANG W.
Nanoscale periodic morphologies on the fracture surface of brittle metallic glasses. *Physical review letters*, vol. 98, n° 23, 2007, page 235501, APS.

[WAN 19] WANG M., ZHAO L., FOURMEAU M., NELIAS D.
Crack plane deflection and shear wave effects in the dynamic fracture of silicon single crystal. *Journal of the Mechanics and Physics of Solids*, vol. 122, 2019, p. 472–488, Elsevier.

[WEN 13] WENHAM S. R., GREEN M. A., WATT M. E., CORKISH R., SPROUL A.
Applied photovoltaics. Routledge, 2013.

[WIL 97] WILLIS J., MOVCHAN A.
Three-dimensional dynamic perturbation of a propagating crack. *Journal of the Mechanics and Physics of Solids*, vol. 45, 1997, p. 591 - 610.

[WIL 01] WILLIS J., MOVCHAN A.
The influence of viscoelasticity on crack front waves. *Journal of the Mechanics and Physics of Solids*, vol. 49, n° 9, 2001, p. 2177–2189, Elsevier.

[WOR 65] WORTMAN J., EVANS R.
Young's modulus, shear modulus, and Poisson's ratio in silicon and germanium. *Journal of applied physics*, vol. 36, n° 1, 1965, p. 153–156, AIP.

[WU 12] WU H., MELKOTE S. N., DANYLUK S.
Mechanical strength of silicon wafers cut by loose abrasive slurry and fixed abrasive diamond wire sawing. *Advanced Engineering Materials*, vol. 14, n° 5, 2012, p. 342–348, Wiley Online Library.

[YOF 51] YOFFE E. H.
LXXV. The moving griffith crack. *The London, Edinburgh, and Dublin Philosophical Magazine and Journal of Science*, vol. 42, n° 330, 1951, p. 739–750, Taylor & Francis.

[YU 12] YU X., WANG P., LI X., YANG D.
Thin Czochralski silicon solar cells based on diamond wire sawing technology. *Solar Energy Materials and Solar Cells*, vol. 98, 2012, p. 337–342, Elsevier.

[ZHA 13] ZHANG H., BAEYENS J., DEGRÈVE J., CACÈRES G.
Concentrated solar power plants : Review and design methodology. *Renewable and sustainable energy reviews*, vol. 22, 2013, p. 466–481, Elsevier.

[ZHA 16a] ZHAO L.
On the fracture of solar grade crystalline silicon wafer. Thèse de doctorat, Université de Lyon, 2016.

[ZHA 16b] ZHAO L., MAYNADIER A., NELIAS D.
Stiffness and fracture analysis of photovoltaic grade silicon plates. *International Journal of Solids and Structures*, vol. 97, 2016, p. 355–369, Elsevier.

[ZHA 17] ZHAO L., BARDEL D., MAYNADIER A., NELIAS D.
Crack initiation behavior in single crystalline silicon. *Scripta Materialia*, vol. 130, 2017, p. 83–86, Elsevier.

[ZHA 18a] ZHAO L., BARDEL D., MAYNADIER A., NELIAS D.
Velocity correlated crack front and surface marks in single crystalline silicon. *Nature communications*, vol. 9, n° 1, 2018, page 1298, Nature Publishing Group.

[ZHA 18b] ZHAO L., WANG M., MAYNADIER A., NELIAS D.
Disturbance and recovery in high speed (110) cleavage in single crystalline silicon. *Journal of the European Ceramic Society*, vol. 38, n° 4, 2018, p. 1038–1045, Elsevier.

FOLIO ADMINISTRATIF

THESE DE L'UNIVERSITE DE LYON OPEREE AU SEIN DE L'INSA LYON

NOM : WANG

DATE de SOUTENANCE : 15/11/2019

Prénoms : Meng

TITRE : Dynamic fracture of solar grade single crystalline silicon wafers

NATURE : Doctorat

Numéro d'ordre : 2019LYSEI081

Ecole doctorale : MECANIQUE, ENERGETIQUE, GENIE CIVIL, ACOUSTIQUE

Spécialité : Mécanique – Génie Mécanique – Génie Civil

RESUME : Crystalline silicon has attracted substantial attention for decades because of its large applications in solar cells and microelectromechanical systems. The high brittleness of silicon raises wide concerns since the failure of this semiconductor material increases the cost of fabrication and decreases the efficiency of the utilization of Si-based devices. Crack propagation of crystalline silicon is the main cause of catastrophic failure of silicon components. It has been intensively studied but is not fully understood yet due to intricate dynamic fracture behavior linked to small-scale phenomena. Therefore, the development of feasible methods to study the dynamic fracture and further understanding of fracture mechanism of crystalline silicon are of paramount importance to improve the reliability and durability of Si-based systems for both industrial and scientific practitioners. In this work, dynamic fracture behavior of solar-grade single crystalline silicon wafers under mechanical loads was studied. The fracture experiments were carried out on the (001) silicon wafer using three-line or four-line bending apparatus under quasi-static loading. The entire fracture process was captured using a high-speed camera and analyzed by the high-speed imaging technique. The post-mortem fracture surface was studied using a digital microscope, a laser scanning profilometer, as well as an atomic force microscope. The failure source of the silicon wafer was identified using fractographic analysis. Coupling the crack velocity measurement and fractographic analysis, the source of (110)-(111) cleavage plane deflection phenomena during high-speeding crack propagation was revealed. Besides, jointly with the finite element simulations, how dynamics of the crack front is governed by the crystallographic direction-dependent dynamic fracture toughness was demonstrated. Finally, in comparison with linear elastic waves that lead to the Wallner lines on the fracture surface, the nucleation and strong nonlinear characteristics of out-of-plane corrugation waves was highlighted, leaving specific traces that alter the surface roughness of asperity-free material.

MOTS-CLÉS : Brittle fracture, Single crystalline silicon, Dynamic crack propagation, Crack deflection, Shear waves, Corrugation front waves.

Laboratoire (s) de recherche : Laboratoire de Mécanique des Contacts et des Structures
UMR CNRS 5259 - INSA de Lyon
20, avenue Albert Einstein
69621 Villeurbanne Cedex FRANCE

Directeur de thèse: Professeur Daniel NELIAS

Président de jury :

Composition du jury : Amal CHABLI
Fineberg JAY
Daniel NELIAS
Daniel BONAMY
Mokhtar ADDA-BEDIA
Marion FOURMEAU